BIOAUTOGRAPHY, COMBINATION EFFECTS AND PHOTO-ACTIVATED ENZYMATIC RESTRICTION INHIBITORY ACTIVITY OF ANTIMICROBIAL ALKALOIDS FROM GLYCOSMIS PENTAPHYLLA (RETZ.) DC.

Nurhaya Md Taib[1a], Norazian Mohd Hassan[2a*], Laina Zarisa Mohd Kamal[3a] and May Khin Soe[4b]

Abstract: *Glycosmis pentaphylla* (Retz.) DC., locally known as nerapan, has long been used in Asian countries as a traditional remedy for ailments attributed to microbial infections. This study aims to isolate antimicrobial alkaloids from *G. pentaphylla*, to determine their combination effects with selected antimicrobial agents and to screen for their photoactivated enzymatic restriction inhibitory activity. Bioautography-guided isolation of antimicrobial alkaloids was performed by using column chromatography with *Staphylococcus aureus*, *Escherichia coli*, and *Candida albicans* as the indicator microbes. The antimicrobial effects of the alkaloids combined with selected antimicrobial agents, namely, ciprofloxacin, erythromycin, vancomycin, and ketoconazole, were determined by using a checkerboard assay. Photoactivated enzymatic restriction inhibitory activity was assessed by using agarose gel electrophoresis. Two antimicrobial active alkaloids were isolated and identified as arborinine and arborine. The antimicrobial activity of arborinine and arborine was determined to be in the range of 250 μg/ml and 1000 μg/ml. Partial synergy was observed for all arborine-antibiotics and arborinine-ketoconazole interactions against *S. aureus* and *C. albicans*, respectively. Arborine was relatively the strongest photoactivated enzymatic restriction inhibitor, particularly against EcoRI, PstI, and SalI. The results obtained are promising and encourage further research on the alkaloids as potential antimicrobial-enhancing agents.

Keywords: Alkaloids, antimicrobial, bioautography, Glycosmis pentaphylla, photo-activated enzymatic restriction inhibition

1. Introduction

The emergence of microbial resistance has been a threat in therapies for microbial infections. This has led to an interest in plant-based antimicrobial agents and synergistic antimicrobial enhancers, as plants are great sources of bioactive compounds (Cheesman et al., 2017; Khameneh et al., 2019). The antimicrobial combination is a promising strategy aimed at increasing treatment efficacy and controlling resistance prevalence. The subsequent reduction in the side effects of highly toxic antimicrobial agents is expected through efficacy enhancement, allowing the use of a drug in low dosages (van Vuuren & Viljoen, 2011; Bollenbach, 2015). Although plant-based antimicrobials are considered milder in terms of effectiveness than conventional antimicrobial agents, their various mechanisms of action render microbes less likely to develop resistance (Bhardwaj et al., 2016). Alkaloids possessing acridone and quinazolinone nuclei are among the active scaffolds that have inspired researchers in the search for new antimicrobial agents due to their promising activity (Asif, 2014; He et al.,

2017). Naturally, these compounds exist abundantly in the species of the Rutaceae family (da Silva et al., 2017).

Glycosmis pentaphylla (Retz.) DC. is a shrub or small tree of the Rutaceae family known by its common name orangeberry, or nerapan in Malay. It is also called a toothbrush plant for the use of its mild astringent and bitter fibrous stems as a toothbrush (Hazarika & Dutta, 2013). The species is wildly found in secondary thickets of low and medium altitudes from India to Sri Lanka, South East Asia including Peninsular Malaysia, Sumatra and Java, Southern China, and north eastern Australia, and is also grown elsewhere (Chua & van Valkenberg, 2001; Wang et al., 2006). *G. pentaphylla* has long been widely used in various traditional medicine preparations including Ayurvedic medicine to cure diarrhea, coughs, rheumatism, anemia, and jaundice. The leaf and root are used in remedies for treating fever, liver complaints, bronchitis, eczema, skin affections, inflammation, stomach pain, bilious attacks, and intestinal trouble and are also taken as an appetizer during confinement (Chua & van Valkenberg, 2001; Aye et al., 2019; Mat Salleh & Latiff, 2002; Sreejith et al., 2012).

Numerous phytochemicals are present in different parts of *G. pentaphylla* including alkaloids, amides, imides, terpenoids, coumarins, and flavonoids, and their pharmacological properties have been reviewed (Sreejith et al., 2012). The species is characterized by the accumulation of anthranilate-derived alkaloids, namely quinazolines, furoquinolines, quinolones, and acridones (da Silva et al., 2013). Arborine, a quinazolin-4-one alkaloid is present abundantly in the leaf, whereas arborinine, an acridone, and

Authors information:

[a]Department of Pharmaceutical Chemistry, Kulliyyah of Pharmacy, International Islamic University Malaysia, 25200 Kuantan, Pahang, MALAYSIA. Email: nurhayamdtaib@gmail.com[1]; norazianmh@iium.edu.my[2]; lainazarisa84@gmail.com[3]
[b]Department of Basic Medical Sciences, Kulliyyah of Pharmacy, International Islamic University Malaysia, 25200 Kuantan, Pahang, MALAYSIA. Email: may_soe@iium.edu.my[4]

*Corresponding Author: norazianmh@iium.edu.my

skimmianine, a furoquinoline, are distributed in almost all parts of the plant (Sreejith et al., 2012; Yang et al., 2012). Different types of carbazole alkaloids such as glycosmisine, glycozoline, glycozolidine, glycozilinine, and biscarbalexin are also found mainly in the stems and roots (Yang et al., 2012; Chen et al., 2015; Kumar et al., 2018).

The antimicrobial properties of the crude extracts of *G. pentaphylla* have been demonstrated in many studies. Chloroform, ethyl acetate, and methanol extracts with moderate to high polarity exhibited a broad spectrum of activity particularly against the most susceptible microbes, namely *S. aureus*, *E. coli*, *Salmonella paratyphi*, and *C. albicans* (Howlander et al., 2011; Bulbul & Jahan, 2016; Ali et al., 2011; Murugan & Natarajan, 2016). The reported antimicrobial active alkaloids of *G. pentaphylla* include arborinine (Das & Deka, 2017), glycozolidol (Battacharyya et al., 1985), skimmianine, kokusaginine, haplopine, and flindersine (Hanawa et al., 2004). A few carbazole alkaloids namely glycoborinine, glycobomine, and carbalexin A are the antimicrobial active compounds identified in the stem extract. In addition, glycoborinine was determined as a photoactivated alkaloid when tested against *S. aureus* and *B. subtilis* (Yu et al., 2012). Therefore, this study was performed to isolate antimicrobial alkaloids from *G. pentaphylla*, to assess their combination effects with selected antimicrobial agents and to screen for their photoactivated enzymatic restriction inhibitory activity.

2. Materials and Methods

2.1 Chemicals

All solvents and chromatographic materials were from the Merck brand (Merck KGaA, Darmstadt, Germany). Vancomycin, erythromycin, ketoconazole, iodonitrotetrazolium chloride, and thiazolyl blue tetrazolium bromide were purchased from Sigma-Aldrich Chemicals (Sigma-Aldrich Inc., St. Louis, USA), whereas ciprofloxacin was purchased from BioChemika-Fluka (Buchs, Switzerland). Broth and agar media (Meuller Hinton and Sabauraud Dextrose) were from the BD Difco brand (Becton, Dickinson, and Co., Maryland, USA). A plasmid, pNEB 193, the DNA marker (1 kb ladder), and the restriction enzymes used in this study were purchased from Thermo Fisher Scientific (Fermentas, Vilnius, Lithuania).

2.2 Instrumentations

Visualization of chromatograms from thin-layer chromatography (TLC) and spectral recording of melting point (uncorrected), UV, infrared, ^{1}H NMR, ^{13}C NMR, and mass of the isolated compounds were performed by using the respective instrumentations as previously reported (Mohd Kamal et al., 2018). The electrophoresis gel images were captured using AlphaImager DE500 (Genetic Technologies Inc., Australia).

2.3 Plant Materials

G. pentaphylla (Retz.) DC. was collected at Pasir Putih, Kelantan, Malaysia. The species verification was performed by Dr. Shamsul Khamis, the botanist of the National University of Malaysia Herbarium (UKMB). A specimen with voucher number PIIUM 0001-1 was kept at the Herbarium, Kulliyyah of Pharmacy, International Islamic University Malaysia. The air-dried leaves were ground to powder form and left in the 4 °C cold room before further investigation.

2.4 Alkaloid Extraction

Acid-base extraction method as previously described (Mohd Kamal et al., 2018) was employed to furnish crude alkaloidal extracts of the leaf (130.68 g).

2.5 Alkaloid Chromatography

The crude alkaloidal extract (0.5 g) was chromatographed through silica gel packed column (40 g, 60-120 mesh) (glass column, 2 x 83 cm). The column was gradient eluted with 200 ml of each of the following: hexane (100%), hexane/$CHCl_3$ (9:1 - 0:1, 10% increment of $CHCl_3$) and $CHCl_3$/MeOH (99:1 - 9:1, 1% increment of MeOH). Twenty ml of eluents was collected while fractionation was monitored by TLC analysis to obtain eight fractions (GP1 to GP8). The fractions, GP3 and GP6 showed antimicrobial active spots labelled GP3-3 and GP6-3, respectively, as revealed by TLC agar overlay bioautographic screening. To elute GP3-3 (222 mg, 60%), fraction GP3 (370 mg) was re-chromatographed on silica gel (40 g) (column 2 x 40 cm) with 50 ml each of hexane (100%), hexane/$CHCl_3$ (1:1 - 1:9, 10% increment of $CHCl_3$), and 250 ml of $CHCl_3$ (100%). Fraction GP6 (370 mg) was further chromatographed using 100 ml of $CHCl_3$ (100%), followed by 200 ml each of $CHCl_3$/MeOH (99:1 - 99:3, 1% increment of MeOH), to elute GP6-3 with $CHCl_3$/MeOH (98:2) (148 mg, 40%).

2.6 Antimicrobial activity

2.6.1 Microbial strains

The lyophilized strains of the American Type Culture Collection, namely *Staphylococcus aureus* ATCC 25923, *Escherichia coli* ATCC 25922, and *Candida albicans* ATCC 90028 were used. The bacterial and yeast cultures were grown and maintained on Mueller Hinton and Sabouraud Dextrose media, respectively.

2.6.2 Microbial inocula

The microbial inocula were prepared from bacterial cultures incubated at 37 °C for 18 h and yeast cultures incubated at 30°C for 48 h (Rahalison et al., 1991). The concentration of bacterial and yeast inocula was adjusted to an absorbance of 0.11 to 0.12 and 0.1 to 0.2 at 600 nm, respectively, using UV Spectrophotometer. The absorbance corresponded to 10^6 to 10^7 colony forming units (CFU)/ml for bacteria, and 10^7 to 10^8 CFU/ml for yeast.

2.6.3 TLC Agar Overlay Bioautographic Assay

The procedure used was adapted from Rahalison et al. (1991) with some modifications by Mohd Kamal et al. (2018). Ten mg/ml of each alkaloid fraction was

chromatographed on a sterile 4 cm x 10 cm silica gel G60 F$_{254}$ aluminum sheet TLC plates with a layer thickness of 0.2 mm. The TLC of each fraction was developed in duplicate under sterile conditions. One chromatogram was used as a reference for alkaloid characterizations on TLC under UV lights at 254 nm and 366 nm, and with Dragendorff's reagent staining. Molten agar at 37 ℃ was mixed with microbial inocula at a ratio of 9:1. The second chromatogram was placed in a sterile square petri dish lined with moist filter paper. Twenty ml of the inoculated agar was rapidly distributed onto the chromatograms and left to solidify. The chromatograms with bacteria and yeast or bioautograms were incubated at 37 °C for 18 h and 30 °C for 48 h, respectively. The bioautograms were then stained with 0.5% iodonitrotetrozolium chloride (INT) before being incubated for another four hours. The antimicrobial activity of the alkaloids was determined through the formation of a growth inhibitory area observed as a stainless zone, surrounded by pink surroundings of living microbes.

2.6.4 Checkerboard assay

The alkaloid-antimicrobial agent combination effects were studied against *S. aureus*, *E. coli*, and *C. albicans* following CLSI (2006) guidelines with minor modifications. The serial dilution of each alkaloid (2000 µg/ml to 0.977 µg/ml) was prepared in the 96-well plate in a vertical dimension, whereas the antimicrobial agent (1000 µg/ml to 7.8125 µg/ml) was serially diluted in the horizontal dimension. Twenty µl of the compound was prepared for each test concentration for an activity assay, whereas the combination of 10 µl of alkaloid and 10 µl of the antimicrobial agent was tested for the combination study. A total of 180 µl of inoculated broth containing 10^4 to 10^5 CFU/ml of bacteria or 10^5 to 10^6 CFU/ml of yeast was added to the designated wells. The bacterial and yeast plates were incubated at 37 °C for 18 h and 30 °C for 48 h, respectively. All samples were tested in triplicate. The minimum inhibitory concentration (MIC) of the test sample against the respective microbe was determined as the lowest concentration that did not cause turbidity and a colour change from yellow to blue after 30 minutes of subsequent incubation with 10 µl of 0.25% thiazolyl blue tetrazolium bromide in each well. The antimicrobial combination effect was determined using the fractional inhibitory concentration index (FICI) (Choi et al., 2009).

2.7 Photoactivated Enzymatic Restriction Inhibitory Activity

2.7.1 DNA amplification

A DNA fragment was synthesized by Polymerase Chain Reaction (PCR) using pNEB 193 as a template. The selected primers used were forward 5'-TCGCGCGTTTCGGTGATGAC and reverse 5'-AGCGTCAGACCCCGTAGAAAAGATC. PCR was performed in 0.2 ml PCR tubes based on the protocol provided by the SensiMixPlus SYBR Kit. Standard PCR reactions were carried out in a total volume of 50 µl of the following mixture: 25 µl of SensiMixPlus SYBR Kit, 2 µl of 200 nM forward and reverse primer, 10 µl of 100 ng DNA template, and 2 µl of 5 µM magnesium chloride with added sterile distilled water up to 50 µl. PCR cycling conditions were conducted using the BioradTM; IQ5 multicolor real-time PCR detection system as follows: 94 °C for 2 minutes; 25 cycles of 94 °C for 15 seconds; 64 °C for 30 seconds; 72 °C for one minute and 72 °C for 10 minutes (Hanawa et al., 2004). The resulted 1.5-kb DNA fragment was analyzed by 0.8% agarose gel electrophoresis.

2.7.2 Photoactivated enzymatic restriction inhibitory assay

The assay was carried out as described by Hanawa et al., (2004) for the antimicrobial active alkaloids and antibiotic, ciprofloxacin. A total of 100 ng of 1.5-kb DNA fragment was mixed with one nmol of the compounds (2 µl from 500 µM in 2.5% DMSO solution) in a 1.5-ml microcentrifuge tube. The total volume was adjusted to 8 µl with sterile distilled water. The mixtures were irradiated with UVA (24.1 kJ/m2) on ice. After irradiation, 10 units of restriction enzymes (1 µl, respectively, depending on the supplied concentrations of the enzymes) and 1 µl of 10X buffers for the respective enzymes were added to the mixtures. The restriction enzymes used in this study are BamHI, EcoRI, KpnI, SacI, BfuI, MssI, HindIII, PstI, XbaI, SmaI, SgsI, PacI, DraI, and SalI. The mixtures were incubated for 1 h at 37 ℃. A mixture of 10 µl of sample and 1 µl of gel loading dye was loaded into each well of the 0.8% agarose gel chamber and 1.5 µl of DNA ladder was loaded in the first lane. The samples were electrophoresed at 100 volts or 400 mA for 35 minutes. The gel was stained for an hour in a staining tray containing 200 ml of distilled water and 2 drops of ethidium bromide. Then, it was destained with 200 ml of distilled water for 20 minutes. The image of the gel was captured and analyzed.

3.   Results and Discussion

3.1   Bioautography-guided isolation of antimicrobial alkaloids

In this study, alkaloidal fractions of *G. pentaphylla* were initially screened for their antimicrobial active alkaloids against the indicator microbes, namely *S. aureus*, *E. coli*, and *C. albicans*. The TLC agar overlay bioautography screening allows the detection of bioactive compounds in an extract and facilitates their isolation through a bioassay-guided approach (Dewanjee et al., 2015). Two antimicrobial active alkaloids were detected, labelled as GP3-3 and GP6-3 from GP3 and GP6 fractions (Figure 1), respectively. The alkaloids were successfully isolated by using column chromatography and identified based on their spectroscopic data and comparison with that of literature. GP3-3 was assigned to 2,3-dimethoxy-1-hydroxy-10-methylacridone or arborinine (Figure 2a) (Mawardi et al., 2010), with characteristics identical to that of previously reported from *Ruta angustifolia* (Mohd Kamal et al., 2018). GP6-3 was confirmed as 2-benzyl-1-methylquinazolin-4(1H)-one with the trivial name arborine (Figure 2b) (Farediah et al., 1996).
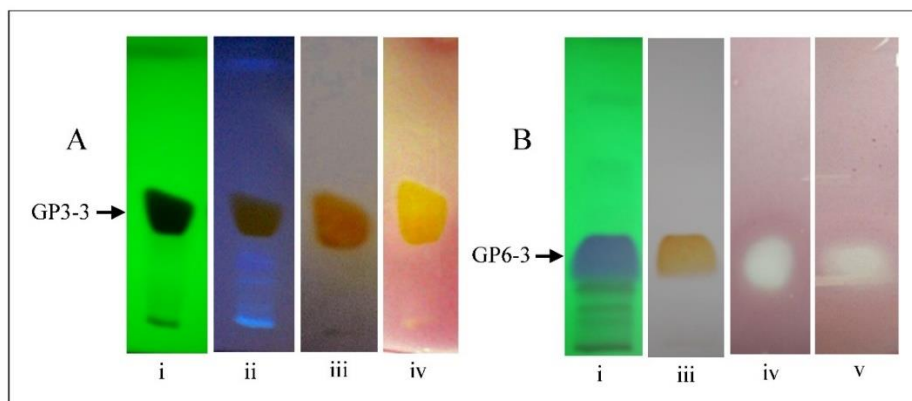
Figure 1. Bioautography of *G. pentaphylla* leaf fractions showing GP3-3 and GP6-3 as the respective antimicrobial active alkaloids. A: fraction GP3, B: fraction GP6, visualized chromatograms with i: UV254 light, ii: UV366 light, iii: Dragendorff's reagent, and the bioautograms iv: *S. aureus*, v: *E. coli*.

GP6-3: 2-Benzyl-1-methylquinazol-4-one [Arborine]; $C_{16}H_{14}N_2O$, MW: g/mol; colorless rhombohedral plates; MP: 156-156ºC, Rf: 24.7 (CHCl₃:EtOAc, 9:1); IR (CHCl₃) cm⁻¹: 1641, 1598, 1527, 707; UV/Vis λ_{max} (MeOH) nm: 203, 229, 276, 304; ¹H NMR (500 MHz, CDCl₃) δ: 8.39 (*dd*, 1.0, 8.0, H-5), 7.72 (*t*, 8.5, H-7), 7.50 (*t*, 8.0, H-6), 7.35-7.39 (*m*, H-8), 7.28-7.39 (*m*, H-2", H-3", H-4", H-5", H-6"), 4.35 (2H, *s*, H-C1'), 3.65 (3H, *s*, *N*-CH₃); ¹³C NMR (100 MHz, CDCl₃) δ: 169.04 (C-4), 162.25 (C-8a), 141.57 (C-2), 133.90 (C-7), 134.58 (C-1"), 129.20 (C-6" & C-2"), 128.32 (C-3", C-4" & C-5"), 127.50 (C-5), 126.05 (C-6), 120.14 (C-4a), 114.54 (C-8), 43.50 (C-1'), 34.93 (*N*-CH₃). MS (EI, 70 eV): *m/z* (%) = 285 [M⁺] (52), 270 (100), 256 (15), 242 (85), 227 (5), 212 (12), 199 (59), 171 (12), 143 (9), 115 (10).
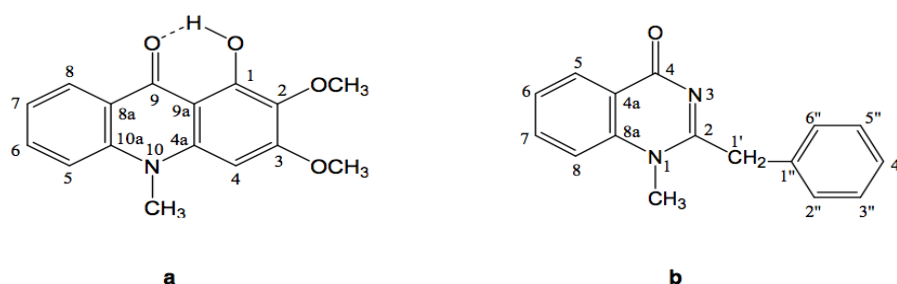
Figure 2. Antimicrobial alkaloids of *G. pentaphylla*. a: Arborinine b: Arborine.

3.2 Antimicrobial activity and combination effects

Arborinine and arborine exhibited a different degree of antimicrobial activity at MIC in the range of 250 µg/ml to 1000 µg/ml against *S. aureus*, *E. coli*, and *C. albicans*. A dual combination of antimicrobial agents is a multi-targeted strategy expected to enhance the actions or counter any possible adverse side effects of both agents (Monte et al., 2014). Arborine was combined with selected antimicrobial agents of different mechanisms of action including ciprofloxacin as a DNA gyrase inhibitor, erythromycin as a protein synthesis inhibitor, and vancomycin as a bacterial cell wall synthesis inhibitor (Khameneh et al., 2019). Considering the activity against *C. albicans*, both arborine and arborinine have been evaluated for their antifungal combined effects with ketoconazole, which disrupt the cell membrane permeability by blocking ergosterol synthesis (Cui et al., 2015). The antimicrobial combinations have resulted in different effects as interpreted from their FICI values (Table 1).

The most effective combination was arborine-ciprofloxacin partial synergism interaction, FICI (0.25) with the respective eight- and two-fold antibacterial activity enhancement against *S. aureus*. In comparison, the two-fold enhancement in the activity of ciprofloxacin in a dual antimicrobial agent combination was achieved with either erythromycin or vancomycin, but with an additive effect (FICI, 1.00) (Mohd Kamal et al., 2018). The antimicrobial combination effects are expected from the simultaneous

action of both agents on different cellular targets that enhance each other's activity. As arborine is a quinazolinone that is more favorable to interact with the cell wall and DNA structures of Gram-positive bacteria (Mohamed et al., 2013), ciprofloxacin molecules would go into the cell and target the DNA gyrase, inhibiting DNA synthesis, which results in bacterial death (Khameneh et al., 2019). Meanwhile, partial synergy (FICI, 0.75) was observed in arborine-vancomycin and arborine-erythromycin interactions, resulting in either four- or two-fold enhancement in their antimicrobial activity. Vancomycin acts by targeting the peptidoglycan wall of the Gram-positive microbe while erythromycin acts as an inhibitor to protein synthesis (Khameneh et al., 2019), which combination may contribute to the dual mechanism of action, although it may not be up to a synergistic level. Therefore, it is suggested that arborine-ciprofloxacin is a potent combination in achieving combined effects in the treatment against *S. aureus*.

Table 1. Antimicrobial combination effects of alkaloids from *G. pentaphylla* and selected antimicrobial agents.

Microorganism	Combination	MIC (µg/ml)		FIC	FICI	Combination effect
		Alone	Combined			
S. aureus ATCC 25923	Arborine Ciprofloxacin	1000 0.195	125 0.098	0.125 0.500	0.625	Partial synergy
	Arborine Erythromycin	1000 1.098	500 0.275	0.500 0.250	0.750	Partial synergy
	Arborine Vancomycin	1000 2.500	250 1.250	0.250 0.500	0.750	Partial synergy
	Ciprofloxacin Erythromycin	0.195 1.098	0.098 0.549	0.500 0.500	1.000	Additive*
	Ciprofloxacin Vancomycin	0.195 2.500	0.098 1.250	0.500 0.500	1.000	Additive*
E. coli ATCC 25922	Arborine Ciprofloxacin	500 0.039	500 0.156	1.000 4.000	5.000	Antagonism
	Arborine Erythromycin	500 50	500 6.25	1.000 0.125	1.125	Indifference
	Arborine Vancomycin	500 250	250 125	0.500 0.500	1.000	Additive
	Ciprofloxacin Erythromycin	0.039 50	0.019 1.562	0.500 0.031	0.531	Additive*
	Ciprofloxacin Vancomycin	0.039 250	0.002 7.813	0.050 0.031	0.081	Synergy*
C. albicans ATCC 90028	Arborine Ketoconazole	500 1.562	500 0.781	1.000 0.500	1.50	Indifference
	Arborinine Ketoconazole	250 1.562	125 0.390	0.500 0.250	0.750	Partial synergy
	Ketoconazole Miconazole	1.562 5.000	1.562 2.500	1.000 0.500	1.500	Indifference

*: Previously reported by Mohd Kamal et al., 2018.

Arborine-antimicrobial agent combination against *E. coli* exhibited only slight enhancement in the antibacterial activity of both agents. Interestingly, combination with vancomycin resulted in a two-fold enhancement in the antimicrobial activity of both agents despite the low susceptibility of Gram-negative bacteria toward vancomycin due to the presence of an outer membrane barrier against large glycopeptide (Zhou et al., 2015). This finding demonstrated an achievable broader spectrum of activity of vancomycin against Gram-negative bacteria when used in combination with other compounds as demonstrated in previous studies (Leite et al., 2015). Nevertheless, the combination was not as effective as that of ciprofloxacin-vancomycin, which exhibited a strong synergy at a FICI of 0.081 (Mohd Kamal et al., 2018). Thus, arborine and ciprofloxacin are suggested as suitable combination agents for vancomycin against Gram-negative bacteria, which potential application in treating infections by multidrug-resistant pathogens may be further investigated (Zhou et al., 2015). Meanwhile, the combination of arborine and ciprofloxacin produced antagonistic effects, by which arborine hindered the effect of ciprofloxacin four-fold.

Arborinine is the best combination agent for ketoconazole against *C. albicans* with two- and four-fold enhancement in antimicrobial activity based on partial synergism (FICI, 0.625), compared with that of arborine or miconazole combinations. The planar structure of arborinine allows it to function as a DNA intercalator with the potential to synergize with azole antifungals. The disrupting activity of azoles against fungal cell plays an important role in increasing the intracellular concentration of DNA intercalators to bind with DNA, exerting cell cycle arrest and DNA damage (Li et al., 2013). Meanwhile, the arborine-ketoconazole combination produced an insignificant effect, which is evident in the two-fold enhancement in the antifungal activity of ketoconazole at the MIC of arborine. Additionally, the ketoconazole-miconazole insignificant interaction was observed in the two-fold increase in miconazole activity. The enhancement effect of miconazole was most probably due to its dual actions in inhibiting peroxidases, which allows accumulation of intracellular peroxide, resulting in cell death, and the shared ergosterol synthesis inhibitory property with ketoconazole (Fothergill et al., 2014).

3.3 Photo-activated enzymatic restriction inhibitory activity

The bioactive alkaloids, particularly acridones, quinolines, and quinazolines have gained considerable interest in the field of antimicrobial, and anticancer drug development. These compounds partly rely on the ability of their polyheteroaromatic structures to interact with DNA or the systems involved in the mechanisms controlling cellular topology, repair, and replication (Tillequin, 2007; Kamel et al., 2016). In this study, arborinine and arborine exhibited the ability to inhibit the activity of the restriction enzymes, resulting in uncleaved DNA fragment that can be observed on the electrophoresis gel. Both alkaloids are photoactivated compounds, which inhibited the enzymatic activity of restriction endonucleases to varying degrees under UVA irradiation but were inactive inhibitors in the dark (Figure 3).
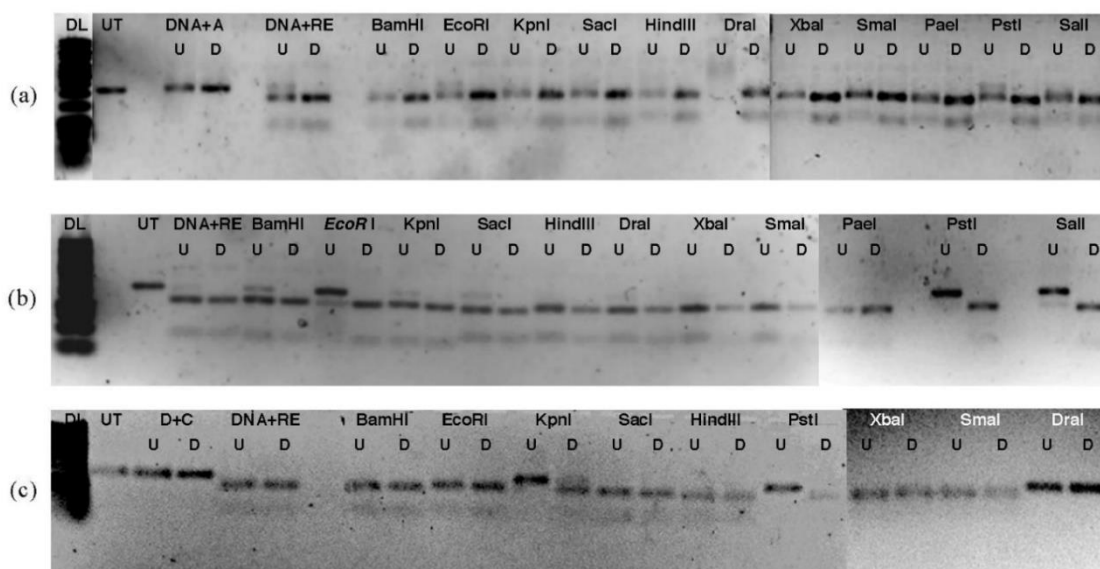
Figure 3. Effects of test compounds on the cleavage of the 1.5 kb DNA fragment by the selected restriction enzymes which have restriction sites on the fragment. A: arborinine, B: arborine, C: ciprofloxacin, DL: DNA ladder, RE: restriction enzyme, U: UVA light irradiation, D: Dark, UT: untreated 1.5 kb DNA fragment.

Both alkaloids inhibited EcoRI, a Type 2A enzyme with restriction sites recognizing a 5'ApT sequence, and PstI, a Type 2B restriction enzyme that recognizes at least one A (or T) in the recognition site, which does not have either 5'ApT or 5'TpA sequence. Arborinine showed relatively the strongest inhibitory activity against DraI, a Type I enzyme recognizing a 5'-TpA sequence in the restriction site, and moderate inhibition against EcoRI and PstI. The inhibition of

the cleaving activity of DraI may be partly attributed to the resistance of its recognition sequence against UV irradiation. Meanwhile, an insignificant effect was observed in the cleaving activity of other enzymes with restriction sites lacking the 5'-TpA sequence (Hanawa et al. 2001). Arborine was found to be the most active inhibitor, with relatively strong activity against EcoRI, PstI, and SalI, whereas moderate activity against BamHI, a Type 2A enzyme. The strong sequence-specific binding affinity of arborine in the 5'-GAATTC-3' restriction site of EcoRI demonstrates its potential therapeutic property as the sequence has also been observed in BRCA 2 breast cancer 2, an early onset oncogene (Hassan et al., 2014). The positive control, ciprofloxacin, exhibited inhibition activity against DraI both in the dark and under UVA irradiation. It is a strong photoactivated inhibitor against KpnI, which restriction site contains a 5'ApT sequence, and PstI. Therefore, in descending order of photo-activated enzymatic restriction inhibitory activity, the alkaloids are ranked as arborine > ciprofloxacin > arborinine.

4. Conclusion

Among the tested combinations, arborine-ciprofloxacin is the most potent combination agent against S. aureus, whereas arborinine interacts well with ketoconazole against C. albicans. The findings support the proposed combinations of quinazolones-macrolides and acridones-azoles for potential combined antimicrobial effects against S. aureus and C. albicans, respectively. This study has also identified these alkaloids as photoactivated enzymatic restriction inhibitors. These results warrant further investigation of antimicrobial alkaloids in *G. pentaphylla* for the development of new antimicrobial-enhancing agents

5. Acknowledgement

6. References

Ali, M. A., Abu Sayeed, M., Syaifuddin, A., Sarmina, Y., Mst. Astaq, M. K. & Abu Hanif, M. (2011). An evaluation of antimicrobial activities of *Glycosmis pentaphylla. Research Journal of Agriculture and Biological Sciences* 7(2): 328-331.

Asif, M. (2014). Chemical characteristics, synthetic methods, and biological potential of quinazoline and quinazolinone derivatives. *International Journal of Medicinal Chemistry* 395637. doi: 10.1155/2014/395637

Aye, M. M., Aung, H. T., Sein, M. M. & Armijos, C. (2019). A Review on the phytochemistry, medicinal properties and pharmacological activities of 15 selected Myanmar medicinal plants. *Molecules* 24: 293. doi:10.3390/molecules24020293

Battacharyya, P., Cakrabartty, P. K. & Chowdury, B. K. (1985). Glycozolidol, an antibacterial carbazole alkaloid from *Glycosmis pentaphylla*. *Phytochemistry* 24(4): 882-883.

Bhardwaj, M., Singh, B. R., Sinha, D. K., Kumar, V., Prasanna Vadhana, O. R., Varan Singh, S., Nirupama, K. R., Pruthvishree, Archana Saraf, B. S. (2016). Potential of herbal drug and antibiotic combination therapy: A new approach to treat multidrug resistant bacteria. *Pharmaceutica Analytica Acta* 7(11): 1-14. doi: 10.4172/2153-2435.1000523

Bollenbach, T. (2015). Antimicrobial interactions: mechanisms and implications for drug discovery and resistance evolution. *Current Opinion in Microbiology* 27: 1-9. doi: 10.1016/j.mib.2015.05.008.

Bulbul, I. J. & Jahan, N. (2016). Study on antioxidant and antimicrobial activities of methanolic leaf extract of *Glycosmis pentaphylla* against various microbial strains. *Journal of Pharmacognosy and Phytochemistry* 5(4): 53-57.

Cheesman, M. J., Ilanko, A., Blonk, B. & Cock, I. E. (2017). Developing new antimicrobial therapies: Are synergistic combinations of plant extracts/compounds with conventional antibiotics the solution? *Pharmacognosy Review* 11: 57-72.

Chen, Y., Tang, C., Wu, Y., Mo, S., Wang, S., Yang, G. & Mei, Z. (2015). Glycosmisines A and B: isolation of two new carbazole–indole-type dimeric alkaloids from *Glycosmis pentaphylla* and an evaluation of their antiproliferative activities. *Organic & Biomolecular Chemistry* 13(24): 6773-6781.

Choi, J. G., Kang, O. H., Lee, Y. S., Oh, Y. C., Chae, H. S., Jang, H. J., Shin, D. W. & Kwon, D. Y. (2009). Antibacterial activity of methyl gallate isolated from *Galla rhois* or carvacrol combined with nalidixic acid against nalidixic acid resistant bacteria. *Molecules* 14(5): 1773-1780. doi: 10.3390/molecules14051773

Chua, L. S. L. & van Valkenberg, J. L. C. H. (2001). *Glycosmis pentaphylla* (Retz.) A.D.C. In: van Valkenberg,, J. L. C. H. & Bunyapraphatsara, N. (editors). Plant Resources of South East Asia 12(2): Medicinal and Poisonous Plants 2, pp. 275-278, Leiden: Backhuys Publishers.

CLSI (2006). Methods for Dilution Antimicrobial Susceptibility Tests for Bacteria That Grow Aerobically, Approved Standard Seventh Edition, Document M7-A7 [ISBN 1-56238-587-9]. Wayne: Clinical and Laboratory Standards Institute.

Cui, J., Ren, B., Tong, Y., Dai, H. & Zhang, L. (2015). Synergistic combinations of antifungals and anti-virulence agents to fight against *Candida albicans*. *Virulence* 6(4): 362-371.

Das, M. M. & Deka, D. C. (2017). Evaluation of anticancer and antimicrobial activity of arborinine from *Glycosmis pentaphylla*. *Journal of Biologically Active Products from Nature* 7(2): 131-139.

da Silva, M. F. G. F., Fernandes, J. B., Forim, M. R., Vieira, P. C. & de Saˊ, I. C. G. (2013). Alkaloids derived from anthranilic acid: Quinoline, acridone and quinazoline. In: K. G. Ramawat, and J. M. Meˊrillon (eds.). K. G. Ramawat, and J. M. Meˊrillon (eds.). Natural Products, pp. 715-859, Berlin Heidelberg: Springer-Verlag.

Dewanjee, S., Gangopadhyay, M., Bhattacharya, N., Khanra, R. & Dua, T. K. (2015). Bioautography and its scope in the field of natural product chemistry. *Journal of Pharmacceutical Analysis* 5(2): 75–84.

Farediah, A., Hazar Bebe, M. I. & Mawardi, R. (1996). Arborine, a larval growth inhibitor from *Glycosmis pentaphylla*. *Pertanika Journal of Science and Technology* 4(1): 11-15.

Fothergill, A.W. (2014). Miconazole: a historical perspective. *Expert Review of Anti-infective Therapy* 4(2): 171-175.

Hanawa, F., Fokialakis, N. & Skaltsounis, A-L. (2004). Photo activated DNA binding and antimocrobial activities of furoquinoline and pyranoquinolone alkaloids from Rutaceae. *Planta Medica* 70: 531-535.

Hanawa, F., Okamoto, M. & Towers, G. H. N. (2001). Inhibition of restriction enzyme's DNA sequence recognition by PUVA treatment. *Photochemistry Photobiology* 74(2): 269-273.

Hassan, S. A., Barthwal, R., Padmadeo, S. R. & Barukab, O. M. (2014). Restriction inhibition assay: A qualitative and quantitative method to screen sequence specific DNA binder from herbal plants. *Tropical Journal of Pharm*aceutical *Research* 13(2): 267-273.

Hazarika, P. & Dutta, D. (2013). Traditional knowledge for using plant resources as tooth brushing stick (datun) by the indigenous communities of Assam, India. *International Journal of Herbal Medicinal* 6(6): 22-34.

He, D., Wang, M., Zhao, S., Shu, Y., Zeng, H., Xiao, C., Lu, C. & Liu, Y. (2017). Pharmaceutical prospects of naturally occurring quinazolinone and its derivatives. *Fitoterapia* 119:136-149.

Howlader, M. A., Farhana, R., Shapna, S., Mohammad, R. R., Shams-Ud-Doha, K.M., Rumana, M. & Apurba, S. A. (2011). Antimicrobial, antioxidant, and cytotoxic effects of methanolic extracts of leaves and stems of *Glycosmis pentaphylla* (Retz.). *Journal of Applied Pharmaceutical Science* 1(8):137-140.

Kamel, M. M., Zaghary, W. A., Al-Wabli, R. I. & Anwar, M. M. (2016). Synthetic approaches and potential bioactivity of different functionalized quinazoline and quinazolinone scaffolds. *Egyptian Pharmaceutical Journal* 15(3): 98-131.

Khameneh, B., Iranshahy, M., Soheili, V. & Bazzaz, B. S. F. (2019). Review on plant antimicrobials: a mechanistic viewpoint. *Antimicrobial Resistence and Infection Control* 8: 118. doi: 10.1186/s13756-019-0559-6

Kumar, A., Banerjee, N., Singamaneni, V., Dokuparthi, S. K., Chakrabarti, T. & Mukhopadhyay, S. (2018). Phytochemical investigations and evaluation of antimutagenic activity of the alcoholic extract of *Glycosmis pentaphylla* and *Tabernaemontana coronaria*. *Natural Products Research* 32(5), 582-587.

Leite, G. C., Neto, L. V. P., Gaudereto, J. J., de Maio Carrilho, C. M. D., Ross, F., Anna Sara Levin A. S. & Costa, S. F. (2015). Effect of antibiotics combination and comparison of methods of synergism in multiresistant Gram negative bacteria. *Journal of Infectious Diseases and Therapy* 3: 207. doi: 10.4172/2332-0877.1000207

Li, D-D., Xu, Y., Zhang, D-Z., Quan, H., Mylonakis, E., Hu, D-D., Li, M-B., Zhao, L-Z., Zhu, L-H., Wang, Y. & Jiang, Y. Y. (2013). Fluconazole assists berberine to kill fluconazole-fesistant *Candida albicans*. *Antimicrobial Agents and Chemotherapy* 57(12): 6016-6027.

Mat Salleh, K. & Latiff A. (2002). Tumbuhan Ubatan Malaysia. pp. 473, Bangi: Pusat Pengurusan Penyelidikan Universiti Kebangsaan Malaysia.

Mawardi, R., Rosmiati, M. S., Najihah, M. H., Mohd Aspollah, S., Gwendoline, C. L. E., Abdul Manaf, A. & Hazar Bebe, M. I. (2010). Alkaloids and sulphur-containing amides from *Glycosmis citrifolia* and *Glycosmis elongata*. *Sains Malaysiana* 39(3): 445-451.

Mohamed, M. A., Ghanem, H. M., Abd El-Ghaffar, N. F. & Mohamed, S. S. (2013). Biological evaluation and molecular docking of substituted quinazolinones as antimicrobial agents. *Australian Journal of Basic and Applied Sciences* 7: 263–274.

Mohd Kamal, L. Z., Mohd Hassan, N., Md Taib, N. & Soe, M. K. (2018). Graveoline from *Ruta angustifolia* (L.) Pers. and its antimicrobial. synergistic potential in erythromycin or vancomycin combinations. *Sains Malaysiana* 47(10): 2429-2435.

Monte, J., Abreu, A. C., Borges, A., Simões, L. C. & Simões, M. (2014). Antimicrobial activity of selected phytochemicals against *Escherichia coli* and *Staphylococcus aureus* and their biofilms. *Pathogens* 3(2): 473-498. doi:10.3390/pathogens3020473

Murugan, N. & Natarajan, D. (2016). Phytochemical, antioxidant and antibacterial activities of *Glycosmis pentaphylla* (Rutaceae) leaf extracts against selected multi-drug resistant bacteria. *Journal of Chemical and Pharmaceutical Research* 8(1): 737-744.

Rahalison, L., Hamburger, M., Hostettmann, K., Monod, M. & Frenk, E. (1991). Bioautographic agar overlay method for the detection of antifungal compounds from higher plants. *Phytochemical Analysis* 2:199-203.

Sreejith, P. S., Praseeja, R. J. & Asha, V. V. (2012). A review on the pharmacology and phytochemistry of traditional medicinal plant, *Glycosmis pentaphylla* (Retz.) Correa. *Journal of Pharmacy Research 5*(5): 2723-2728.

Tillequin F. (2007). Rutaceous alkaloids as models for the design of novel antitumor drugs. *Phytochemistry Review* 6: 65-79.

van Vuuren, S. & Viljoen, A. (2011). Plant-based antimicrobial studies - Methods and approaches to study the interactions between natural products. *Planta Medica* 77: 1168-1182.

Wang, J., Di, Y., Yang, X., Li, S., Wang, Y. & Hao, X. (2006). Hydroquinone diglycoside acyl esters from the stems of *Glycosmis pentaphylla*. *Phytochemistry* 67(5): 486-491.

Yang, G.-Z., Wu, Y. & Chen, Y. (2012). Alkaloids from the stems of *Glycosmis pentaphylla*. *Helvetica Chimica Acta* 95: 1449–1451.

Yu., C., Bo, Y., Jing, X., Tong, Z., Hua, F. & Guang-zhong, Y. (2012). Photo-activated DNA binding and antimicrobial activities of alkaloids from *Glycosmis pentaphylla*. *Acta Pharmaceutica Sinica* 47(12): 1646–1652.

Zhou, A., Kang, T. M., Yuan, J., Beppler, C., Nguyen, C., Mao, Z., Nguyen, M. Q., Yeh, P. & Miller, J. H. (2015). Synergistic interactions of vancomycin with different antibiotics against *Escherichia coli*: Trimethoprim and nitrofurantoin display strong synergies with vancomycin against wild-type *E. coli*. *Antimicrobial Agents and Chemotherapy* 59(1): 276-281.

GASTROINTESTINAL PARASITES IN *Macaca fascicularis* LIVING IN TWO URBAN AREAS OF MALAYSIA

Sharifah Aminah Tuan Said[1a], Jaya Vejayan[2a]*, Nur A'fiefah Mohd Zulkeffli[3b] and Hani Kartini Agustar[4b]

Abstract: *Macaca fascicularis* or commonly known as long-tailed macaques, are nonhuman primates that are increasingly vulnerable in becoming natural reservoirs for many microorganisms including gastrointestinal (GI) parasites, largely due to anthropogenic activities. This study was conducted to detect and compare GI parasites in *M. fascicularis* found in densely urbanized settings. The fecal samples of the long-tailed macaques were collected at a public university campus (Universiti Kebangsaan Malaysia, Bangi) and a tourist site (Bukit Melawati, Kuala Selangor). A total of 80 fecal samples were collected: 50 at the university campus, and the remaining samples from the tourist site. The fecal samples were processed by flotation techniques to include the GI parasites and then were subjected to morphological analysis to identify important taxonomy keys under microscopic magnification. A total of 139 parasites were identified from both locations and classified into 5 phylums and 17 families. Among the 139 parasites, 33 parasites were grouped into 6 genus of GI parasites. Among the gastrointestinal parasites that were identified from both study sites, three parasites were zoonotic namely *Strongyloids* spp., *Trichostrongylus* spp. and *Trichuris* spp. Results showed that the diversity index of GI parasites was higher at the university campus compared to the tourist site with Simpson's Index values of 0.953 and 0.880, respectively, while the Shannon's Index values were 3.282 and 2.399, respectively. This research revealed that there are more parasite infections in the long-tailed macaques in the campus surroundings compared to those found in the tourist site. Therefore, it is highly suggested that authority intervention by translocating the long-tailed macaques elsewhere is necessary to avoid prolonged contact and possible parasite transmission to humans, and if any parasitic infections occur, appropriate medication such as anthelmintic drugs should be readily available at the university campus clinics.

Keywords: Monkey, long-tailed macaques, fecal, gastrointestinal parasites, campus

1. Introduction

Macaca fascicularis, also known as the long-tailed macaque, is a cercopithecine monkey native to Southeast Asia (Md-Zain et al., 2010). The food source for the long-tailed macaques might vary depending on the season and altitude, and their eating ecology has largely been documented in lowland environments (Ungar, 1996; Kassim Norazila et al., 2017). They consume a variety of foods which also include non-hygienic food sources that increase the probability for the macaques to be hosts for parasites. Although not all parasites are pathogenic, but some can cause fatality to the macaques (Verweij et al., 2003; Kassim Norazila et al., 2017). Other than food, its wide range of habitats allow *M. fascicularis* to adapt to new challenging environments such as urban habitats. They are frequently seen in tourist areas in Malaysia (Hambali et al., 2014) and many residential areas. This adaptation to new habitats is largely due to anthropogenic activities related to human development that destroy their original habitat, forcing them to dwell in close proximity to humans (Karuppannan et al., 2014).

Anthropogenic environmental changes causing habitat fragmentation may render primate populations more vulnerable to parasite infections, which can result in significant mortality and morbidity in some situations (Chapman et al., 2005; Trejo-Macias & Estrada, 2012). Human-macaque interactions can induce stress in the latter, making them more susceptible to illnesses (Chapman et al., 2005; Valenta et al., 2017). The macaques are less susceptible to parasites if accessible to nutritional crops, which reduces the stress (Wallis, 2000; Hahn et al., 2003). Long-tailed macaques are usually pests as they prefer to live at the edges of forests. They are prone to cause disturbances to local residents by scavenging in garbage dumps, invading their homes (Md-Zain et al., 2011; Md-Zain et al., 2014), biting, scratching, or stealing food from humans (Sha et al., 2009; Md-Zain et al., 2014). However, visitors at tourist destinations may find long-tailed macaques to be part of the

Authors information:

[a]Faculty of Industrial Science and Technology, Universiti Malaysia Pahang. Lebuhraya Tun Razak, Pahang, 26300 Kuantan, MALAYSIA. E-mail: sh.aminahtnsaid@yahoo.com[1], jayavejayan@ump.edu.my[2]
[b]Faculty of Science and Technology, University Kebangsaan Malaysia. Selangor, 43600 Bangi, MALAYSIA. E-mail: mnurafiefah@gmail.com[3], hani_ag@ukm.edu.my[4]
*Corresponding Author: jayavejayan@ump.edu.my

attraction. Visitors usually enjoy feeding the long-tailed macaques because it is part of the tourism appeal. In both situations, humans and macaques are at high risk due to the human-macaque contact, which can lead to negative attitudes regarding macaque welfare and conservation (Webber et al., 2007; Md-Zain et al., 2014), as well as the transfer of zoonatic diseases (Engel & Jones-Engel, 2011; Md-Zain et al., 2014).

Continuous human-primate interactions can lead to the increased likelihood of transmission of parasitic infections and worse, zoonotic diseases, from macaques to humans and *vice versa*. For example, the intestinal parasite, *Trichuris trichiura,* causes diarrhea, bloody diarrhea and anemia in both *M. fascicularis* and humans (Zanzani et al., 2015). Humans and macaques are also susceptible to many of the same infectious illnesses, including tuberculosis and hepatitis, due to their genetic similarities (Grant et al., 2019). Aside from that, free-ranging primate populations are known to have a wide range of endoparasites, including yellow fever virus, helminthes, and lung mites, many of which are transmittable to humans (Nunn & Altizer, 2006; Beisner et al., 2016). Long-tailed macaques have been recognized as parasitic reservoirs (Siregar et al., 2015; Raja et al., 2018), with gastrointestinal parasites being one of the parasites detected (Engel & Jones-Engel, 2011). The parasite that lives in the gastrointestinal tract of the host and contributes considerably to the nutrition and health of the host is known as a gastrointestinal parasite (Amato et al., 2013). Gastrointestinal parasites affect the host's digestive efficiency while the host diet affects the composition of the parasite. Identification of gastrointestinal parasites can be verified through the host faeces. In this study, fecal samples of long-tailed macaques were gathered from two separate areas, one representing a university campus and the other a tourism destination. The goal was to learn more about the existence of gastrointestinal parasites in long-tailed macaques in two separate settings. The variations in gastrointestinal parasites can be recognised and compared.

2.   Methodology

2.1   Sample Collection
At the sampling sites, fecal samples were collected at random, following natural defacation. To reduce environmental contamination, only the top section of the faeces that did not come in contact with the ground and leaf litter were collected. In addition to that, disposable gloves were worn and a new spatula was used to transfer each collected sample into a 70 ml specimen container, to avoid further contamination. The samples were preserved in 10% formalin and kept in an icebox to prevent existing helminth

eggs from hatching or degenerating before further examination (Lane et al., 2010).

2.2   Sampling Sites
For this study, there were two selected sampling sites for fecal sample collection. Both sampling sites are located in Selangor, Malaysia. The first site is Universiti Kebangsaan Malaysia (UKM), commonly known as the National University of Malaysia, a public university situated in Bangi, Selangor (2.93°N, 101.46°E), south of Kuala Lumpur. The samples were collected around the area on campus grounds, where the long-tailed macaques are frequently seen. Figure 1 shows the topography map with 4 spots that were used to collect the fecal samples.
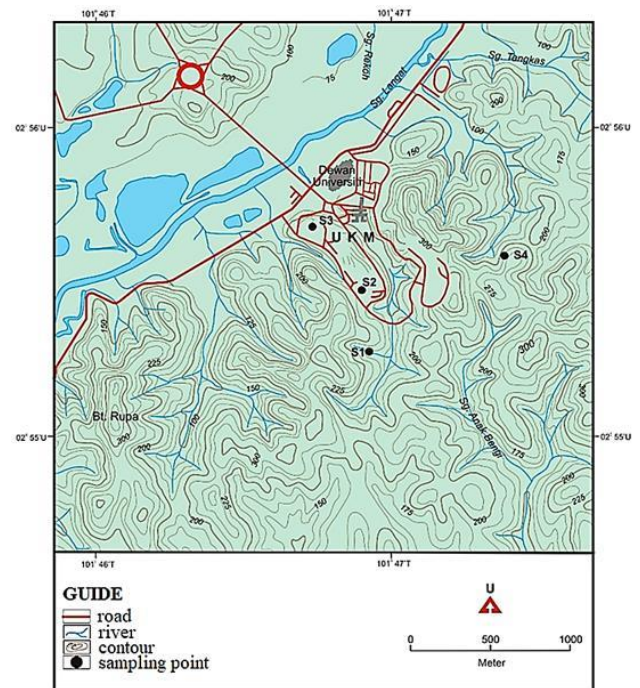
Figure 1. Topography map of the sampling spots at Universiti Kebangsaan Malaysia, Bangi campus

The first spot (S1) was near the dumpster at the Biology Building (2°55'22.0"N, 101°46'55.7"E). At this site, 5 fecal samples were collected. The second spot (S2) was the road side near the library (2°55'30.6"N, 101°46'52.6"E). A total of 15 fecal samples were taken from this location. The third spot (S3) was the road site near the Institute of The Malay World and Civilization (2°55'40.8"N, 101°46'45.4"E) and from this area, 13 fecal samples were collected. The last location (S4) was the road side by the residential area, Kolej Keris Mas (KKM) (2°55'37.0"N, 101°47'25.7"E). From this spot, 17 fecal samples were collected.
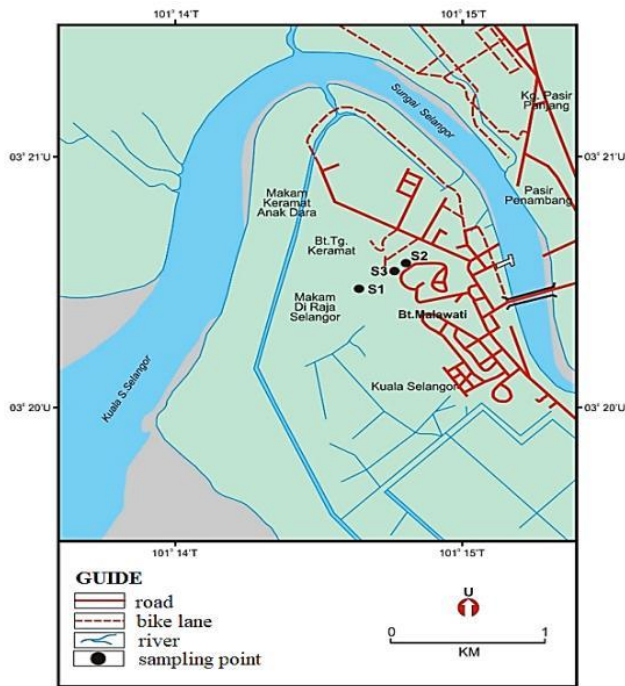
Figure 2. Topography map of the sampling spots at Bukit Melawati, Kuala Selangor (tourist site)

The second sampling site is Bukit Melawati, or also known as Melawati Hill, near Kuala Selangor (3° 20' 31" N, 101° 14' 46" E). The hill is located approximately 120 kilometres northwest from Universiti Kebangsaan Malaysia (according to Google Map) as shown in Figure 2. It is known as one of the popular tourist sites in Kuala Selangor. At Bukit Melawati, there were 3 spots selected to collect the fecal samples of long-tailed macaques as shown in Figure 2. The first spot (S1) was near the Baitulhilal (3°20'29.4"N, 101°14'40.7"E). At this area, 9 samples were collected. The second spot (S2) was at an area referred for the "monkey experience" (3°20'33.3"N, 101°14'47.7"E). Around this area, there were 15 fecal samples collected. The last spot (S3) was at the road site where long-tailed macaques were frequently seen sitting on the guardrails (3°20'33.1"N, 101°14'44.3"E). There were 6 fecal samples collected at this area.

2.3   Parasite Identification
The flotation method was used to identify parasites, specifically helmithes, in the fecal samples. Fecal analysis was carried out using a modified sodium chloride flotation method (Gillespie, 2006). A total of 600 g NaCl was dissolved in 1 L distilled water to make a sodium chloride solution. Centrifugation at 1800 rpm for 10 minutes was conducted to remove the formalin preservative from the faeces. Once the supernatants were discarded, the faeces was homogenised in distilled water before being centrifuged again. Following that, a maximum of 2 g of faeces from each sample was combined with NaCl to fill the sample tube up to 15 mL, and

subsequently centrifuged at 1800 rpm for 10 minutes. The surface liquid was transferred to a slide and covered with a coverslip. The egg from each sample was then examined under standard light microscopy at 10x and 40x magnification. The parasites observed in the fecal samples were primarily identified by referring to academic publications and comparing key morphological features such as shape, colour and size. The three academic publications which were mainly referred to for proper identification of the gastrointestinal parasites are: Anderson, Chabaud & Willmott (1974), Bowman (2003), and Mifsut (2015).

2.4   Statistical Analysis
The data collected was analysed by using biodiversity indexes for parasite family, abundance and richness. The parameters used were dominance, Simpson, Shannon and Evenness. To compare the mean values from two samples, a two-sample t-test was performed using the PAST software to determine whether the mean values of the gastrointestinal parasites from the two locations are statistically different.

3.   Results and Discussions
Long-tailed macaques (*Macaca fascicularis*) are the most common non-human primate species at the Universiti Kebangsaan Malaysia (UKM) and Bukit Melawati areas. Both sites were chosen owing to the long-tailed macaques' varied eating patterns. Long-tailed macaques are commonly seen traversing the campus and residential areas of UKM in search of food. The long-tailed macaques can be frequently seen at the dumpsters looking for leftover food which have also become one of their main food source (Md-Zain et al., 2014). In contrast, the macaques at Bukit Melawati often enjoy food given by tourists and visitors who find animal feeding as part of the attraction at the site. There are fruits and vegetables sellers in the surrounding areas where the visitors can purchase and directly give the food to the macaques (Hambali et al., 2014). Therefore, a comparison can be made regarding the prevalence of gastrointestinal parasites in the faeces of long-tailed macaques based on these two distinct feeding techniques.

Table 1 shows the number of fecal samples collected from *M. fascicularis* and the corresponding number of parasites identified from the university campus and tourist site by referral to morphology keys within the taxonomy classifications up to the ranks of family. In order to have a more comprehensive identification for each microbe up to the species, a combination of morphological recognition with the use of polymerase chain reactions or other molecular detection methods is required (Lastuti et al, 2021; Rivera & Kanbara, 1999; Sricharern et al, 2016; Zanzani et al, 2015). In fact, there are reports of solely using morphological identifications (Adrus et al, 2019; Athaillah et al, 2021; Lane et al, 2010).

Overall, there are a total of 80 fecal samples collected and 139 parasites that have been identified. The fecal samples collected were 50 and 30 at the university campus and tourist site, respectively. It was harder to collect the fecal samples at the tourist site due to its hilly terrain. The total number of parasites that have been identified also vary at both locations. There were 99 parasites on the university campus, but only 40 parasites in the tourist attraction. It was discovered that the prevalence and quantity of parasites were greater on campus. At this site, the long-tailed macaques can usually be seen digging through the waste dumps or invading the rooms at the residential area. Meanwhile, at the tourist site, the long-tailed macaques are usually fed by the tourist or visitors with vegetables and fruits. Hence, due to stress of having lack of food sources and high competition at the university campus compared to the other site, it is expected that the macaques are more susceptible to parasitic infections. A study found that macaques are less susceptible to parasites if they can get nutritional crops and thus decreasing the stress (Wallis, 2000; Hahn et al., 2003).

Table 1. Total fecal samples collected and parasites identified

	Spots	Number of samples collected	Total individuals of parasites identified
University campus	S1	5	9
	S2	15	28
	S3	13	30
	S4	17	32
	Total	50	99
Tourist site	S1	9	8
	S2	15	25
	S3	6	7
	Total	30	40

Figure 3 shows the total of 139 parasites that have been identified and divided into 5 phylums which were Platyhelminthes, Apicomplexa, Arthropoda, Acanthocephala and Nematoda. The highest phylum of parasites that had been identified was Apicomplexa which consists of 40 parasites (28.8%) and the lowest was from Arthropoda with 11 parasites (7.9%).
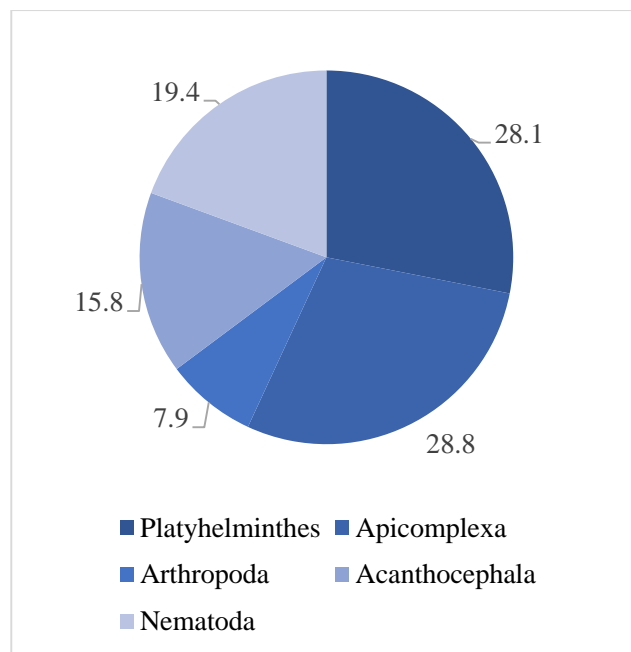
Figure 3. The total abundance (%) of parasites according to phylums

The numbers of identified parasites are different in each phylum for both of the study sites. From Figure 4, it is observed that the highest number of identified parasites for university campus was in the phylum Platyheminthes with 34 parasites and the lowest was in the phylum Arthropoda with 4 parasites. Furthermore, at the tourist site, the highest was from the phylum Acanthocephala with 11 parasites and the lowest was from the phylum Plathyhelminthes with 5 parasites.
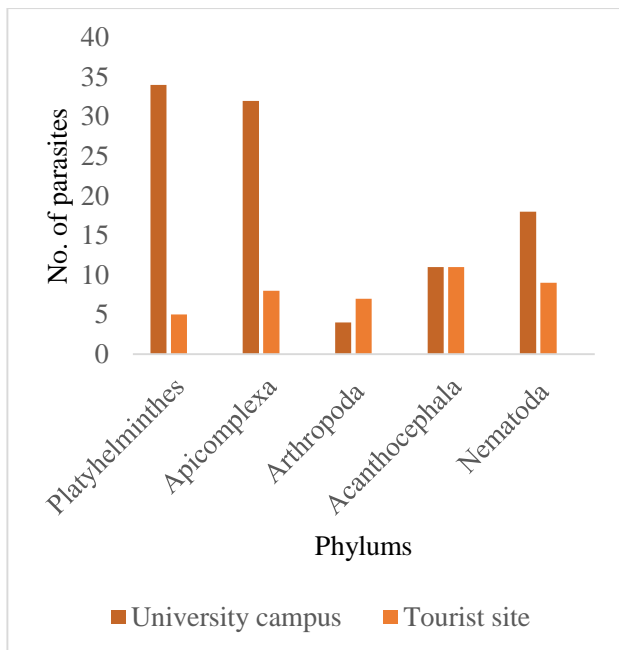
Figure 4. Comparisons of phylums of the identified parasites for both sampling sites

At university campus, the phylum Platyhelminthes had the highest number of identified parasites, but it was the opposite at the tourist site where the number of identified parasites from the phylum is the lowest. This can be related to the eating habits and living conditions of the long-tailed macaques. Improper hygiene source of foods can make the macaques more susceptible to infections. Flatworm infestations have been linked to poor water quality, poor livestock management, and food contamination with helminthes cysts, according to a prior study (Ukwubile & Bingari, 2018). Almost all phylums identified were endoparasites that are typically found in the intestines and feces except for phylum arthropoda (Mathison & Pritt, 2014). Most of the arthropoda are ectoparasites that live on the host. This findings can be related to the habits of *M. fascicularis* itself. They usually spend their time grooming themselves as well as others by using their fingers or mouth (Ilham et al, 2018; Fitriyah et al, 2021). Hence, this behaviour

increases the chance of the ectoparasites to be found inside their fecal.

Figure 5 shows the comparisons of identified parasites from the 5 phylums to their respective families for both sites. From phylum Platyhelminthes, there are 5 families which are Taeniidae, Schistosomatidae, Hymenolididae, Anoplocephalidae and Fasciolidae. The highest identified parasites from the phylum was from Schistosomatidae at university campus and Fasciolidae at tourist site. On the other hand, the lowest were from Taeniidae, Hymenolididae and Fasciolidae with each having only 4 parasites at university campus and there was no identication of any parasite from Schistosomatidae at the tourist site. For phylum apicomplexa, there were 2 families which were Sarcocytidae and Eimeriidae. In this phylum, Eimeriidae have higher number of parasites compared to Sarcocytidae for both the study sites. At the university campus, the Sarcocytidae had 3 parasites and Eimeriidae had 29 individual parasites which also makes it as the highest identified compared to all families of the phylums. At the tourist site, there were only 8 parasites that was from Eimeriidae and no parasites from Sarcocytidae.

For phylum Acantocephala, only one family was identified which was Giganthorhynchidae. From this family, there were 11 parasites identified for each of the study sites. For phylum Arthropoda, it can be divided into 4 families which were Listrophoridae, Pyroglyphidae, Analyoidae and Sarcoptidae. At the university campus, there was only one family identified which was Listrophoridae with 4 parasites. At the tourist site, the highest were 4 parasites that belong to Pyroglyphidae and other families only had one parasite each. Lastly, for phylum Nematoda, there were 5 families which were Ascarididae, Strongylidae, Trichostrongylidae, Trichuridae and Toxocharidae. At the university campus, Ascarididae had the most parasites with 6 parasites, and Strongylidae had the least with 1 parasite, while at the tourist spots, Toxocharidae had the most with 4 parasites, and Strongylidae, Trichostrongylidae, and Trichuridae each had only 1 parasite.
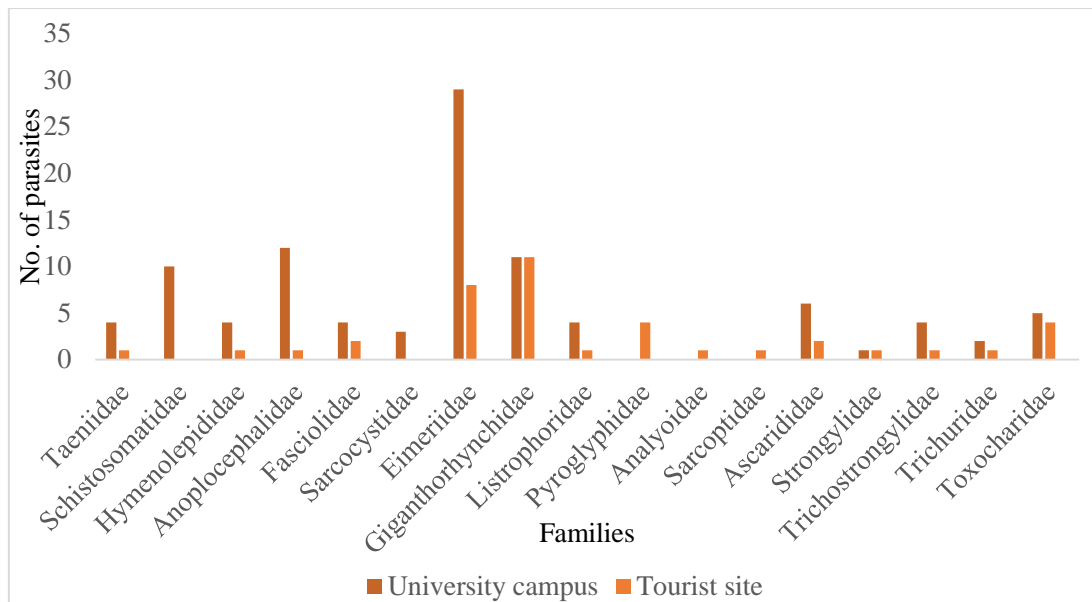
Figure 5. Comparison of the number of parasites to their respective families at both sites

Among all the families, the highest number of parasites that had been identified from the univesity campus was from Eimeriidae while for the tourist site was from Giganthorhynchidae. From the families obtained, there were a few genus that can be identified with some certainty. Table 2 shows gastrointestinal parasites that can be recognized up until its genus based on morphological identification. The most typical types of gastrointestinal parasites are helminthes and protozoans (Coumo et al., 2009). Many gastrointestinal parasites including *Trichuris* spp. and *Strongyloides* spp. often infect both humans and animals. Infection by these parasites can cause sub clinical symptoms to clinical symptoms of long duration with abdominal pain, diarrhea, dysentery and weight loss (Hechenbleikner & McQuade, 2015; Pumipuntu, 2018). Most of them have been reported to be zoonotic agents which have the ability to transmit between humans, livestock, companion animals and wildlife especially in their larval stage of infection (Lavikainen, 2010; Pumipuntu, 2018) and also as host to complete their life cycle (Adrus, et al., 2019). Most of it also can exist in the host by consumption of the infected eggs while eating foods (Viswanath & Williams, 2019). Usually fecal samples are taken in order to prove the gastrointestinal parasite (Hahn et al., 2003).

Trichuris spp., *Entamoeba* spp., and *Strongyloides* spp. are the most prevalent gastrointestinal parasites discovered in primates (Hahn et al., 2003; Trejo-Macias & Estrada, 2012; Mafuyai et al., 2013; Klaus et al., 2018). According to Valenta et al., (2017), macaques in human-occupied areas have a greater frequency of *Cryptosporidium* spp. infections than those in the wild. *Enterobius* spp., *Strongyloides* spp., *Trichuris* spp., *Entamoeba coli*, and *Entamoeba hystolytica* were shown to be more common in macaques that lived in human-inhabited regions (Ekanayake et al., 2006; Valenta et

al., 2017). Long-tailed macaques have been studied in the past to see how common gastrointestinal parasites occur (Lane et al., 2010; Wenz-Mucke et al., 2013; Zanzani et al., 2015). In comparison to long-tailed macaques, other primates' gastrointestinal parasites are not that different (Lane et al., 2010; Zanzani et al., 2015; Sricharern et al., 2016). Infection by these parasites can cause sub-clinical symptoms to clinical symptoms of long duration with abdominal pain, diarrhea, dysentery and weight loss (Hechenbleikner & McQuade 2015; Pumipuntu, 2018). The majority of them have been identified as zoonotic agents, meaning they may spread between people, cattle, companion animals, and wildlife, particularly during their larval stage of infection (Lavikainen, 2010; Pumipuntu, 2018).

The parasites are mostly prevalent in the host due to consumption of the infected eggs while eating foods (Viswanath & Williams, 2019). The numbers of identified parasites were higher at the campus compared to the tourist site which can be due to the sharing of space between the long-tailed macaques and human. The increasing human population can cause the loss of natural habitat for the long-tailed macaque. Anthropogenic effect has been characterised as promoting helminth infection measurements indirectly through several forms of intervention, such as increased host interaction and parasite transmission rates as a result of dietary resource delivery (Klaus et al., 2018). Furthermore, the growing human population has had an impact on the primate's ecosystem, making human-macaque interaction unavoidable. This relationship increases the risk of zoonotic disease transfer from macaque to human or vice versa, and this issue will have an impact not only on human health but also on macaque conservation (Gillespie, 2006).

Images	Genus	Numbers of identified parasites	
		University campus	Tourist site
	Taenia spp.	4	1
	Hymenolepis spp.	4	1
	Moniezia spp.	12	1
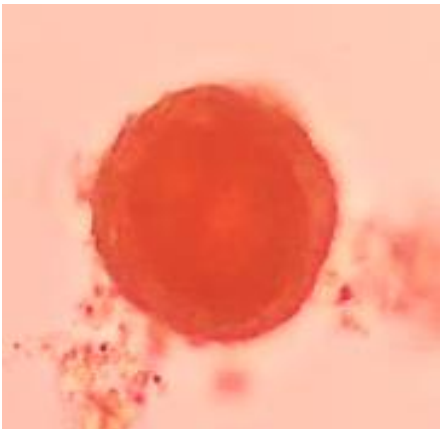
Strongyloids spp.   1   1

Trichostrongylus spp.   4   1

Trichuris spp.   2   1

Shown selected images of *Taenia* spp., *Hymenolepis* spp., *Moniezia* spp., *Strongyloids* spp., *Trichostrongylus* spp., and *Trichuris* spp. (40X magnification, under light microscope)

Table 3. Diversity indices of gastrointestinal parasites at the two sites

Sites	University campus	Tourist site
Taxa_S	34	15
Individuals	99	40
Dominance_D	0.047	0.120
Simpson_1-D	0.953	0.880
Shannon_H	3.282	2.399
Evenness_e^H/S	0.783	0.734

Table 3 shows the biodiversity indices of parasites in the university campus and tourist location. When compared to the number of taxa at the tourist location, the number of taxa on the university campus was greater. Dominance (D) is a metric for the most visible and numerous species. Diversity in the sense of evenness diminishes as D grows. Table 3 shows that dominance for university campus sites was 0.047 which was much lower than the value of 0.120 for tourism sites. This is further confirmed by the Simpson Index, which is often used as a supplement (1-D). The Simpson Index is a tool for comparing two collections of data to evaluate which is more diversified. This indicator has a range of 0 to 1, with higher values closer to 1 indicating greater diversity and lower scores closer to 0 indicating less diversity. It also shows that both sites had high numbers which were 0.953 and 0.880 for the university campus and tourist sites, respectively, that is closer to 1 which indicates high diversity.

Another statistic that is widely used to characterise a community's variety is the Shannon Index (H). Shannon's index takes into account the number of species present as well as their distribution. In most ecological studies, typical values range from 1.5 to 3.5, with the index seldom exceeding 4. The Shannon Index rises in proportion to the community's richness and evenness. The Shannon Index in Table 3 indicates that the university campus has a higher parasite abundance and species richness compared to the

Table 4. Two-sample t-test

Parameter	Value
Mean (University campus)	1.98
Mean (Tourist site)	1.33
p(same)	0.22

The use of a two-sample t-test is seen in Table 4. It is utilised to determine whether the mean values of the gastrointestinal parasites from the two locations are statistically different. PAST analysis was used for this test. The null hypothesis for this test was that the population averages from two independent, random samples drawn from an essentially normal distribution were equal. The p-value obtained from this test was 0.22, which was higher than the significance limit of 0.05. This showed that the null hypothesis was accepted and the population means of the sampling sites were not significantly different. This is probably due to unequal sample size, since at the university

tourist location, with values of 3.282 and 2.399, respectively. This is also supported by the value of evenness since the value for the campus site was also higher than the tourist site with values of 0.783 and 0.734, respectively. The differences might be attributable to the long-tailed macaques' differing food supplies at the sample sites. It is known that the habitat and source of foods have impact on the parasite pattern in macaques (Gillespie et al., 2005; Adrus, et al., 2019). Other than natural source of foods from trees, there is a difference source of food that can be seen from the sample sites. At the university campus, the macaques were frequently found rummaging at the dumpster and eat contaminated food from it while the macaques from the tourist site were often fed by the tourist with vegetables and fruits that were sold at that area. In contrast, high levels of provisioning and readily available sources of year-round food among monkey forests should result in a decrease in parasite prevalence, intensity, and diversity, because of the combined effects of better nutrition and minimization of time spent foraging, reducing potential exposure to parasite infective stages (Lane et al., 2010). Aside from that, non-human primates are frequently compelled to live in anthropogenically altered environments as a result of human population growth and deterioration of formerly natural ecosystems (Chapman & Peres, 2001; Wolfe et al., 2004). The presence of humans has a significant impact on the number of gastrointestinal parasites (Wenz-Mucke et al., 2013).

campus site there were 50 fecal samples and at the tourist site there were 30 fecal samples that affected the mean calculations.

4. Conclusion

A total of 139 parasites were found from both sample sites by using morphological identifications. They were classified into 5 phylums and 17 families. From 139 parasites, 33 parasites can be identified into 6 genus of GI parasites. Among the gastrointestinal parasites that were identified in *M. fascicularis* from the study sites, there are three parasites that were shown to be zoonotic positive namely *Strongyloids* spp*., Trichostrongylus* spp. and *Trichuris* spp. These parasites can be commonly found at the university campus due to consumption of unhygienic foods. They are the most common gastrointestinal parasites that can be found in the fecal and also can cause certain diseases which can disturb

the host's health and ultimately transmit to humans. The diversity index of GI parasites was higher at the university campus compared to the tourist site with values of 0.953 and 0.880, respectively for Simpson's Index while for the Shannon's Index, the values were 3.282 and 2.399, respectively. In conclusion, there are more parasites identified from the long-tailed macaques at the university campus than those at the tourist site. Therefore, suitable precautions are needed in order to avoid any possible parasite transmission.

5. Acknowledgements

6. References

Adrus, M., Zainuddin, R., Ahmad Khairi, N.H., Ahamad, M., Abdullah, M-T. (2019). Helminth parasites occurrence in wild proboscis monkeys (Nasalis larvatus), endemic primates to Borneo Island. J Med Primatol. 00:1–7.

Athaillah, F., Ginting, A.W.E., Rahmi, E., Hambal, M., Hasan, M., Erwin, E., Vanda, H. (2021). Identification of Gastrointestinal Protozoa in Long-Tailed Macaque (Macaca fascicularis) in Sabang. In 2nd International Conference on Veterinary, Animal, and Environmental Sciences (ICVAES 2020) (pp. 187-192). Atlantis Press.

Amato, K.R., Yeoman, C.J., Kent, A., Righini, N., Carbonero, F., Estrada, A., Gaskins, H.R., Stumpf, R.M., Leigh, S.R. (2013). Habitat Degradation Impacts Black Howler Monkey (Alouatta pigra) Gastrointestinal Microbiomes, International Society for Microbial Ecology 7: 1344-1353. DOI: https://doi.org/10.1038/ismej.2013.16

Anderson, R.C., Chabaud, A., & Willmott, S. (1974). CIH keys to the nematode parasites of vertebrates (No. QL 391. N4. C54). Commonwealth Institute of Helminthology.

Beisner, B.A., Balasubramaniam, K.N., Fernandez, K., Heagerty, A., Seil, S.K., McCowan, B., Sinha, R.P. (2016). Prevalence of Enteric Bacterial Parasites with Respect to Anthropogenic Factors Among Commensal Rhesus Macaques in Dehradun, India, Primates 57 (4): 459-469. DOI: 10.1007/s10329-016-0534-2

Bowman, D.D. (2003). Georgis' Parasitology for Veterinarians 8 th edition. WB Saunders Company.

Chapman, C.A., Bonnell, T.R., Gogarten, J.F., Schoof, V.A.M., Calme, S. (2005). Competing Pressures on Populations: Long-term Dynamics of Food Availability, Food Quality, Disease, Stress, and Animal Abundance, Phil. Trans. R. Soc. B 26: 370-382. DOI: https://doi.org/10.1098/rstb.2014.0112

Chapman, C.A., Peres, C.A. (2001). Primate Conservation in the New Millennium: The Role of Scientists, Evolutionary Anthropology 10:16–33.

Cuomo, M.J., Noel, L.B., White, D.B. (2009). Diagnosing Medical Parasites: A Public Health Officers Guide to Assisting Laboratory and Medical Officers. United States, OH: Air Education and Training Command, RANDOLPH AFB TX

Ekanayake, D.K., Arulkanthan, A., Horadagoda, N.U. et al. (2006). Prevalence of Cryptosporidium and Other Enteric Parasites Among Wild Non-human Primates in Polonnaruwa, Sri Lanka, Journal of Tropical Medicine and Hygiene 74: 322-331.

Engel, G., Jones-Engel, L. (2011). The Role of Macaca fascicularis in Infectious Disease Transmission. In Gumert, M.D., Fuentes, A. & Jones-Engel, L. (eds.). Monkeys on the Edge: Ecology and Management of Long-tailed Macaques and Their Interface with Humans, pp. 183–203. United Kingdom: Cambridge University Press, Cambridge.

Fitriyah, A., Wahyuningsih, E., Syaputra, M., Lestari, A.T. (2021). Survey of Long-tailed macaque's Behaviour in Mount Rinjani National Park, Lombok Timur. In IOP Conference Series: Earth and Environmental Science (Vol. 891, No. 1, p. 012028). IOP Publishing.

Gillespie, T.R., Chapman, C.A., Greiner, E.C. (2005). Effects of logging on gastro- intestinal parasite infections and infection risk in African primates. J Appl Ecol. 42: 699-707

Gillespie, T.R. (2006). Noninvasive Assessment of Gastrointestinal Parasite Infections in Free-ranging Primates, International Journal of Primatology 27 (4): 1129-1172.

Grant, E., Kyes, R.C., Kyes, P., Trinh, P., Ramirez, V., Tanee, T., Dangtakot, R. Pinlaor, P., Rabinowitz, P.M. (2019). Fecal Microbiota Dysbiosis in Macaques and Human within

Shared Environment, Public Library of Science ONE 14 (5): 134-156.

Hahn, N.E., Proulx, D., Muruthi, P.M., Alberts, S., Altmann, J. (2003). Gastrointestinal Parasites in Free-ranging Kenyan Baboons (Papio cynocephalus and P. anubis), International Journal of Primatology 24: 271-280.

Hambali, K., Ismail, A., Md-Zain, B.M., Amir, A., Karim, F. A. (2014). Diet of Long-tailed Macaques (Macaca fascicularis) at the Entrance of Kuala Selangor Nature Park (Anthropogenic Habitat): Food selection That Leads to Human-macaque Conflict, Acta Biologica Malaysiana 3 (2): 58–68.

Hechenbleikner, E.M., McQuade, J.A. (2015). Parasitic Colitis, Clinics in Colon and Rectal Surgery 28: 79-86.

Ilham, K., Nurdin, J., Tsuji, Y. (2018). Effect of provisioning on the temporal variation in the activity budget of urban long-tailed macaques (Macaca fascicularis) in West Sumatra, Indonesia. Folia Primatologica, 89(5): 347-356.

Karuppannan, K., Saaban, S., Mustapam A.R., Zainal Abidin, F.A., Azimat, N.A., Keliang, C. (2014). Population Status of Long-tailed Macaque (Macaca fascicularis) in Peninsular Malaysia, Journal of Primatology 3 (1): 34-37.

Kassim Norazila, Kamarul Hambali, Aainaa Amir. (2017). Nutritional Composition of Fruits Selected by Long-Tailed Macaques (Macaca fascicularis) in Kuala Selangor, Malaysia. Tropical Life Sciences Research 28 (1): 91–101.

Klaus, A., Strube, C., Roper, K.M., Radespiel, U., Schaarschmidt, F., Nathan, S., Goossens, B., Zimmermann, E. (2018). Fecal Parasite Risk in the Endangered Proboscis Monkey is Higher in an Anthropogenically Managed Forest Environment Compared to a Riparian Rain Forest in Sabah, Borneo, Public Library of Science ONE 13 (4): 110-122.

Lane, K.E., Holley, C., Hollocher, H., Fuentes, A. (2010). The Anthropogenic Environment Lessens the Intensity and Prevalence of Gastrointestinal Parasites in Balinese Long-tailed Macaques (Macaca fascicularis), Primates 52: 117-128.

Lastuti, N.D.R., Suwanti, L.T., Hastutiek, P., Kurniawati, D.A., Puspitasari, H. (2021). Molecular Detection of EntamoebaSpp in Long-tailed Macaque (Macaca Fascicularis) at Baluran National Park, Indonesia. Malaysian Journal of Medicine and Health Sciences, 17, 85-88.

Lavikainen, A. (2010). Human Medical View on Zoonotic Parasites, Acta Vet Scand 52 (1), 1-2.

Mafuyai, H.B., Barshep, Y., Audu, B.S., Kumbak, D., Ojobe, T.O. (2013). Baboons as Potential Reservoirs of Zoonotic Gastrointestinal Parasite Infections at Yankari National Park, Nigeria, African Health Sciences 13 (2): 252-254.

Mathison, B.A., Pritt, B.S. (2014). Laboratory identification of arthropod ectoparasites. Clinical microbiology reviews, 27(1): 48-67.

Md-Zain, B. M., Sha'ari, N. A., Mohd-Zaki, M., Ruslin, F., Idris, N. I., Kadderi, M. D., Idris, W. M. R. (2010). A Comprehensive Population Survey and Daily Activity Budget on Long-tailed Macaques of Universiti Kebangsaan Malaysia, Journal of Biological Science 10 (7): 608–615.

Md-Zain, B.M., Tarmizi, M.R., Mohd-Zaki, M. (2011). Campus Monkeys of Universiti Kebangsaan Malaysia: Nuisance Problems & Students Perception. In Gumert, M.D., Fuentes, A. & Jones-Engel, L. (eds.). Monkeys on The Edge: Ecology and Management of Long-Tailed Macaques and Their Interface with Humans, pp. 110–117. United Kingdom: Cambridge University Press, Cambridge.

Md-Zain, B.M., Ruslin, F., Idris, W.M.R. (2014). Human-macaque Conflicts at the Main Campus of Universiti Kebangsaan Malaysia, Pertanika Journal of Tropical Agricultural Science 37 (1): 73-85.

Mifsut, C.L. (2015). Helminths: Handbook for Identification and Counting of Parasitic Helminth Eggs in Urban Wastewater. Iwa Publishing.

Nunn, C.L., Altizer, S.M. (2006). Infectious Diseases in Primates: Behavior, Ecology and Evolution. Oxford University Press, Oxford.

Pumipuntu, N. (2018). Detection for Potentially Zoonotic Gastrointestinal Parasites in Long-tailed Macaques, Dogs and Cattle at Kosamphi Forest Park, Maha Sarakham, Veterinary Integrative Sciences 16 (2): 69-77.

Raja, T.N., Hu, T.H., Zainudin, R., Lee, K.S., Perkins, S.L., Singh, B. (2018). Malaria Parasites of Long-tailed Macaques in Sarawak, Malaysian Borneo: A Novel Species and Demographic and Evolutionary Histories, BMC Evolutionary Biology 18 (1): 49.

Rivera, W.L., & Kanbara, H. (1999). Detection of Entamoeba dispar DNA in macaque feces by polymerase chain reaction. Parasitology Research, 85(6), 493-495.

Sha, J.C.M., Gumert, M.D., Benjamin, P.Y.H.L., Jones-Engel. L., Chan, S., Fuentes, A. (2009). Macaque-human Interactions and the Societal Perceptions of Macaques in

Singapore, American Journal of. Primatology 71: 825–839.

Siregar, J.E., Faust, C.L., Murdiyarso, L.S., Rosmanah, L., Saepuloh, U., Dobson, A.P., Iskandriati, D. (2015). Non-invasive Surveillance for Plasmodium in Reservoir Macaque Species, Malaria Journal 14: 404-412.

Sricharern, W., Inpankaew, T., Keawmongkol, S., Supanam, J., Stich, R.W. & Jittapalapong, S. (2016). Molecular Detection and Prevalence of Giardia duodenalis and Cryptosporidium spp. Among Long-tailed Macaques (Macaca fascicularis) in Thailand, Infection, Genetics and Evolution 40: 310–314.

Trejo-Macias, G., Estrada, A. (2012). Risk Factors Connected to Gastrointestinal Parasites in Mantled Alouatta palliata mexicana and Black Howler Monkeys Alouatta pigra Living in Continuous and in Fragmented Rainforests in Mexico, Current Zoology 58 (3): 375-383.

Ukwubile, C.A., Bingari, M.S. (2018). Flatworms (Platyhelminthes) Associated with Slaughtered Cows in Abattoirs Found in Bali Town Taraba State Nigeria, International Journal of Research (6): 18-22.

Ungar, P.S. (1996). Feeding Height and Niche Separation in Sympatric Sumatran Monkeys and Apes, Folia Primatologica 6 (1): 163–168.

Valenta, K., Twinomugisha, D., Godfey, K., Liu, C., Schoof, V.A.M., Goldberg, T.L., Chapman, C.A. (2017). Comparison of Gastrointestinal Parasite Communities in Vervet Monkeys, Integrative Zoology 12 (6): 512-520.

Verweij, J.J., Vermeer, J., Brienen, E.A., Blotkamp, C., Laeijendecker, D., van Lieshout, L., Polderman, A.M. (2003). Entamoeba histolytica Infections in Captive Primates, Parasitology Research 90:100–103.

Viswanath, A., Williams, M. (2019). Trichuris trichiura (Whipworm, Roundworm). In: StatPearls [Internet]. Treasure Island (FL): StatPearls

Wallis, J. (2000). Prevention of Disease Transmission in Primate Conservation, Annals of the New York Academy of Sciences 916: 691-693.

Webber, A.D., Hill, C.M., Reynolds, V. (2007). Assessing the Failure of a Community-based Human-wildlife Conflict Mitigation Project in Budongo Forest Reserve, Uganda, Oryx 41: 117-125.

Wenz-Muecke, A., Sithithaworn, P., Petney, T.N., Taraschewski, H. (2013). Human Contact Influences the Foraging Behaviour and Parasite Community in l\Long-tailed Macaques, Parasitology 140 (6): 709-719.

Wolfe, N.D., Tassey-Prosser, A., Carr, J.K., Tamoufe, U., Mpoudi-Ngole, E., Ndongo Torimiro, J., LeBreton, M., McCutchan, F.E., Birx, D.L., Burke, D.S. (2004). Exposure to Non-human Primates in Rural Cameroon, Emerging Infectious Diseases 10: 2094–2099.

Zanzani, S.A., Gazzonis, A.L., Epis, S., Manfredi, M.T. (2015). Study of the Gastrointestinal Parasitic Fauna of Captive Non-human Primates (Macaca fascicularis), Parasitology Research 6 (2):1.

ESTIMATION OF THERMODYNAMIC PARAMETERS OF Ni-Si BASE ALLOYS USING THE SEMI-EMPIRICAL MIEDEMA MODEL

Ali Kadhim Alsaedi[1a]*, Faiz Salih Abbas[2a], Azhar S. Alaboodi[3a], and Ali Abid Abojassim[4a]

Abstract: In this paper, we present a calculation method for evaluating the possibility of enhancing the thermal stability of nickel silicide by alloying with metals, which consists in determining the formation enthalpy (ΔH) of nickel silicide using the Miedema model. Changes in formation enthalpy (ΔH) were observed for nickel silicides that were alloyed with Mo, Pt, Pd, W, and Zr. The MAAT (Materials Analysis Applying Thermodynamics) software was used to calculate and plot the formation enthalpy of binary and ternary systems. Based on our calculations, we found that in binary systems, the optimum values to expand the formation enthalpy were ⏤51.28 and ⏤49.57 kJ/mol for nickel silicide alloys. For the ternary system, the results showed that adding Zr could increase monosilicide phase stability.

Keywords: Miedema model, Formation enthalpy, Ni-Si alloys

1. Introduction

Nickel monosilicide (NiSi) is a promising material for microelectronics, and it is mainly used due to its low resistivity (12–14 μOhm·cm), low formation temperature (T = 350–500°C), and compatibility with silicon and germanosilicide technologies (Chi et al., 2007). However, during high-temperature treatment (T ≥ 700°C), several problems arise, associated with the agglomeration of a thin film of nickel silicide and the phase transition to the highly resistive NiSi2 compound due to a sharp increase in the specific resistance of the material. The phase transformation of NiSi to NiSi2 leads to an increase in leakage currents and a deterioration in the morphology of the silicide/silicon interface.

To expand the application range for the nickel monosilicide phase in the nickel–silicon system, thermal stability should also be increased. Therefore, approaches to increasing the NiSi thermal stability compound have attracted much interest in the last decade. One possible solution is doping silicon single crystals with $〚BF〛\_2^+$ or F+ ions (Wong et al., 2002). The introduction of $〚BF〛\_2^+$ or F+ ions ensures the stable existence of the NiSi phase up to a temperature of T = 750°C, at which NiSi2 is usually formed. This effect is due to the segregation of fluorine at the silicide/silicon (001) interface and at the silicide grain boundaries, which slows down the growth of NiSi grains.

Consequently, the presence of $〚BF〛\_2^+$ or F+ ions in the silicon substrate leads to an improvement in the uniformity of the monosilicide film and the formation of smaller grains. However, due to the possible ingrowth of silicon grains into the silicide layer and additional defects introduced by fluorite, this method cannot be considered an optimal way to increase thermal stability. The second method used to increase the morphological and phase stability of nickel silicide is doping nickel silicide with various metals or introducing a metal sublayer between nickel and silicon.

In particular, the studies (Huang et al., 2007; Shao et al., 2006; Gao et al., 2009) on the addition of the metals Pt, Pd, Ru, and Zr showed that such alloying has an influential effect on both the temperature stability and the morphological homogeneity of the surface and the NiSi/Si interface. The assessment of thermal stability was carried out based on the phase analysis of the Ni-Si system at different annealing temperatures using X-ray diffraction analysis and Raman spectroscopy (Gao et al., 2009; Skobelev et al., 2021).

This paper considers a calculation method for assessing the thermal stability of nickel silicide alloys with metals and the possibility of increasing it. This is achieved by using the Miedema model based on the determination of the formation enthalpy of nickel silicide (Steeneken & Houtgast, 1980). The analysis of changes in the thermal stability of nickel silicides doped with metals Mo, Pt, Pd, W, and Zr is carried out.

Authors information:

[a]Department of Physics, University of Kufa, Najaf, IRAQ.
Email: aliak.alsaaedi@uokufa.edu.iq[1];
faezs.muhammad@uokufa.edu.iq[2];
azhars.hamza@uokufa.edu.iq[3];
ali.alhameedawi@uokufa.edu.iq[4]
*Corresponding Author: aliak.alsaaedi@uokufa.edu.iq

2. Thermodynamic Analysis

Miedema Model

The two main parameters on which the formation enthalpy of a specific phase of metal alloys depends are the sign and the value. Therefore, we calculate the formation enthalpy for both binary and ternary systems according to the semi-empirical Miedema model (Steeneken & Houtgast, 1980; Wang et al., 2004).

We present the calculation of the formation enthalpy of phases for both undoped and doped nickel silicides. Undoped nickel silicides are nickel silicides formed by the solid-phase reaction of a film of nickel and silicon, whereas doped nickel silicides are compounds formed by the solid-phase reaction of a nickel film containing an alloying addition, for example, a transition metal, and silicon. The concept of nickel silicides used in this work includes three phases: a nickel-rich phase (Ni_2Si), a nickel monosilicide phase ($NiSi$), and a nickel disilicide phase ($NiSi_2$).

Since the results of recent experimental work (Gao et al., 2009; Skobelev et al., 2021) predict the possibility of increasing the thermal stability of nickel silicides with the addition of several elements, we analyse and calculate the formation enthalpy of nickel silicides with different compositions.

The semi-empirical Miedema model (Steeneken & Houtgast, 1980; Chelikowsky, 1982) allows direct calculation of the formation enthalpy of liquid and solid alloys containing atoms of both transition and non-transition metals. In the Miedema model, each atom is described by two parameters: the chemical potential, ϕ^*, and the averaged electron density over the surface of the Wigner–Seitz cell, $n_{WS}^{1/3}$. The Miedema model assumes that there are two mechanisms that contribute to the formation enthalpy of binary alloy systems: the first is proportional to ϕ^{*2} and is associated with charge transfer between neighbouring cells due to attractive forces, and the second is proportional to $n_{WS}^{2/3}$ and takes into account the repulsive forces due to surface tension.

Using the results of calculating the formation enthalpy of the binary system, obtained according to the Miedema model (Steeneken & Houtgast, 1980; Wang et al., 2004; Sharma & De Datta, 1986), we write the expression for the heat of formation:

$$\Delta H_{AB} = C_A^B\, X_A \Delta H_{A\,\text{in}\,B} + C_B^A X_B \Delta H_{B\,\text{in}\,A}) \qquad (1)$$

The concentration functions C_A^B and C_B^A are given by

$$C_A^B = X_A^S\left[1 + \beta(X_A^S X_B^S)^2\right] \qquad (2)$$

$$C_B^A = X_B^S\left[1 + \beta(X_A^S X_B^S)^2\right] \qquad (3)$$

The factor β has different values, 0, 5, and 8, which refer to soli solution, metallic glasses, and intermetallic, respectively.

The surface concentrations by X_A^S and X_B^S are represented by

$$X_A^S = \frac{X_A\, V_A^{\frac{2}{3}}}{X_A\, V_A^{\frac{2}{3}} + X_B\, V_B^{\frac{2}{3}}} \qquad (4)$$

$$X_B^S = \frac{X_B\, V_B^{\frac{2}{3}}}{X_A\, V_A^{\frac{2}{3}} + X_B\, V_B^{\frac{2}{3}}} \qquad (5)$$

Also, the interfacial enthalpy $\Delta H_{A\,\text{in}\,B}$ for mixing of A in B is described by

$$\Delta H_{A\,\text{in}\,B} = \frac{P\, V_A^{2/3}}{(n_{WS}^{-1/3})_{av}} \times \left[-(\Delta\phi^*)^2 + {}^Q\!/_P \left(\Delta n_{WS}^{1/3}\right)^2 - R^*\!/_P\right]$$

$$(6)$$

Here, the terms VA, Φ^*, and nWS represent the molar volumes of A and B, the constituent element work function, and the density of electrons, respectively. P, Q, and R* are constants. Constant P has values of 14.2 and 10.7 (Alsaedi et al., 2020; Imani & Enayati, 2017; Li, 2014). The metal status of being transitioned or non-transitioned describes this difference in P values. In addition, P/Q has a value of 9.4. R* appears as an additional term for the enthalpy in Eq.6 for transition/non-transition metals.

Table 1. The values of the electron density at the boundary of the Wigner–Seitz cell, $n_{WS}^{1/3}$, experimentally obtained in [7], and the values of $n_{CWS}^{1/3}$ calculated in this study.

Metal	Atomic radius (nm)	$n_{ws}^{1/3}$ (d. u)$^{1/3}$	ϕ^*(V)	$V_m^{2/3}$ (cm)^2
Si	0.118	1.50	4.70	4.20
Ni	0.124	1.75	5.20	3.50
Mo	0.140	1.77	4.65	4.40
W	0.141	1.81	4.80	4.50
Zr	0.160	1.39	3.40	5.80
Pd	0.137	1.67	5.45	4.30
Pt	0.139	1.78	5.65	4.40

3.   Results and Discussion

Figure 1 shows the formation enthalpy (ΔH) of the binary systems Ni-Pd, Si-Pd, Ni-Pt, Si-Pt, Ni-Zr, Si-Zr, Ni-Mo, Si-Mo, Ni-W, Si-W, and Ni-Si. Furthermore, Figure 1 reveals that the binary systems Ni-Si, Si-Pd, Si-Pt, Ni-Zr, Si-Zr, Si-Mo, and Si-W are more stable because the values of the formation enthalpy are negative for all composition values. The highest negative value was found in the binary system Si-Zr (�49.57 kJ/mol), and the lowest negative value was observed in Ni-Zr (�13.31 kJ/mol). The curve has two minimal points near x_{Ni} ~ 0.2 and x ~ 0.7. This indicates that in a binary system, the formation of these phases results from the stored energy released by a thermodynamic force.

The ΔH values of binary systems Ni-Mo, Ni-Pd, Ni-Pt, and Ni-W were positive for all composition values. This indicates that the formation of these binary systems is impossible under standard conditions, demonstrating that there is no strong interaction between the atoms. The reason for this behaviour could be the small differences between the electron negativities, atomic volumes, and electron densities of the atoms, as shown in Table 1.
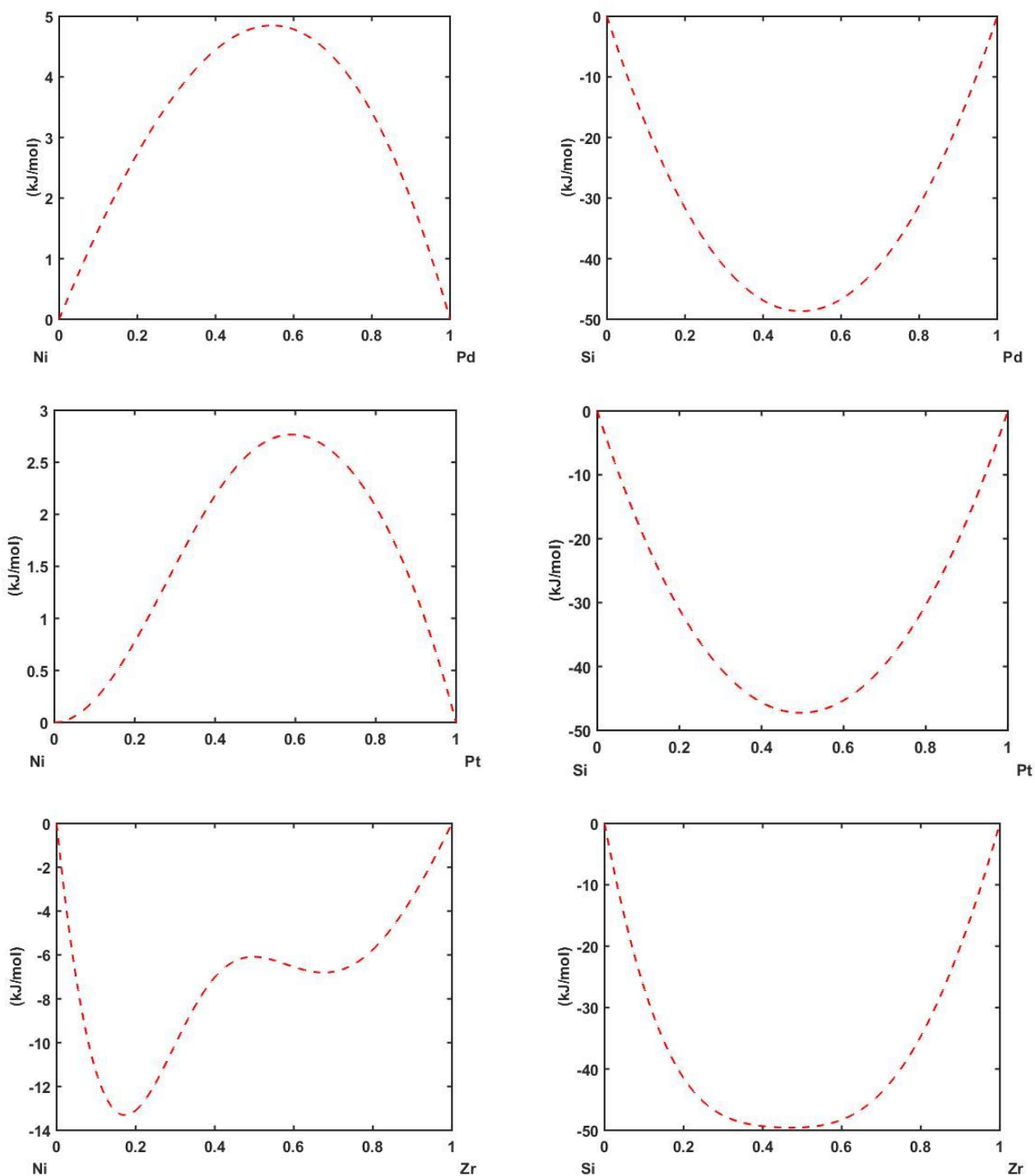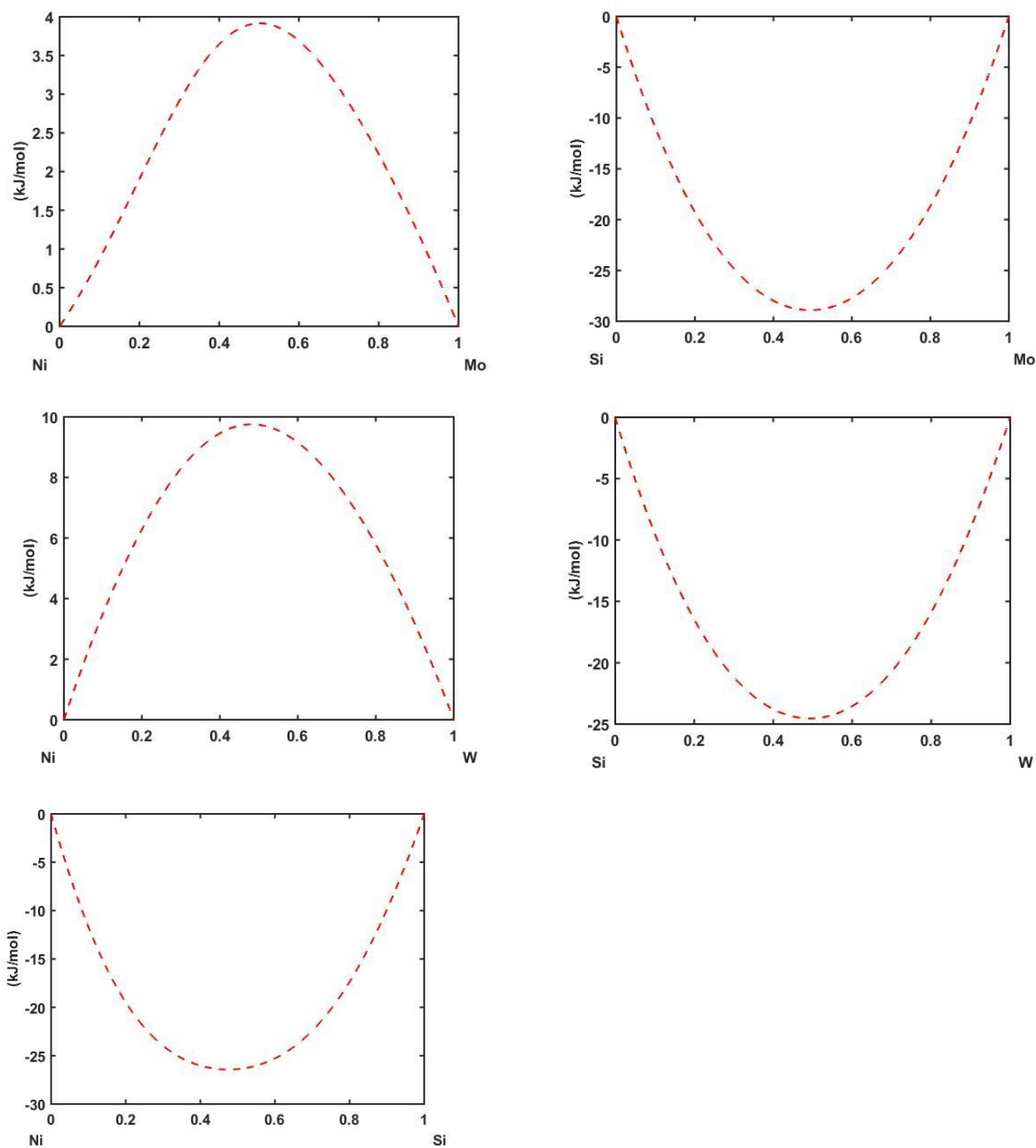
Figure 1. The formation enthalpy of the binary systems Ni-Pd, Si-Pd, Ni-Pt, Si-Pt, Ni-Zr, Si-Zr, Ni-Mo, Si-Mo, Ni-W, Si-W, and Ni-Si.

Figure 2 shows the formation enthalpy of the ternary system of nickel silicides doped with Pd, Pt, Zr, Mo, and W, and it shows that the addition of Zr, Pd, and Pt in the composition of the nickel film leads to the most negative values of the formation enthalpy of doped nickel silicide (⁻49.62, ⁻48.67, ⁻46.80 kJ/mol for Zr, Pd, and Pt, respectively). This means that for the conversion of nickel monosilicide into nickel disilicide, it will be necessary to spend more energy and, consequently, heat, which will lead to an increase in the process temperature.

The more negative the value of the formation enthalpy, the more stable the connection and the stronger the bond between silicon and metal atoms. As a result, it is more difficult to break it for the formation of a disilicide. As can be seen, it is precisely the more negative value of the formation enthalpy of nickel silicide due to the addition of an alloy element to the composition of the compound that leads to an improvement in its thermal stability.

The data in Figure 2 show that the addition of elements such as Mo and W leads to less negative values of the formation enthalpy of nickel disilicide than the formation enthalpy of pure nickel disilicide (−26.43 and −25.97 kJ/mol for Mo and W, respectively). However, the experimental data (Huang et al., 2007; Shao et al., 2006) indicate that the addition of these elements, albeit insignificantly, increases the thermal stability of nickel monosilicide, which might be due to the influence of other factors, for example, an improvement in the morphology of the interface and a slowdown in the growth of grains in the NiSi2 phase.
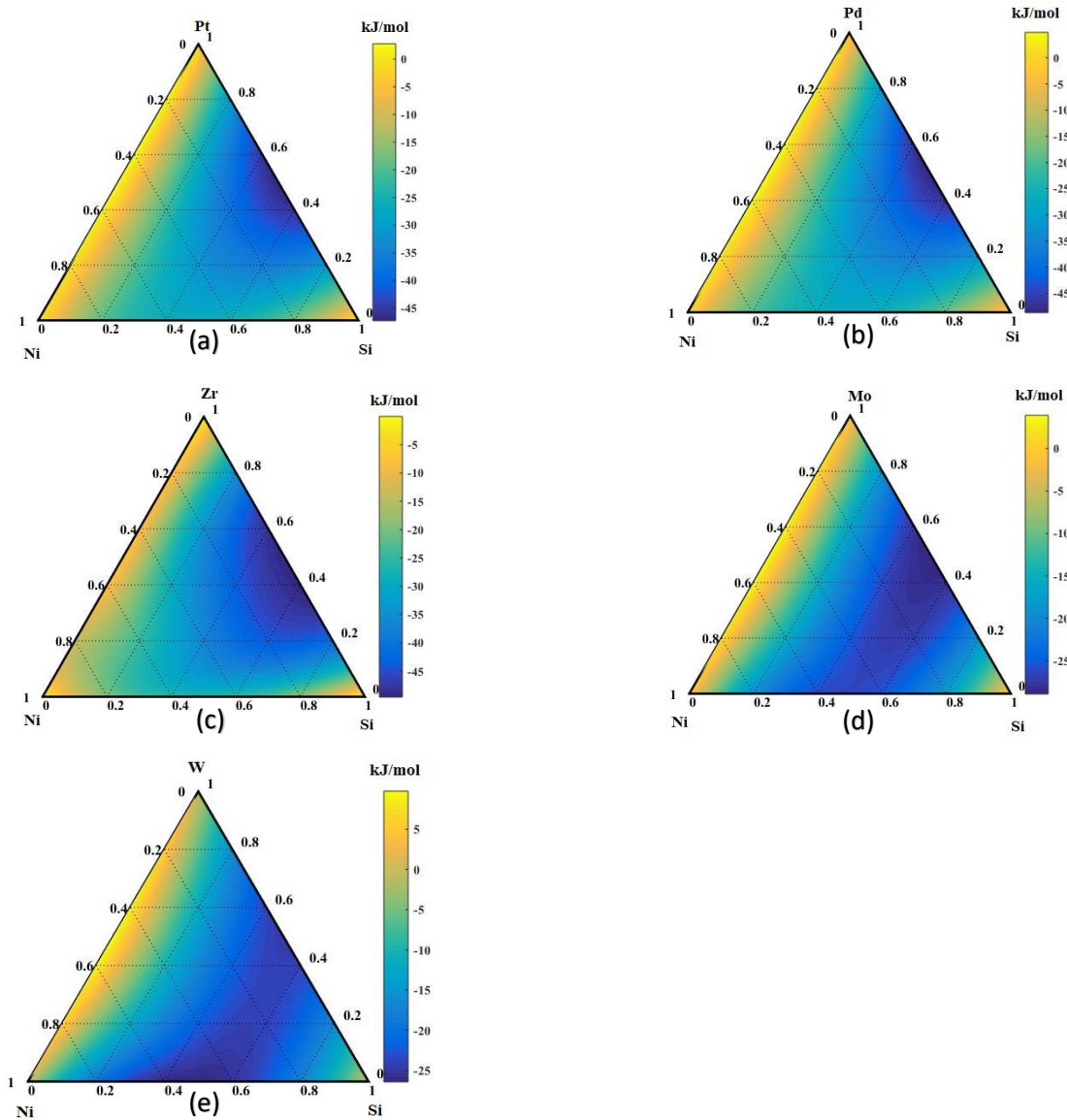
Figure 2. Formation enthalpy of ternary systems: (a) Ni-Pd-Si, (b) Ni-Pt-Si, (c) Ni-Zr-Si, (d) Ni-Mo-Si, and (e) Ni-W-Si.

4. Conclusions

The semi-empirical Miedema model is a good approach to calculating the thermodynamic properties of solid solution and amorphous binary and ternary systems. In this work, the MAAT software was used to calculate and plot the formation enthalpy of binary and ternary systems. A preliminary assessment was made to investigate the effectiveness of adding certain types of elements to increase the thermal stability of nickel monosilicide based on the calculations of the formation enthalpy of the Ni-Si phase for doped nickel silicides. The values of the formation enthalpy of the nickel monosilicide phase with the addition of the alloy elements Pd, Pt, Zr, Mo, and W were calculated based on the use of the semi-empirical Miedema model. Here, the most negative value of the formation enthalpy of doped nickel silicide was found to be (-49.67 kJ/mol), which is 2 kJ/mol more than the formation enthalpy of undoped nickel silicide.

5. References

Alsaedi, A. K., Ivanova, A. G., Habieb, A. A., & Almayahi, B. A. (2020). Estimation of the functions of some iron-based ternary systems within Miedema model and comparison with experiment. Results in Physics, 16, 102969.

Chelikowsky, J. R. (1982). Microscopic basis of Miedema's theory of alloy formation. Physical Review B, 25(10), 6506.

Chi, D. Z., Lee, R. T. P., & Wong, A. S. W. (2007). Addressing materials and integration issues for NiSi silicide contact metallization in nano-scale CMOS devices. Thin Solid Films, 515(22), 8102–8108.

Gao, B., Hu, F. X., Wang, J., Shen, J., Sun, J. R., & Shen, B. G. (2009). Influence of the substitution of Cu for Si on magnetic entropy change and hysteresis loss in LaFe11.7(Si1 – xCux)1.3 compounds. Journal of Applied Physics, 105(7), 07A916.

Huang, W., Zhang, L., Gao, Y., & Jin, H. (2007). Effect of a thin W, Pt, Mo, and Zr interlayer on the thermal stability and electrical characteristics of NiSi. Microelectronic Engineering, 84(4), 678–683.

Imani, M. H. E. M., & Enayati, M. H. (2017). Investigation of amorphous phase formation in Fe-Co-Si-BP – Thermodynamic analysis and comparison between mechanical alloying and rapid solidification experiments. Journal of Alloys and Compounds, 705, 462–467.

Li, H., Sun, X., & Zhang, S. (2014). Calculation of thermodynamic properties of Cu-Ce binary alloy and precipitation behavior of Cu6Ce phase. Materials Transactions, 55(12), 1816–1819.

Shao, J., Lu, J., Huang, W., Gao, Y., Zhang, L., & Zhang, S. L. (2006). Raman spectral study on the thermal stability of Ni/Zr/Ni/Si and Ni/Co/Ni/Si structures. Journal of Raman Spectroscopy, 37(9), 951–953.

Sharma, P. K., & De Datta, S. K. (1986). Physical properties and processes of puddled rice soils. In Advances in soil science (pp. 139–178). New York, NY: Springer.

Skobelev, S. A., Balakin, A. A., Anashkina, E. A., Andrianov, A. V., & Litvak, A. G. (2021). Ultrawide shifting of the laser pulse wavelength in a multicore tellurite fiber with two zero-dispersion wavelengths. Physical Review A, 104(3), 033518.

Steeneken, H. J., & Houtgast, T. (1980). A physical method for measuring speech-transmission quality. The Journal of the Acoustical Society of America, 67(1), 318–326.

Wang, R. N., He, Y., & Feng, J. Y. (2004). Explanation of the enhancement of NiSi thermal stability according to TFD equations and Miedema's model. Nuclear Instruments and Methods in Physics Research Section B: Beam Interactions with Materials and Atoms, 222(3–4), 462–468.

Wong, A. S. W., Chi, D. Z., Loomans, M., Ma, D., Lai, M. Y., Tjiu, W. C., ... & Greene, J. E. (2002). F-enhanced morphological and thermal stability of NiSi films on BF_2^+-implanted Si(001). Applied Physics Letters, 81(27), 5138–5140.

PHOTOPROTECTIVE EFFECTS OF CARRAGEENANS AGAINST ULTRAVIOLETB-INDUCED EXTRACELLULAR MATRIX (ECM) DAMAGE IN KERATINOCYTES

Haema Thevanayagam[1a], Shar Mariam Mohamed[2a]*, Wan-Loy Chu[3a] and Zolkapli Eshak[4b]

Abstract: Carrageenans, the polysaccharide from red seaweeds, are widely used in food, medicine and as an excipient in cosmetics and skincare products. Carrageenans have shown a prospective photoprotective effect against ultraviolet B (UVB) irradiation on immortalised normal human keratinocyte (HaCaT) cells. This research evaluated the photoprotective effect of iota (ι), kappa (κ)-carrageenans and their combination with vitamin E against UVB-induced extracellular matrix (ECM) damage in HaCaT cells. The study also assessed the superoxide dismutase (SOD) and catalase (CAT) antioxidant enzymes in UVB-exposed pre-treated and non-pre-treated cells. The parameters assessed were biological mediators important for the structural integrity of ECM, comprising of epidermal growth factor receptor (EGFR), mitogen-activated protein kinase (MAPK), activating protein- (AP-1) and matrix metalloproteinases (MMPs), liberated by the UVB exposed cells. Enzyme-linked immunosorbent assay was used to evaluate the release of these mediators. Carrageenans enhanced the activities of the antioxidant enzymes SOD and CAT, which acts as a defence mechanism against oxidative stress. The levels of the biological mediators were also reduced in cells pre-treated with carrageenans, suggesting that the polysaccharide has the potential to retain skin's structure by reducing the damage to ECM upon UVB exposure. In conclusion, the results imply that carrageenans possess photoprotective effects against UVB-induced ECM damage and stimulate antioxidant enzymes.

Keywords: ultraviolet B (UVB), photoaging, extracellular matrix, antioxidant enzymes, carrageenan

1. Introduction

Ultraviolet radiation (UVR) causes not only skin cancer but also photoaging (Rabe et al.,2006), a cumulative process characterised by clinical, histological and biochemical changes in skin that makes one appear aged (Berneburg et al.,2000). The extent of damage to the extracellular matrix (ECM) following UVB exposure could be understood by the initiation of epidermal growth factor receptor (EGFR), mitogen-activated protein kinase (MAPK), activating protein-1 (AP-1) and matrix metalloproteinases (MMPs) liberated by the cells. These biological mediators are important in a cell's structural integrity and help keep a cell in shape.

Ingredients with anti-inflammatory, antihistamine or antioxidant properties such as vitamin E, vitamin A, green tea extract and polyphenols are incorporated for photoprotection (Davis & Callender,2010) as topical skin care products or sunscreens. However, not all sunscreens grant an antioxidant effect, and not all antioxidants produce a sunscreen effect (Lin et al.,2005). Algae and their extracts are increasingly recognised in skin care regimes. They are used in cosmetics either as an excipient or therapeutic agent (Agatonovic-Kustrin & Morton,2013). Carrageenans are used in cosmetics as an excipient to improve lubricity and softness. They are high molecular weight polysaccharides extracted from red seaweeds (Rhodophyceae) cell wall and intercellular matrix (Kalitnik et al.,2013), mostly of the genera Chondrus, Eucheuma, Gigartina and Iridea with 15% to 40% ester-sulphate content (Necas & Bartosikova,2013). Due to the thickening water-binding nature, carrageenans are incorporated into sunscreens, anti-ageing creams, facial creams, and soap (Campo et al.,2009). Although extensively used as an excipient, the value of carrageenans as a photoprotective or therapeutic agent for skin has not been explored, especially in their protective effect against UV damage.

The photoprotective property of carrageenans is expected to be contributed by their sulphur moieties, polysaccharide nature, mineral content and gelling property. Due to their sulphated characteristic (Zhang et al.,2010),

Authors information:

[a]School of Postgraduate Studies, International Medical University, 126 Jalan Jalil Perkasa 19, Bukit Jalil, 57000 Kuala Lumpur, MALAYSIA. Email: haematheva@gmail.com[1]; sharmariam_mhd@imu.edu.my[2];wanloy_chu@imu.edu.my [3]

[b]Faculty of Pharmacy, University Teknologi Mara Puncak Alam Campus, FF1 Building, Bandar Puncak Alam, 42300, Selangor, MALAYSIA. Email: zolkapli_eshak@puncakalam.uitm.edu.my[4]
*Corresponding Author: sharmariam_mhd@imu.edu.my

carrageenans possess antioxidant activity by quenching free radicals induced by UVR (Yuan et al.,2006). Photoprotective effects of carrageenans on HaCaT and Mouse Embryonic Fibroblasts (MEF) cells (Ren et al.,2010) and antioxidative (Sokolova et al.,2011) activities have been reported. Our previous study showed the ability of carrageenans to act as an antioxidant against reactive oxygen species (ROS) in UVB-induced HaCaT cells, along with their photoprotective and anti-inflammatory properties (Thevanayagam et al.,2014). Incorporating photoprotective agent into cosmetic products is desirable. Combining several antioxidants is a therapeutic approach to reducing photoaging and skin cancer incidence. Hence, the potential use of carrageenans as the main compound for photoprotection is worth exploring.

Pathologically, photoaging is characterised by the abnormal structure and alteration of the dermal connective tissue and ECM (Hwang et.al.,2011). Such effects impair skin function, causing it to look aged (Quan et al.,2009). Extreme change of biochemical mediators causes degradation of ECM. A complex cascade of biochemical reactions in the human skin is triggered by UVR. These biological mediators are of importance to be studied since photoprotection could be achieved if the release of these mediators could be manipulated via effective treatment.

In UVB-exposed skin, keratinocytes absorb the radiation, generates ROS along with impaired natural antioxidants, leads to a flow of events starting with the stimulation of EGFRs (Saeed et al.,2012) followed by MAPK signalling (Rabe et al.,2006) that induces AP-1 (Wen et al.,2012) and leads to the transcription of MMPs, (Pandel et al.,2013) enzymes responsible for ECM and collagen degradation that promotes wrinkle and metastases (Brenneisen et al.,2002). Dermal fibroblasts and epidermal keratinocytes have MMP expression (Yasui & Sakurai, 2003). The MMPs include MMP-1 (collagenase), which degrades collagen types I and III; MMP-9 (gelatinase B) further breakdowns collagen and MMP-3 (stromelysin) degrades collagen type IV (Herouy, 2001; Sachs et al., 2009). The ability of carrageenans and/or vitamin E treatment to suppress these mediators in UVB-exposed HaCaT is expected to protect the ECM and integrity of the skin, hence shielding against photoaging.

This study aims to assess the photoprotective action of carrageenans against UVB-induced damage in keratinocytes. The assessment was based on the quantification of biological mediators liberated by UVB-induced cells. The effect of carrageenans on superoxide dismutase (SOD) and catalase (CAT) was also assessed. This study has incorporated a novel use of carrageenans in protecting UVB-induced ECM degradation in keratinocytes. Apart from being an excipient, carrageenan is a potentially photoprotective agent. These findings will be a breakthrough in the field of dermatology and cosmeceutical, and our results will create a paradigm for future studies in the evolution of carrageenans for photodamage prevention and treatment.

2. Materials and Methods

2.1 Cell culture

Immortalised normal human keratinocyte (HaCaT) cells from cell line services (CLS) (Germany) were cultured and maintained in Dulbecco's Modified Eagle medium (DMEM) supplemented with 10% heat-inactivated fetal bovine serum (FBS, GIBCO Life Technologies, USA), 1% penicillin-streptomycin (10,000 units of penicillin (base) and 10,000 µg of streptomycin (base) ml^{-1}, GIBCO Life Technologies), and stored at 37°C in an atmosphere of 5% CO_2 and 99% humidity incubator.

2.2 Carrageenans

Two isomers of purified food-grade carrageenans, namely iota (ι)-carrageenan from Eucheuma denticulatum and kappa (κ)-carrageenan from Eucheuma cottonii (PT. Wahyu Putra Bimasakti, Indonesia) were used. Vitamin E (Vit-E) (α-tocopherol) of 96% purity from Sigma Aldrich, USA, was positive control. Dimethyl sulfoxide (DMSO) (Thermo Fisher Scientific, USA) was used to dissolve stock solutions of ι, κ and vit-E. For subsequent experiments, compounds were taken from stock solutions and diluted to the desired concentrations using complete DMEM.

2.3 Setup for UVB

The UV source was a UVB lamp (Uvitec, UK) emitting UV radiation at 312 nm. The UVB intensity was measured using a UVA/B light meter (Sper Scientific, USA), and a constant intensity of 1.17 mW was maintained throughout the study. The time of exposure was varied to obtain the different UVB fluences.

2.4 Treatment

Four sets of cells used are as below:
  a) Control (cells alone): Cells without treatment or irradiation.
  b) Cells pre-treated with carrageenans and/or vit-E without UVB irradiation.
  c) Cells subjected to UVB irradiation without pre-treatment.
  d) Cells pre-treated before UVB irradiation.

For all the tests, ι, κ, vit-E and the combination of ι and vit-E, and κ and vit-E at a final concentration of 12.5 µg/mL were added in triplicate into microplate wells containing 2x10⁴ cells/mL unless stated otherwise. For the combination solution, equal volume and concentration of individual

chemicals were added to a final concentration of 12.5 µg/mL. After treatment, the samples were incubated for 24 hours as pre-treatment time. After 24 hours, the culture medium was replaced with fresh medium before being irradiated with UVB at 100 and 300 mJ/cm². The plates were incubated for 24 hours as a recovery period. All experiments were carried out in triplicate unless stated otherwise.

2.5 Effect of UVB on biochemical mediators and antioxidant enzymes

2.5.1 SOD and CAT

SOD and CAT were detected using The OxiSelect Superoxide Dismutase Activity Assay and The OxiSelect Catalase Activity Assay kit (Cell Biolabs', USA) according to the manufacturer's protocols. The extracellular SOD activity was determined based on the inhibition of the superoxide anion by each test group. The percentage of inhibition following equation 1 was calculated by comparing the optical density (OD) of the blank and samples. A catalase standard curve was plotted, a trend line of a second order polynomial was established, and the chart equation was used to calculate CAT activity.

$$\textbf{SOD Activity (inhibition \%)} = \frac{\textbf{ODblank} - \textbf{ODsample}}{\textbf{ODblank}} \textbf{ X 100}$$
(1)

2.5.2 EGFR and phosphorylated EGFR

The intracellular EGFR and its activation (Phosphorylated EGFR) form were detected using the Pierce In-Cell Colorimetric ELISA Kit (Thermo Fisher Scientific, Illinois, USA) per the manufacturer's protocols. The HaCaT cells were cultured in a 96-well microplate at a density of 1x104 cells per well and incubated for 24 hours and proceeded with the treatment protocol mentioned above. The readings at 450 nm were averaged for each experimental condition, and the target protein modification was assessed by calculating the fold change as a ratio of the treated and non-pre-treated modified protein. The values were then presented as a percentage of EGFR and Phosphorylated EGFR.

2.5.3 MAPK

Endogenous levels of MAPK were evaluated using the PathScan®MAP Kinase Multi-Target Kit (Cell Signalling Technologies, Massachusetts, USA), which detects six different target proteins per the manufacturer's protocols. The experiment was carried out in duplicate. The magnitude of absorbance is proportional to the number of bound target proteins. Each protein released was compared to the untreated group and converted to a percentage.

2.5.4 AP-1

After the treatment and irradiation period, DNA from the desired cells was extracted using the Genomic DNA Mini Kit (Geneaid Biotech Ltd, Taiwan). The amount of DNA was standardised to 0.6 µg/µL using the Nuclear Extract Dilution Buffer. The AP-1 levels were determined using the TF ELISA target-specific kit (Panomics, USA) per the manufacturer's protocols. The absorbance was read at 450 nm and converted to a percentage based on the comparison with the blank and positive reading (supplied in the kit) for each sample.

2.5.5 MMPs

The extracellular release of MMP 1, 3 and 9 were determined using the Human MMP-1, 3, 9 enzyme-linked immunosorbent assay (ELISA) kit (RayBio®, Inc, Norcross, Georgia, USA). The amount of MMPs was determined in each sample by using the linear interpolation equation from the standard curve that was generated based on the standard control given in the kit.

2.5.6 Statistical analysis

Data were analysed using one-way ANOVA followed by Bonferroni post hoc multiple comparisons using SPSS Version 18. A p value <0.05 between the control and test groups was considered significant. Data presented as the mean of triplicate of each group ± SD (n=3).

3. Results

3.1 SOD and CAT

The control cells inhibited superoxide anion the highest (65.79%), showing functional SOD activity. Carrageenan and vit-E pre-treated but nonirradiated cells showed moderate inhibition of superoxide anions. Cells exposed to UVB without treatment had a weaker ability to inhibit superoxide anion, with only 20.77% inhibition after 100 mJ/cm², which reduced to 13.94% after 300 mJ/cm². In contrast, pre-treated groups significantly elevated inhibition against superoxide anions by 32.51-44.47% after 100 mJ/cm² UVB, the highest being κ and vit-E combination (65.24%). At 300 mJ/cm², cells treated with κ showed the highest percentage (61.42%) of superoxide anion inhibition. The combination treatment showed better SOD activity compared to vit-E alone but not against carrageenan by itself (Figure 1).

Catalase in control cells was the highest, 78.63 Units/ml (U/ml). Non-pre-treated cells had 14.95 U/ml CAT after 100 mJ/cm², which decreased by almost half after 300 mJ/cm². However, pre-treated cells showed significantly

higher (p < 0.05) CAT. After 100 mJ/cm² and 300 mJ/cm², the highest CAT was in cells treated with κ, 48.53 U/ml, 68.39 U/ml, respectively and combination treatment induced higher CAT compared to vit-E alone. (Figure 2).
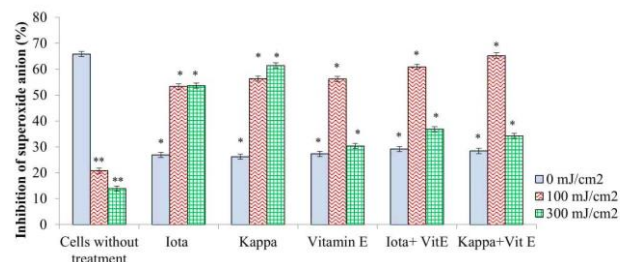
Figure 1. Percentage of superoxide anion inhibition. *Significant difference between non-pre-treated irradiated cells at p<0.05 with pre-treated irradiated groups. **Significant difference between non-pre-treated irradiated cells at p<0.05 with non-pre-treated and nonirradiated cells.
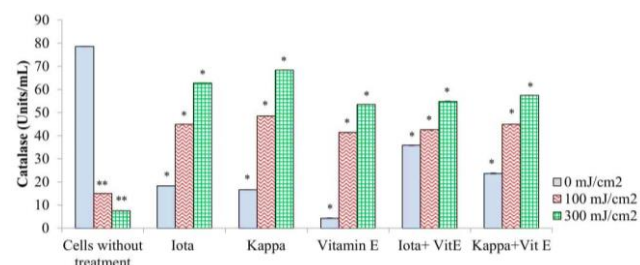
Figure 2. Catalase production. *Significant difference between non-pre-treated irradiated cells at p<0.05 with pre-treated irradiated groups. **Significant difference between non-pre-treated irradiated cells at p<0.05 with non-pre-treated and nonirradiated cells.

3.2 EGFR and Phosphorylated EGFR

The level of both EGFR and its activated form (phospho-EGFR) in control cells was taken as 100% as the starting point. A reduction in EGFR was found in cells treated with carrageenans and vit-E without irradiation (Figure 3a), with a 3.00-4.00% increase in phospho-EGFR level (Figure 3b).

After 100 mJ/cm² UVB, the EGFR level in all irradiated groups increased by 31.00% compared to the control cells. However, the increase in pre-treated groups was only 1.00-12.00%, indicating the treatment was able to suppress EGFR. The phospho-EGFR in non-pre-treated cells was higher than the treated groups. After 300 mJ/cm² significantly (p < 0.05) higher level of EGFR was observed, with a 150% increase compared to the control cells and phospho-EGFR with a 226% increase in cells without treatment.
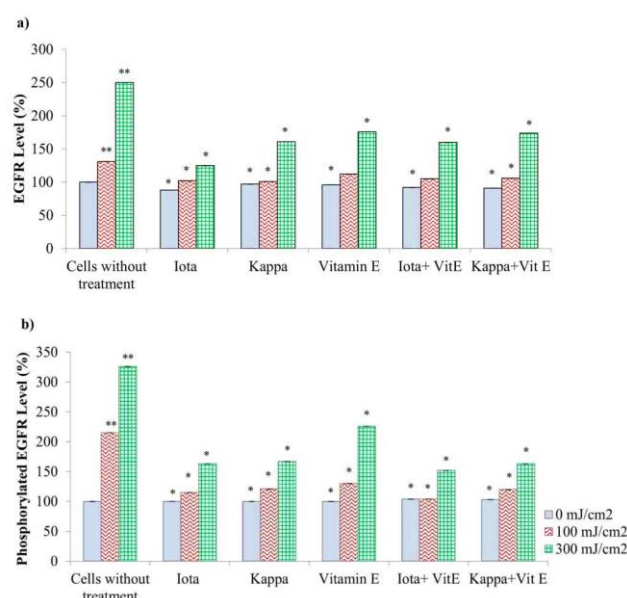
Figure 3. Levels of a) EGFR and b) Phospho-EGFR. * Significant difference between non-pre-treated irradiated cells at p<0.05 with pre-treated irradiated groups. **Significant difference between non-pre-treated irradiated cells at p<0.05 with non-pre-treated and nonirradiated cells.

3.3 MAP kinase

Activated EGFRs lead to an increase in MAP kinase signalling. In this study, six target proteins, namely the Phospho-p44/42 MAPK (Thr202/Tyr204), Phospho-p38 MAPK (Thr180/Tyr182), MEK1, Phospho-MEK1/2 (Ser217/221), SAPK/JNK and Phospho-SAPK/JNK(Thr183/Tyr185) were evaluated to determine the overall MAPkinase action (Table 1).

In comparison to the control cells, protein concentrations of the lysates in cells treated with carrageenans and/or vit-E without UVB irradiation showed either a decrease or increase in the release of Phospho-p44/42 MAPK (Thr202 /Tyr204), Phospho-p38 MAPK (Thr180/Tyr182), MEK1 and SAPK / JNK. After UVB, all six protein lysates increased in a fluence-dependent manner in comparison to the control. The most pronounced increase was Phospho-p44/42 MAPK (Thr202/Tyr204), which increased by 183.33% and 289.58% after 100 mJ/cm² and 300 mJ/cm², respectively. Carrageenans and/or vit E pre-treated cells showed a lower percentage of MAPK proteins after UVB irradiation compared to the untreated cells.

Protein concentrates in the pre-treated cells compared to the control ranged from 16.67-139.58% for Phospho-p44/42 MAPK (Thr202/ Tyr204), 7.58-48.48% for Phospho-p38 MAPK (Thr180/Tyr182) and 12.50-143.75% for MEK1. In cells irradiated with 300 mJ/cm2, treatment of carrageenans and/or vit-E suppressed the release of Phospho-MEK1/2 (Ser217/221) and SAPK/JNK compared to the control.

MAPK Proteins	UVB Fluence (mJ/cm^2)	Cells without treatment	Iota	Kappa	Vit E	Iota +Vit E	Kappa +VitE
Phospho-p44/42 MAPK(Thr202/Tyr204)	0	0±0.00	2.08±0.04*	12.5±0.08*	-10.42±0.13*	6.25±0.25*	-2.08±0.18*
	100	183.33±0.06**	85.42±0.08*	118.75±0.08*	100±0.11*	116.67±0.07*	139.58±0.09*
	300	289.58±0.05**	43.7±0.05*	27.08±0.09*	87.5±0.10*	102.08±0.14*	16.67±0.05*
Phospho-p38 MAPK (Thr180/Tyr182)	0	0±0.00	-3.03±0.09*	7.58±0.11*	0±0.10*	-16.67±0.05*	-24.24±0.07*
	100	69.7±0.09**	25.76±0.05	36.36±0.09	40.91±0.12*	27.27±0.07*	45.45±0.10*
	300	183.33±0.08**	36.36±0.11*	31.82±0.13*	48.48±0.18*	56.06±0.20*	7.58±0.04*
MEK1	0	0±0.00	-13.39±0.14*	10.71±0.08*	-7.14±0.16*	-8.93±0.17*	-14.29±0.17*
	100	144.64±0.09**	35.71±0.07	42.86±0.07*	143.75±0.12*	83.04±0.04*	118.75±0.14*
	300	158.04±0.07**	26.79±0.10	12.5±0.08*	29.46±0.18*	26.79±0.11*	14.39±0.09*
Phospho-MEK1/2 (Ser217/221)	0	0±0.00	43.24±0.16*	31.08±0.13*	37.84±0.08*	8.11±0.07*	31.08±0.13*
	100	135.14±0.07**	56.76±0.21	60.81±0.14*	127.03±0.07*	40.54±0.17*	167.57±0.13*
	300	235.14±0.06**	1.35±0.15	-39.19±0.20*	-10.81±0.34*	-33.78±0.03*	9.46±0.05*
SAPK/JNK	0	0±0.00	54.45±0.21*	20.45±0.14*	-36.36±0.16*	-54.55±0.12*	18.18±0.12*
	100	204.55±0.10**	72.72±0.21*	163.64±0.10	195.45±0.06*	179.55±0.10*	143.18±0.10*
	300	215.91±0.06**	-10±0.06*	-47.730.05*	6.38±0.25*	102.27±0.13*	-2.27±0.04*
Phospho-SAPK/JNK(Thr183/Tyr185)	0	0±0.00	-68.18±0.14*	-98.86±0.01*	-84.09±0.14*	-94.32±0.05*	-93.18±0.06*
	100	72.72±0.09**	-67.05±0.14*	-67.05±0.16*	-57.95±0.11*	-69.32±0.27*	-79.55±0.18*
	300	89.77±0.09**	-89.77±0.09*	-54.55±0.09*	-51.14±0.11*	-52.27±0.42*	-72.73±0.24*

TABLE 1. Percentage of MAPK proteins. *Significant difference between non-pre-treated irradiated cells at p<0.05 with pre-treated irradiated groups. **Significant difference between non-pre-treated irradiated cells at p<0.05 compared with non-pre-treated and nonirradiated cells.

3.4 Transcription factor (AP-1)

The control cells had 0.22% AP-1. An increase between 2.12-4.21% was seen in pre-treated cells without UVB. A UVB fluence-dependent pattern was observed in the percentage of AP-1 after 100 and 300 mJ/cm2 UVB in both treated and non-pre-treated groups, with the latter being the highest. In general, the protection against the formation of AP-1 in DNA was significantly observed after carrageenans treatment compared to nontreated cells. Although the combination group exhibited protection, it was not significantly (p>0.05) better than those treated with carrageenans alone. However, it exhibited a stronger protective effect compared to vit-E alone (Figure 4).
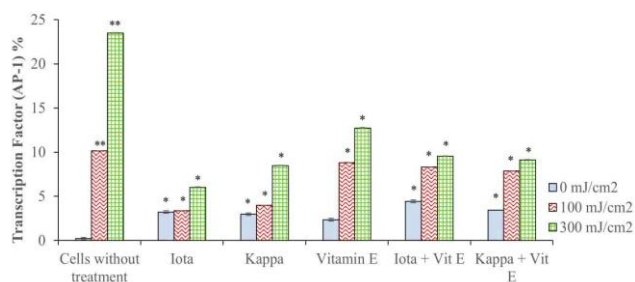
Figure 4. Percentage of transcription factor (AP-1) in 6 ug DNA. *Significant difference between non-pre-treated irradiated cells at p<0.05 with pre-treated irradiated groups. **Significant difference between non-pre-treated irradiated cells at p<0.05 with non-pre-treated and nonirradiated cells.

3.5 MMPs

The MMP-1 in nonirradiated cells increased significantly (p < 0.05) after pre-treatment with carrageenans and vit-E. After subjecting to UVB, the level of MMP-1 in non-pre-treated cells increased significantly but decreased significantly in pre-treated cells. The reduction in MMP-1 was more pronounced in cells treated with the combination of carrageenans and vit-E compared to vit-E alone (Figure 5a).

Extracellular quantification of MMP-3 in nonirradiated cells remained almost constant when treated with the test compounds without UVR irradiation. The highest increase (2.79 ng) was observed in the non-pre-treated cells after 300 mJ/cm² irradiation, followed by 100 mJ/cm² (1.56 ng). All pre-treated groups showed lower amounts of the MMP compared to those without treatment after irradiation with UVB. The lowest was the κ- pre-treated group (0.32 ng) after 100 mJ/cm² UVB (Figure 5b).

The levels of MMP-9 increased significantly in nonirradiated pre-treated cells compared to the control cells (1295.83 pg). Likewise, the levels increased after UVB irradiation, with the highest level in non-pre-treated groups after 100 and 300 mJ/cm², respectively (Figure 5c).
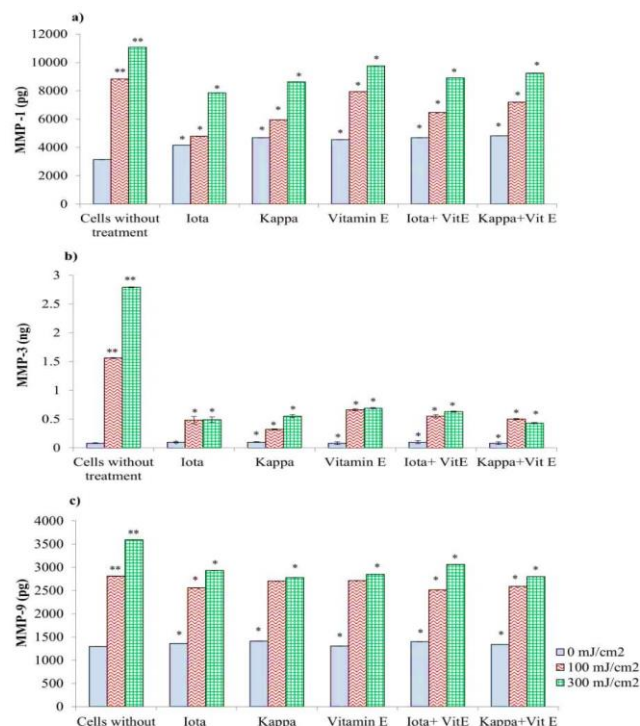
Figure 5. Level of a) MMP-1 b) MMP-3 c) MMP-9. *Significant difference between non-pre-treated irradiated cells at p<0.05 with pre-treated irradiated groups. **Significant difference between non-pre-treated irradiated cells at p<0.05 with non-pre-treated and nonirradiated cells.

4. Discussion

Superoxide dismutase and CAT protects human keratinocytes against UVB-induced cell damage (Rezvani et al.,2006), and a decrease in these enzymes causes excessive ROS damage. In this study, it was noticeable that the activity of SOD was higher in cells without irradiation than in those subjected to UVB, showing that normal cells spontaneously inhibit superoxide anions, but the tendency reduced after UVB.

Nevertheless, carrageenans enhanced SOD in irradiated cells by effectively removing superoxide anions after UVB compared to the non-pre-treated cells. A similar trend was observed with CAT. Sasaki et al., (1997) showed that SOD in HaCaT cells peaked following a single exposure to UVB, followed by a decline, which suggested the increase occurs as a cutaneous antioxidant defence against UVB. In the present study, higher inhibition of superoxide anion and CAT release was observed after exposure to 300 mJ/cm2 UVB compared to 100 mJ/cm2, which could be a defence mechanism against UVB, as postulated by Sasaki. The antioxidant defence in UVB irradiated cells was enhanced by carrageenans pre-treatment.

The same study mentioned that treatment with high calcium following UVB exposure in keratinocytes induced higher SOD activity and cell viability (Sasaki et al.,1997). This further explains the possibility of carrageenans in stimulating SOD and protecting cells since carrageenan has high calcium content along with sodium, potassium and magnesium (Cian et al.,2015). As reviewed by Pandel et al., (2013), natural photoprotection agent exhibits their effect as an antioxidant and their capacity to increase SOD, CAT, GPx and other antioxidant enzymes, which collectively provides anti-inflammatory, anti-carcinogenic and anti-ageing properties. Similarly, we postulate carrageenans can enhance SOD and CAT activities as part of the antioxidant defence against UVB, thus, providing an overall photoprotective effect.

An increase in EGFR happens within minutes after UVR in cultured keratinocytes and mouse skin (El-Abaseri et al.,2005). He et al., (1997) found that EGFR was inhibited in breast cancer cells treated with kappa-selenocarrageenan preventing cell proliferation. The findings were like the present study, where carrageenans were able to inhibit EGFR and phospho-EGFR, and is postulated to be due to carrageenans' potential antioxidant mechanism whereby once ROS is attenuated, the actions of receptor ligands that activate EGFR are blocked (Meves et al.,2001). In a study using green tea, it was said that the green tea polyphenols repealed the UVB-induced proinflammatory signalling by binding with EGFR and suppressing extracellular signalling, which inhibited cell proliferation and led to apoptosis (Bowden, 2004). There is a possibility that carrageenans could have bonded to the EGFR, thus, suppressing its activation. In contrast, the high levels of EGFR in non-pre-treated cells could have led to the activation of other signalling pathways.

Activation of EGFR leads to increased signalling of MAPK proteins and pathways. The present study showed an increase in all the six target proteins after UVB, especially in the non-pre-treated groups, which could be due to the phosphorylation of EGFR. Phosphorylation of protein kinases can be regulated by UVR-induced oxidative stress via MAPKs and AP-1 signalling pathways (Mantena & Katiyar,2006). Mutations or alterations in the proteins regulating MAPK signalling, such as EGFR overexpression, mutations of rat sarcoma (RAS), or rapidly accelerated fibrosarcoma (RAF), can cause changes in MAPK regulation (Ouwens,2001).

Ultraviolet radiation activates all three MAPKs (p38, JNK, ERK) in skin cells (Dent et al.,2003). The activity of p38 due to ionising radiation is variable, showing either no activation (Kim et al.,2002), weak activation (Taher et al.,2000) or strong activation (Narang et al.,2009), whereas activation of ERK (MEK1/2) and SAPK/JNK pathways has been observed in varied cell types, whether to low or high radiation (Munshi & Ramesh, 2013). UVB raised p38 and ERK phosphorylation

between two and ten hours after exposure. Although p38 activation was constant, a gradual increase was seen in the phosphorylation of ERK (Chen & Bowden, 1999). A similar pattern was observed in this study, where the highest was phospho-MEK1/2, phospho-SAPK/JNK, followed by phospho-p38 and phospho-p42/44. It is also proven that UVR, cytokines, DNA-damaging agents, and ROS strongly activate the SAPK/JNK pathway (Ouwens et al.,2001), as in this study. Moreover, ERK pathways are mostly associated with growth factor receptors, whereas activation of cytokine receptors regulates JNK and p38 pathways (Fisher et al.,1998); hence, in this study, it is surmised that the activation of ERK pathway is more likely compared to JNK and phospho-p38.

It was observed that UVB-induced JNK activation only lasted about an hour (Chen & Bowden,1999). Similarly, after 300 mJ/cm², SAPK/JNK activation was lower than phospho-p38 and phospho-p42/44. Hence, results suggest that SAPK/JNK activation could be reduced after 24 hours, in comparison to phospho-p38 and phospho-p44/42, which gradually increased proportionally to UVB fluence. Antioxidants attenuate the activation of MAPK signalling (Afaq & Mukhtar,2006); thus, this study suggests that MAPK suppression could be due to carrageenans being sulphated polysaccharides that act as antioxidants (Zhang et al.,2010).

Activation of AP-1 is directly related to phosphorylation of MAPK proteins, especially ERK and JNK (López-Camarillo et al.,2011), as observed in this study, especially in the non-pre-treated cells. A decrease of AP-1 in pre-treated groups could be due to the antioxidant capacity of carrageenans, which attenuated the MAPK proteins and failed to activate AP-1 in large quantities. AP-1 increases collagen breakdown and remains elevated within 24 hours after UVB exposure (Fisher et.al.,1996). Similarly, AP-1 remained elevated in non-pre-treated cells, but the reduction was observed in pre-treated groups.

Liebel et al., (2012) demonstrated that human epidermal keratinocytes generate a dose-dependent increase in proinflammatory cytokines and expression of MMPs after UVB, as seen in this study. Initiation of MMPs can be due to AP-1 activation (Berneburg et al.,2000). The potential antioxidant and immunomodulatory activities of carrageenans could have suppressed MMPs in treated cells, as supported by Sun et al., (2017), who showed that MMPs in keratinocytes could be prevented by antioxidant and immunomodulatory effects.

Studies proved that seaweeds or their extracts could inhibit MMPs (Chung et al.,2001; Kang J et al.,2008) due to their high phenolic content (Kim et al.,2006) by impeding the ERK pathways (Moon et al.,2008) or MMP-1 promoter (Moon et al.,2009). After UVA exposure, MMP-1 was directly stimulated in the dermal fibroblasts; however, MMP-1

release due to UVB required the presence of epidermis (Battie et al.,2014). Thus, it is appropriate to use keratinocytes in this study to assess the release of MMPs after UVB. The ability of carrageenans to induce SOD and CAT could have played a role in inhibiting MMPs.

Vitamin E protects cellular membranes and lipoproteins against oxidative damage by quenching singlet oxygen and superoxide anions (Agatonovic-Kustrin & Morton, 2013). It prevents the breakdown of collagen and reduces MMP-1; therefore, the use of α-tocopherol help protects the dermis from degrading, provided it is in high concentrations (Zussman et al.,2010). This corroborates with the present finding, which showed the lack of protection when keratinocytes were treated with vit-E at low concentrations. However, the combination of carrageenans and vit-E could provide stronger protection than vit-E alone.

5.   Conclusion

This study showed that carrageenans have a potential photoprotective effect against UVB in keratinocytes, possibly through the antioxidant and anti-inflammatory properties that attenuated ROS and inflammatory cytokines, potentially halting the activation of other mediators responsible for photoaging. The outcome of this research would highlight the prospective value of carrageenans in enhancing or promoting photoprotection and photocarcinogenesis against UVB. However, further studies would have to be conducted to uncover the best formulation.

6.   Acknowledgements

7.   References

Afaq, F., Mukhtar, H. (2006). Botanical antioxidants in the prevention of photocarcinogenesis and photoaging, Experimental dermatology 15(9): 678-684.

Agatonovic-Kustrin, S., Morton, D. (2013). Cosmeceuticals derived from bioactive substances found in marine algae.

Battie, C., Jitsukawa, S., Bernerd, F., Del Bino, S., Marionnet, C., Verschoore, M. (2014). New insights in photoaging, UVA induced damage and skin types, Experimental dermatology 23, 7-12.

Berneburg, M., Plettenberg, H., Krutmann, J. (2000) Photoaging of human skin, Photodermatology, Photoimmunology & Photomedicine: Review article 16(6): 239-244.

Bowden, G. T. (2004). Prevention of non-melanoma skin cancer by targeting ultraviolet-B-light signalling, Nature Reviews Cancer 4(1): 23-35.

Brenneisen, P., Sies, H., Scharffetter-Kochanek, K. A. R. I. N. (2002). Ultraviolet-B irradiation and matrix metalloproteinases: from induction via signaling to initial events, Annals of the New York Academy of Sciences 973(1): 31-43.

Campo, V. L., Kawano, D. F., da Silva Jr, D. B., Carvalho, I. (2009). Carrageenans: Biological properties, chemical modifications and structural analysis–A review, Carbohydrate polymers 77(2): 167-180.

Chen, W., Bowden, G. T. (1999). Activation of p38 MAP kinase and ERK are required for ultraviolet-B induced c-fos gene expression in human keratinocytes, Oncogene 18(52): 7469-7476.

Chung, J. H., Seo, J. Y., Choi, H. R., Lee, M. K., Youn, C. S., Rhie, G. E., Cho K.H., Kim K.H., Park K.C., Eun, H. C. (2001). Modulation of skin collagen metabolism in aged and photoaged human skin in vivo, Journal of Investigative Dermatology 117(5): 1218-1224.

Cian, R. E., Drago, S. R., De Medina, F. S., Martínez-Augustin, O. (2015). Proteins and carbohydrates from red seaweeds: evidence for beneficial effects on gut function and microbiota, Marine drugs 13(8): 5358-5383.

Davis, E. C., Callender, V. D. (2010). Postinflammatory hyperpigmentation: a review of the epidemiology, clinical features, and treatment options in skin of color, The Journal of clinical and aesthetic dermatology 3(7): 20.

Dent, P., Yacoub, A., Fisher, P. B., Hagan, M. P., Grant, S. (2003). MAPK pathways in radiation responses, Oncogene 22(37): 5885-5896.

El-Abaseri, T. B., Putta, S., Hansen, L. A. (2006). Ultraviolet irradiation induces keratinocyte proliferation and epidermal hyperplasia through the activation of the epidermal growth factor receptor, Carcinogenesis 27(2): 225-231.

Fisher, G. J., Datta, S. C., Talwar, H. S., Wang, Z. Q., Varani, J., Kang, S., Voorhees, J. J. (1996). Molecular basis of sun-induced premature skin ageing and retinoid antagonism, Nature, 379(6563): 335-339.

Fisher, G. J., Talwar, H. S., Lin, J., Lin, P., McPhillips, F., Wang, Z., Li X, Wan Y, Kang S, Voorhees, J. J. (1998). Retinoic acid

inhibits induction of c-Jun protein by ultraviolet radiation that occurs subsequent to activation of mitogen-activated protein kinase pathways in human skin in vivo, The Journal of clinical investigation 101(6): 1432-1440.

He, G., Cheng, C., Lu, R. (1997). Studies on biological effects of kappa-selenocarrageenan on human breast cancer cell line BCaP-37, Zhonghua yu Fang yi xue za zhi [Chinese Journal of Preventive Medicine] 31(2): 103-106.

Herouy, Y. A. R. E. D. (2001). Matrix metalloproteinases in skin pathology, International journal of molecular medicine 7(1): 3-15.

Hwang, K. A., Yi, B. R., & Choi, K. C. (2011). Molecular mechanisms and in vivo mouse models of skin aging associated with dermal matrix alterations, Laboratory animal research 27(1): 1-8.

Kalitnik, A. A., Barabanova, A. B., Nagorskaya, V. P., Reunov, A. V., Glazunov, V. P., Solov'eva, T. F., Yermak, I. M. (2013). Low molecular weight derivatives of different carrageenan types and their antiviral activity, Journal of applied phycology 25(1): 65-72.

Kang, J., Chen, W., Xia, J., Li, Y., Yang, B., Chen, B., Sun, W., Song, X., Xiang, W., Wang, X. Wang, F., Bi Z., Wan, Y. (2008). Extracellular matrix secreted by senescent fibroblasts induced by UVB promotes cell proliferation in HaCaT cells through PI3K/AKT and ERK signaling pathways. International journal of molecular medicine, 21(6): 777-784.

Kim, M. M., Van Ta, Q., Mendis, E., Rajapakse, N., Jung, W. K., Byun, H. G., Jeon Y.J., Kim, S. K. (2006). Phlorotannins in Ecklonia cava extract inhibit matrix metalloproteinase activity, Life Sciences 79(15): 1436-1443.

Kim, S. J., Ju, J. W., Oh, C. D., Yoon, Y. M., Song, W. K., Kim, J. H., Yoo, Y.J., Bang, O.S., Kang, S.S., Chun, J. S. (2002). ERK-1/2 and p38 kinase oppositely regulate nitric oxide-induced apoptosis of chondrocytes in association with p53, caspase-3, and differentiation status, Journal of Biological Chemistry 277(2): 1332-1339.

Liebel, F., Kaur, S., Ruvolo, E., Kollias, N., Southall, M. D. (2012). Irradiation of skin with visible light induces reactive oxygen species and matrix-degrading enzymes, Journal of Investigative Dermatology 132(7): 1901-1907.

Lin, F. H., Lin, J. Y., Gupta, R. D., Tournas, J. A., Burch, J. A., Selim, M. A., Monteiro-Riviere N.A., Grichnik J.M., Zielinski J., Pinnell, S. R. (2005). Ferulic acid stabilizes a solution of vitamins C and E and doubles its photoprotection of skin, Journal of Investigative Dermatology 125(4): 826-832.

López-Camarillo, C., Aréchaga Ocampo, E., López Casamichana, M., Pérez-Plasencia, C., Álvarez-Sánchez, E., & Marchat, L. A. (2012). Protein kinases and transcription factors activation in response to UV-radiation of skin: implications for carcinogenesis, International journal of molecular sciences 13(1): 142-172.

Mantena, S. K., Katiyar, S. K. (2006). Grape seed proanthocyanidins inhibit UV-radiation-induced oxidative stress and activation of MAPK and NF-κB signaling in human epidermal keratinocytes, Free Radical Biology and Medicine 40(9): 1603-1614.

Meves, A., Stock, S. N., Beyerle, A., Pittelkow, M. R., Peus, D. (2001). H2O2 mediates oxidative stress-induced epidermal growth factor receptor phosphorylation, Toxicology letters 122(3): 205-214.

Moon, H. J., Lee, S. H., Ku, M. J., Yu, B. C., Jeon, M. J., Jeong, S. H., Stonik V.A., Zvyagintseva T.N., Ermakova S.P., Lee, Y. H. (2009). Fucoidan inhibits UVB-induced MMP-1 promoter expression and down regulation of type I procollagen synthesis in human skin fibroblasts, European Journal of Dermatology 19(2): 129-134.

Moon, H. J., Lee, S. R., Shim, S. N., Jeong, S. H., Stonik, V. A., Rasskazov, V. A., Zvyagintseva, T., Lee, Y. H. (2008). Fucoidan inhibits UVB-induced MMP-1 expression in human skin fibroblasts, Biological and Pharmaceutical Bulletin 31(2): 284-289.

Munshi, A., Ramesh, R. (2013). Mitogen-activated protein kinases and their role in radiation response, Genes & cancer 4(9-10): 401-408.

Narang, H., Bhat, N., Gupta, S. K., Santra, S., Choudhary, R. K., Kailash, S., Krishna, M. (2009). Differential activation of mitogen-activated protein kinases following high and low LET radiation in murine macrophage cell line, Molecular and cellular biochemistry 324(1): 85-91.

Necas, J., Bartosikova, L. (2013). Carrageenan: a review, Veterinarni medicina 58(4).

Ouwens, D. M., de Mesquita, D. S. G., Dekker, J., & Maassen, J. A. (2001). Hyperosmotic stress activates the insulin receptor in CHO cells, Biochimica et Biophysica Acta (BBA)-Molecular Cell Research 1540(2): 97-106.

Pandel, R., Poljšak, B., Godic, A., Dahmane, R. (2013). Skin photoaging and the role of antioxidants in its prevention, International Scholarly Research Notices 2013.

Quan, T., Qin, Z., Xia, W., Shao, Y., Voorhees, J. J., Fisher, G. J. (2009, August). Matrix-degrading metalloproteinases in photoaging, In Journal of Investigative Dermatology Symposium Proceedings (Vol. 14, No. 1, pp. 20-24). Elsevier.

Rabe, J. H., Mamelak, A. J., McElgunn, P. J., Morison, W. L., Sauder, D. N. (2006) Photoaging: mechanisms and repair Journal of the American Academy of Dermatology 55(1): 1-19.

Ren, S. W., Li, J., Wang, W., & Guan, H. S. (2010). Protective effects of κ-ca3000+ CP against ultraviolet-induced damage in HaCaT and MEF cells, Journal of Photochemistry and Photobiology B: Biology 101(1): 22-30.

Rezvani, H. R., Mazurier, F., Cario-André, M., Pain, C., Ged, C., Taïeb, A., de Verneuil, H. (2006). Protective effects of catalase overexpression on UVB-induced apoptosis in normal human keratinocytes, Journal of Biological Chemistry 281(26): 17999-18007.

Sachs, D., Helfrich, Y., Voorhees, J. (2009). Molecular mechanisms in skin aging, COSMETIC DERMATOLOGY-CEDAR KNOLLS- 22(6): 291-298.

Saeed, A. K., & Salmo, N. (2012). Epidermal growth factor receptor expression in mice skin upon ultraviolet B exposure-Seborrheic Keratosis as a coincidental and unique finding, Advanced biomedical research, 1.

Sasaki, H., Akamatsu, H., Horio, T. (1997). Effects of a single exposure to UVB radiation on the activities and protein levels of copper-zinc and manganese superoxide dismutase in cultured human keratinocytes, Photochemistry and photobiology 65(4): 707-713.

Sokolova, E. V., Barabanova, A. O., Homenko, V. A., Solov'eva, T. F., Bogdanovich, R. N., Yermak, I. M. (2011). In vitro and ex vivo studies of antioxidant activity of carrageenans, sulfated polysaccharides from red algae. Bulletin of experimental biology and medicine 150(4): 426.

Sun, Z., Park, S. Y., Hwang, E., Zhang, M., Seo, S. A., Lin, P., Yi, T. H. (2017). Thymus vulgaris alleviates UVB irradiation induced skin damage via inhibition of MAPK/AP-1 and activation of Nrf2-ARE antioxidant system, Journal of cellular and molecular medicine 21(2): 336-348.

Taher, M. M., Hershey, C. M., Oakley, J. D., & Valerie, K. (2000). Role of the p38 and MEK-½/p42/44 MAP Kinase Pathways in the Differential Activation of Human Immunodeficiency Virus Gene Expression by Ultraviolet and Ionizing Radiation, Photochemistry and photobiology 71(4): 455-459.

Thevanayagam, H., Mohamed, S. M., Chu, W. L. (2014). Assessment of UVB-photoprotective and antioxidative activities of carrageenan in keratinocytes, Journal of applied phycology 26(4): 1813-1821.

Wen, K. C., Fan, P. C., Tsai, S. Y., Shih, I., Chiang, H. M. (2012). Ixora parviflora protects against UVB-induced photoaging by inhibiting the expression of MMPs, MAP kinases, and COX-2 and by promoting type I procollagen synthesis, Evidence-Based Complementary and Alternative Medicine, 2012.

Yasui, H., Sakurai, H. (2003). Age-dependent generation of reactive oxygen species in the skin of live hairless rats exposed to UVA light, Experimental dermatology 12(5): 655-661.

Yuan, H., Song, J., Zhang, W., Li, X., Li, N., Gao, X. (2006). Antioxidant activity and cytoprotective effect of κ-carrageenan oligosaccharides and their different derivatives, Bioorganic & Medicinal Chemistry Letters 16(5): 1329-1334.

Zhang, Z., Wang, F., Wang, X., Liu, X., Hou, Y., Zhang, Q. (2010). Extraction of the polysaccharides from five algae and their potential antioxidant activity in vitro, Carbohydrate Polymers 82(1): 118-121.

Zussman, J., Ahdout, J., Kim, J. (2010). Vitamins and photoaging: Do scientific data support their use?. Journal of the American Academy of Dermatology 63(3): 507-525.

A WAITING TIME-BASED BULLY ALGORITHM FOR LEADER NODE SELECTION IN DISTRIBUTED SYSTEMS

Md. Navid Bin Anwar[1a], Afroza Nahar[2a*], Nashid Kamal Md.[3a], Mehedi Hasan Shuvo[4a]

Abstract: In distributed systems, a single node (referred to as a leader) coordinates all other nodes to ensure synchronization. If this node fails, another node in the system must adopt the role of leader. The classic bully algorithm suffers from some significant drawbacks, such as excessive message passing, a redundant number of election calls, and uncertainties over message delivery. The enhanced bully algorithm is one of the most recent improvements of this algorithm. However, this algorithm performs poorly in average- and worst-case scenarios. In this paper, a novel waiting time-based algorithm is proposed to improve the enhanced bully algorithm for electing a new leader during such critical scenarios. In this algorithm, if a single or multiple number of nodes discover that the leader has failed, it does not broadcast instantly. Rather, it waits for a certain period, and this waiting time is assigned to the nodes according to their load. After the timeout, the node sends its message and starts the election process. Moreover, it restricts nodes from unnecessary message passing and stops any redundant election calls. Accordingly, this algorithm detects the failure of the leader node more precisely and elects a new leader more quickly.

Keywords: Distributed systems, bully election algorithm, electing coordinator, message passing

1. Introduction

A distributed system is an accretion of isolated computers that engage simultaneously through a system to accomplish a complex task that is coordinated by message passing (Beaulah et al., 2013; Sathesh, 2015). To arrange the various errands in a distributed system, a leader is essential for synchronizing the whole system whenever necessary. To select the leader (or leader), several algorithms have been proposed, including distinctive, ring topology, bully election, Franklin's, Chang and Robert's, time slice, and variable speeds (Amit & Animesh, 2016; Balmukund et al., 2014; Rahman & Nahar, 2009). However, all these algorithms have their own shortcomings, including time complexity, message passing, redundancy, and large network traffic. This paper presents a reformation of the enhanced version of the bully algorithm by introducing the time allocation concept to the nodes. The remainder of the paper is arranged as follows: Section 2 contains a brief literature review, Section 3 presents a description of the proposed algorithm with legitimate examples, Section 4 reports the comparative results and outcomes, and Section 5 indicates the inferences of the present study.

Authors information:

[a]Department of Computer Science, American International University – Bangladesh (AIUB), Dhaka 1229, BANGLADESH. E-mail: navid.anwar@aiub.edu[1]; afroza@aiub.edu[2]; nashidkamaljitu7@gmail.com[3]; shuvo.rpm@gmail.com[4]
*Corresponding Author: afroza@aiub.edu

2. Methodology

In this section, the four major algorithms for electing the leader node in distributed systems are discussed.

2.1 Bully Algorithm by Garcia-Molina

In 1982, Garcia-Molina first introduced the bully algorithm (Garcia, 1982), which dynamically chooses a coordinator (or leader) by utilizing the process identification (ID) number. This algorithm is based on the following essential hypotheses:

- It is a synchronous method that utilizes a timeout instrument to monitor leader disappointment location, and each process has an exceptional number to allow them to be recognized.

- Each node acknowledges the node ID among all other nodes. No node knows which forms are currently up and which forms are down.

- The node with the highest node ID is chosen as a leader and is in accord with other active nodes.

- A failed node can rejoin the process after recuperation.

Whenever the coordinator node is down, an election process for selecting a new leader starts, and the node with the highest ID becomes the new leader. All active nodes receive this message, which entails extensive message

passing and creates heavy network traffic (Garcia, 1982; Mamun et al., 2017).

From Figure 1, the leader election process can be described as follows:

   a)   As Node 2 detects that the leader node is down, it sends election messages to the higher Nodes 3 and 4.
   b)   In response, Nodes 3 and 4 send an OK message.
   c)   Nodes 3 and 4 send an election message to Node 5.
   d)   Node 4 sends an OK, although it will not receive any message from Node 5.
   e)   Node 4 will elect itself as leader and broadcast a leader message to each node in the network.

This algorithm has the following drawbacks:

   •   The most significant number of messages during the election is O (n2), regardless of how it is arranged. Whenever a node sees the leader node is down, another election is held. Subsequently, multiple elections could happen within this method at the same time, forcing substantial system traffic that could result in the system being overwhelmed.
   •   If the leader is running singularly or the connection between the process and the coordinator is damaged, some processes could fail to identify the leader and start an election, resulting in redundant elections.
   •   This algorithm does not guarantee message delivery. Consequently, multiple nodes could assign themselves as the leader simultaneously.

2.2   Modified Bully Algorithm by Quazi Ehsanul Kabir Mamun

The basic assumptions of this algorithm are rooted in the Bully algorithm, whereby the node with the highest ID number is selected as the leader (Mamun et al., 2017). However, this algorithm proposes a resolution in cases where any node (or multiple nodes) detects that the leader node does not respond.

   •   If any node identifies that the leader is unavailable or has not responded, an election is announced by sending a message to the nodes with higher IDs.
   •   In response, the node with the highest ID transmits an OK message and the node elects the node with the highest ID node after receiving the responses.
   •   After being elected, the highest node sends a leader message and broadcasts itself as the leader to all other existing nodes.

From Figure 2, the election process can be described as follows:

   a)   Node 2 detects that leader Node 5 is down.
   b)   An election message is then sent by Node 2 to the highest ID nodes (Nodes 3 and 4).
   c)   Upon receiving the election message, Nodes 3 and 4 send an OK message to Node 2.
   d)   Node 2 elects the highest ID node (i.e., Node 4), which then 4 broadcasts itself as the new leader to all other existing nodes.

Figure 1. Leader election in the bully algorithm.
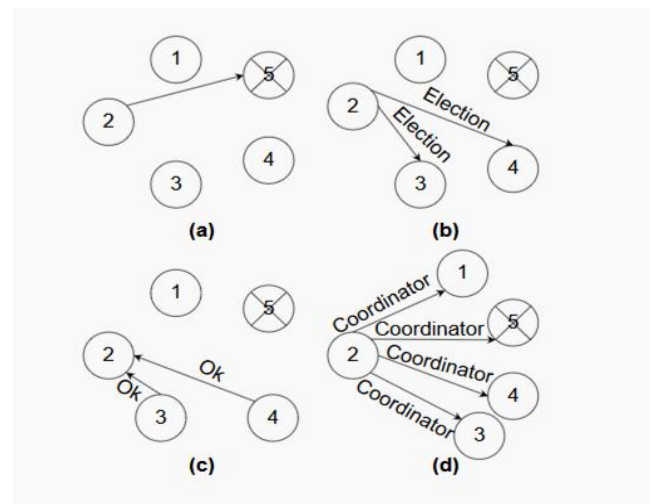
Figure 2. Leader election by Quazi Ehsanul Kabir Mamun (Mamun et al., 2017)

Although the modified bully algorithm reduces the total time of message passing and the complexity compared to the original bully algorithm, it displays some inadequacies:

- In some cases, the total number of messages passing increases because a node can receive more than one election message from its lower ID nodes, which increases network traffic.
- On recovery, the overall degree of message passing is also increased, causing a significant amount of network traffic.

2.3   Modified Bully Algorithm by Kordafshari et al.

Kordafshari et al. (2005) introduced a new algorithm in which the node containing the highest ID acts as the coordinator node. The author's also attempted to identify the ensuing circumstances if any node (or nodes) discovered that the leader node was down.

- When any node detects that the leader node is not responding, it instantaneously announces the start of an election and sends messages to all other existing nodes with higher IDs.
- In response, the higher ID nodes return an OK message, and the node selects the highest ID node among them after receiving the responses.
- After electing the highest node, it sends a GRANT message to the selected highest ID node.
- Upon receiving the GRANT message, the highest ID node then sends a new message to all other existing nodes as the new leader.
- If, after sending the message, the node does not receive either a response or an OK message from other existing nodes, it broadcasts itself as the new leader node and sends confirmation to all other active nodes.
- The algorithm will run again on recovery with the highest priority ID node.
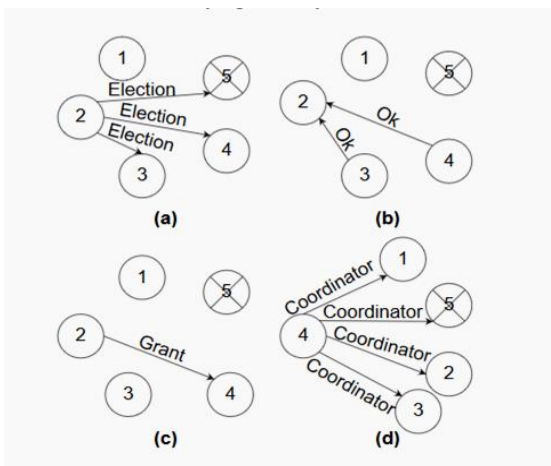
Figure 3. Leader Election by M.S. Kordafshari et al. (2005)

From Figure 3, the election process can be understood as follows:
a)   Node 2 detects that the leader node (Node 5) is down. Therefore, it initiates an election and sends an election message to Nodes 3, 4, and 5.
b)   An OK message is sent to all nodes as a response.
c)   Upon receiving the replies, Node 2 sends a GRANT message to Node 4, as it contains the highest node ID.
d)   When Node 4 receives the GRANT message, a leader message is broadcast to all other existing nodes.

This algorithm also suffers from the following deficiencies:

- If a node becomes down either while sending the election message or after receiving the priority number from higher ID nodes, the nodes will wait for a time of 3D for the leader message, where D is the average propagation delay. During this period, the nodes will recommence the algorithm if they do not receive any leader message, which is redundant (Kordafshari et al., 2005).
- The higher the number of nodes, the distinct precedent of the modified bully algorithm will remain at that moment in the system, which will cause repetitive election.
- The total amount of message passing, and network traffic will increase as a result of every redundant election.

2.3   Enhanced Bully Algorithm by Minhaj Khan, Neha Agarwal, and Jeeshan Ahmad Khan

This algorithm introduced the electing coordinator concept, which reduces the amount of unnecessary message passing and redundant election calls. When nodes detect that the coordinator has crashed, any of the following can happen:
- Only one node detects the crash.
- More than two nodes detect the crash.
- Every node detects that the leader is crashed.
- The node with the second-highest ID detects the crash.

This algorithm proposes that an election message should be sent by other nodes to the second-highest ID node. This node will then check whether the leader node is active. If the coordinator fails to respond again, then the second-highest ID node will elect itself as the new leader and send a notification to all other active nodes through a leader message (Minhaj et al., 2017). Three different variables are used to store the leader: the node ID, the ID of the leader that has crashed recently and the ID of the new leader (to reduce the total number of messages passing during the election).
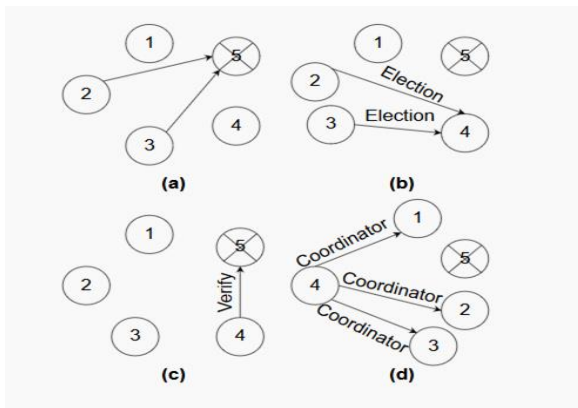
Figure 4. Leader election by Minhaj et al. (2017)

From Figure 4, the election process is clarified as follows:
a)   The leader node (Node 5) has crashed, which is detected by Nodes 2 and 3.
b)   Nodes 2 and 3 send an election message to the second higher node (Node 4).
c)   After receiving the election message, Node 4 checks whether the leader has crashed.
d)   When Node 4 detects that the leader node is down, it sends a message with the new leader ID and the recently crashed leader ID to all active nodes.

This algorithm has the following major drawbacks:
•   When all nodes (n) detect at a certain time that the leader has crashed, this results in the system having a total number of messages of $3 \times (n - 2) + 1$ and a time complexity of O (n).
•   If multiple nodes (n) detect that the leader is down, the number of messages passing for detecting the new leader will be $(2 \times x) + 1 + (n - 2)$ with a time complexity of O (n).

3.   Results and Discussions

In this section, a waiting time-based bully algorithm is introduced based on the enhanced bully algorithm (Kordafshari, 2005). According to the enhanced bully algorithm, a large number of messages pass when multiple nodes detect that the leader is down. Therefore, in order to reduce the number of messages passing and improve efficiency, a waiting time is introduced in the proposed algorithm. It implies that when a node notices that the leader is down, it does not instantly broadcast. The node instead waits for a certain amount of time before sending its message. Depending on their load, nodes are given a waiting time. If the load is small, then the waiting time will be shorter, or vice versa. Therefore, during average- or worst-case scenarios, when multiple (or all) nodes detect that the leader node is down or crashed, only the node with the smallest load (shortest waiting time) will send election message to the second-highest ID node. As the waiting time of this node will be the shortest, the timeout will occur first,

and the election process will begin soon. As explained previously, the second-highest process ID node will check the leader again by sending a message. If it also detects that the leader has failed, then it will declare itself the new leader by sending a leader message to all other active nodes. This process will prevent multiple nodes from sending election messages at the same time. Furthermore, it is very unlikely for multiple nodes to have the same waiting time, as this time depends on the load. Again, if the second-highest ID node is unavailable or is lost and cannot respond within the timeout, then the election requesting node will send the election request to the third highest process ID node. This process will continue after each timeout.

3.1   Algorithm

In the present algorithm, when N number of nodes detects that the leader node is down, the nodes respond according to their predefined waiting time. This waiting time is calculated and assigned to the nodes according to the following formula:

WaitingTime= propagation delay + verification time,
where the propagation delay describes the time, a packet takes to reach its destination from the source, the verification time defines the duration to check whether the leader is down or not, and w is a weight value defining the load on the node.

If there are five nodes in a distributed system and when the leader node is down, then the waiting time for the remaining four nodes can be assigned according to the following steps:

WaitingTime for Node 4 (highest process ID) = 0 ms (with minimal load)
WaitingTime for Node 3 (2nd highest process ID) = (2 × propagation delay + verification time)
WaitingTime for Node 2 (3rd highest process ID) = (2 × propagation delay + verification time) × 2
WaitingTime for Node 1 (3rd highest process ID) = (2 × propagation delay + verification time) × 3

After the waiting time has elapsed, the corresponding node sends an election message to the second-highest process ID node, after which the second-highest node checks the leader's status. If the leader node is down, it will broadcast a leader message to all active nodes, and the remaining nodes will not send any election messages; otherwise, it will discard the election message.

41

1. Initially the coordinator will assign the WaitingTime to each of the node according to the proposed algorithm.
   // Node X_1, X_2 ...... X_n detect that the coordinator is down
2. A single node, having smallest WaitingTime, will send election message to the second highest process ID node, when waiting time is finished.
3. Second highest process ID node will CheckNode (scp_id is down or not)
4.   If (scp_id node down)
5.   scp_id = ncp_id
6.   Broadcast coordinator message (ncp_id, rcp_id)
7.   Cancel remaining node from sending election

Figure 5. Pseudo code for the scenario when all nodes detect that the coordinator node is down.

3.3 Example

The election process according to the proposed algorithm is shown in Figure. 6. The steps can be described as follows:

a) Leader/coordinator Node 5 is down.
b) Nodes 1, 2, and 3 detect leader failure at the same time.
c) Based on the waiting time span, Node 3 sends an election message to the second-highest process ID node (Node 4). In this case, Nodes 1 and 2 will not send an election message to Node 4, as their waiting time is greater.
d) Node 4 checks the coordinator again and finds that the leader is down.
e) Finally, Node 4 sends a leader message to all active nodes and broadcasts itself as the new leader node. Upon receiving the message, all other nodes (active) update their table and store Node 4 as the new leader.

According to the average- and worst-case scenarios of the enhanced bully algorithm (Kordafshari, 2005), when multiple nodes (p) or all nodes (n) detect leader failure, the total number of messages passing will be $2 \times p + 1 + (n - 2)$ and $3 \times (n - 2) + 1$ (Kordafshari, 2005). However, in the proposed algorithm, when a multiple number (p) of nodes or all nodes (n) detect that the leader has failed, then the total number of messages passing between the nodes for electing the leader will be $2 \times (n - 2) + p + 1$ and $2 \times (n - 2) + 1 + 1$. However, the total number of messages passing within the nodes for electing the leader could be $3 \times (n - 2) + 1$, which is similar to Kordafshari (2005) when a timeout occurs for every election requesting node. It is very unlikely that this would happen in normal conditions and could only occur if the receiver (second-highest process ID node) was also down.
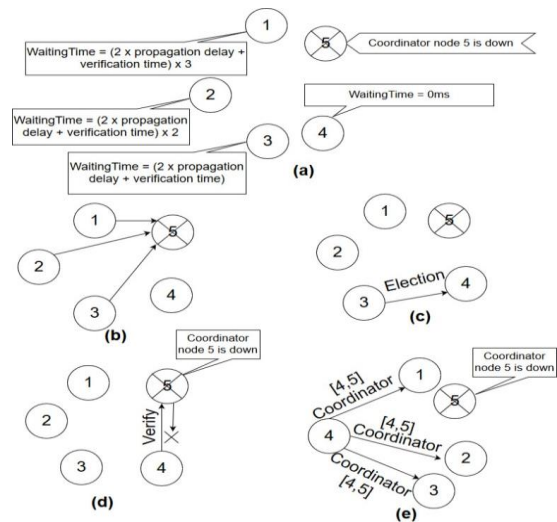
Figure 6. Steps to select a new leader node when multiple numbers of nodes find leader as down.

4. Comparison with Previous Algorithms

The performance of the proposed algorithm is compared with the bully algorithm, modified bully algorithm, and enhanced bully algorithm by counting the total number of messages passing during the scenario when multiple numbers of nodes detect the leader node is down. Table 1 indicates that the proposed waiting time-based bully algorithm exchanges the least number of messages. Hence, it detects the leader node failure earlier and can call the election quickly compared to other schemes. As a result, the efficiency of the proposed algorithm is better than other algorithms. This is due to the fact that the proposed algorithm restricts the nodes by assigning WaitingTime to send unnecessary redundant messages for verifying the leader node's failure while only one node, with a higher processing ID, will do this task first.

A network's propagation delay and verification time depend on the system conFigureuration. For this experiment, the following system conFigureuration was used: Intel i5-4210U CPU @ 1.70GHz (4 CPUs) ~2.4 GHz, 4 GB RAM, Windows 10 OS, and the network conFigureuration was Wireless LAN IEEE 802.11b/g/n with 3 Mbps bandwidth. The average network response time was 107.7 ms.

Table 1. Performance comparison of proposed algorithm with other algorithms

Total nodes in a network	Leader node Election Algorithms (number of messages)			
	Bully Algorithm	Modified Bully Algorithm	Enhanced Bully Algorithm	Proposed Algorithm
5	24	14	10	8
10	99	29	25	18
25	624	74	70	48
100	9999	299	295	198
150	22499	449	445	298

5.   Conclusion

A novel waiting time-based bully algorithm to elect the leader node in a distributed system was proposed in this article. The algorithm solves the limitations of enhanced bully algorithms and improves the performance of the algorithm in terms of message passing. The waiting time method in the proposed algorithm restricted the nodes from unnecessary message passing, stopping redundant election calls. Therefore, the proposed algorithm helps to detect leader node failure more precisely and elect the new leader more swiftly.

6.   Acknowledgement

7.   References

Amit B., Animesh D. (2016). A Timer Based Leader Election Algorithm, IEEE Conference.

Balmukund M., Ninni S. & Ravideep S. (2014). Master-Slave Group Based Model For Co-Ordinator Selection, An Improvement of Bully Algorithm, International Conference on Parallel, Distributed and Grid Computing, Solan, 457-460,

Beaulah SP, Thriveni J, Venugopal, K., & Patnaik LM (2013). An improved leader election algorithm for distributed systems, International Journal of Next-Generation Networks (IJNGN). 5(1): 21-29.

Garcia-Molina H, (1982). Elections in distributed computing system. IEEE Transaction on Computer C-31:48-59.

Kordafshari MS, Gholipour M., Jahanshahi M. & Haghighat AT. (2005) Modified Bully Election Algorithm in Distributed Systems. WSEAS International Conference on Computers.

Kordafshari, MS. M. Gholipour, Jahanshahi M. & Haghighat AT. (2005). Two novel algorithms for electing coordinator in distributed systems based on bully algorithm, the fourth WSEAS International Conference on Software Engineering, Parallel and Distributed Systems.

Mamun QH, Masum SH & Mustfa MA. (2017). Modified bully algorithm for electing coordinator in distributed systems, in Proc. 3rd WSEAS International Conference on Software Engineering, Parallel and Distributed Systems :22-28.

Minhaj K., Neha Agarwal & Jeeshan AK. (2017). An Enhanced Bully Algorithm for Electing a Coordinator in Distributed Systems. International Journal on Recent and Innovation Trends in Computing and Communication 5(5): 1092-1097.

Rahman M. & Nahar A. (2009). Modified Bully Algorithm using Election Commission. MASAUM Journal of Computing 1(3): 439-446,

Sathesh BM. (2015). Optimized Bully Algorithm. International. Journal of Computer Application. 121(18): 0975 – 8887.

MORTALITY PREDICTION OF SURGICAL INTENSIVE CARE UNIT PATIENTS USING DEEP LEARNING-BASED SURVIVAL MODELS

Lintu M.K.[1a], S. N. S. Acharya[2b*], Asha Kamath[3a], and David Raj Micheal[4c]

Abstract: Mortality prediction in surgical intensive care units (SICUs) is considered to be among the most critical steps in enforcing efficient treatment policies. This study aims to evaluate the performance of various deep learning models in predicting the mortality of patients admitted to SICUs. The survival of 2,225 adult patients admitted to SICUs was modeled using five salient deep learning-based survival models, namely, Cox-CC, Cox-Time, DeepSurv, DeepHit, and N-MTLR. The data were extracted from the Medical Information Mart for Intensive Care II (MIMIC-II) database. The performance of the models was compared using the time-dependent concordance index (C^{td}-index) and integrated Brier score (IBS). From among the five models, DeepSurv achieved the most accurate prediction, while Cox-Time demonstrated the least optimal predictive ability. For DeepSurv, Cox-CC, DeepHit, N-MTLR, and Cox-Time, the mean C^{td}-index was 0.773, 0.767, 0.765, 0.732, and 0.659, and the mean IBS was 0.181, 0.192, 0.195, 0.212, and 0.225, respectively. DeepSurv, Cox-CC, and DeepHit yielded comparable performance. Deep learning models are free from the stringent assumptions inherent in standard survival models. Hence, these models are considered flexible alternatives to the standard approaches in scalable, real-world survival problems.

Keywords: SICU, deep learning, survival analysis, mortality prediction, MIMIC-II

1. Introduction

The surgical intensive care unit (SICU) is a type of intensive care unit (ICU) for patients undergoing or recovering from surgery. Patients admitted to SICUs are typically in serious health condition, and often have a longer duration of stay, which has been associated with increased mortality rates. Accurately predicting in-hospital mortality and length of stay helps in implementing effective interventions and health care policies, as they are the most significant clinical outcomes for an ICU admission (Hartl et al., 2007; Mosissa et al., 2021).

The Cox proportional hazards (Cox-PH) model has been a salient choice for time-to-event analyses (Wang et al., 2019). However, the underlying linearity and proportional hazards assumptions of this particular model are relatively stringent for scalable, real-world datasets. Deep learning models, free from these assumptions, are emerging as efficient alternatives for the Cox-PH model. These models also have high prediction accuracies that directly assist clinicians in improving treatment plans (Sargent, 2001; Wang et al., 2019; Xiang et al., 2000).

This study applies some of the recently-developed and salient deep learning-based survival models to predict the overall survival of adult patients admitted to SICUs at the Beth Israel Deaconess Medical Center in Boston. The predictive performance of the models was compared using standard performance metrics.

2. Methods

This study involved a secondary data analysis of 2,225 adult patients admitted to SICUs from the MIMIC-II database (Goldberger et al., 2000). The MIMIC database offers the opportunity to develop and validate novel methods for critically ill patients. This database comprises anonymous health-related data of adult patients admitted to critical care units. Every patient is associated with physiological parameters such as cholesterol level, heart rate, serum glucose, O_2 saturation, etc., as well as general descriptors such as gender, age, height, and weight.

The continuous variables were summarized with a mean (SD) or median (Q_1, Q_3) based on the normality of variables, and the categorical variables were summarized with a frequency (%) value.

Authors information:

[a]Department of Data Science, Prasanna School of Public Health, Manipal Academy of Higher Education, Manipal, Karnataka, INDIA. E-mail: lintu.mk@learner.manipal.edu[1]; asha.kamath@manipal.edu[3]

[b]Manipal School of Information Sciences, Manipal Academy of Higher Education, Manipal, Karnataka, INDIA. E-mail: sudarsan.acharya@manipal.edu[2]

[c]Division of Mathematics, School of Advanced Sciences, Vellore Institute of Technology, Chennai, Tamil Nadu, INDIA. E-mail: davidraj.micheal@vit.ac.in[4]

*Corresponding Author: sudarsan.acharya@manipal.edu

The Kaplan-Meier method was used to visualize the overall survival, and to estimate the mean survival time of patients admitted to SICUs.

For time-to-event analyses of large datasets with several covariates, the standard Cox-PH model often fails, as it was designed for datasets with a relatively smaller number of covariates. Additionally, the Cox-PH model is too simplistic for real-world settings, as it assumes a linear relationship between the outcome and the covariates (Xiang et al., 2000). The proportional hazards assumption is another limitation of the Cox-PH model. According to prior work, it is evident that deep learning models provide more accurate results than standard models such as Cox-PH, without making stringent assumptions. Deep learning models also capture complex interactions between the dependent and independent variables involved, without any distributional assumptions (Sargent, 2001; Wang et al., 2019; Xiang et al., 2000). Hence, deep learning models emerge as efficient alternatives for the Cox-PH model in solving large real-world survival problems.

The five deep learning models employed to predict the survival of SICU patients were: DeepSurv (Katzman et al., 2018), DeepHit (Lee et al., 2018), Cox-CC, Cox-Time (Kvamme et al., 2019), and Neural Multi-Task Logistic Regression (N-MTLR) (Yu et al., 2011). DeepSurv and Cox-CC are non-linear extensions of the Cox model. Cox-Time, DeepHit, and N-MTLR are non-linear and non-proportional extensions of the Cox model. Additionally, DeepHit is able to handle competing risks. Unlike the other models, N-MTLR performs survival analysis through a series of logistic regression models. The neural network-based Cox-PH model based on the linear Cox-PH technique was also fit. All the models were fit using the pycox Python package (Kvamme et al., 2019).

Baseline variables with more than 50% missingness were dropped from the study. Subsequently, the models were built on the 29 baseline variables. The remaining missing observations were imputed using the fancyimpute Python package by employing an iterative imputation method where each feature with missing values is modeled as a function of other features in a round-robin fashion (Rafsunjani et al., 2019).

All of the continuous covariates were standardized, and the categorical variables were binary encoded prior to training the neural network. A five-fold cross-validation was applied with 60% training, 20% validation, and 20% testing sets. For all of the models, we applied the same network architecture used by Kvamme et al (2019), including ReLU activations (Nair & Hinton, 2010), batch normalization (Ioffe & Szegedy, 2015), dropout (Srivastava et al., 2014), and early stopping (Prechelt, 1998). Hyperparameter tuning was performed using a random grid search, and the optimal model was selected based on the scores obtained on the validation set.

The predictive performance of the models was then compared using a time-dependent concordance index (C^{td}-index) (Antolini et al., 2005) and an integrated Brier score (IBS) (Graf et al., 1999). Both measures range between zero and one. The highest C^{td}-index and lowest IBS indicate the best performance. The mean (95% CI) C^{td}-index and IBS were computed from a 5-fold cross-validation procedure.

3. Results

From among the 2,225 patients admitted to SICUs, 331 (14.88%) died in an SICU. The remaining 1,894 (85.12%) patients were considered censored. The median (Q_1, Q_3) duration of stay was 12 (7, 20) days. There were 955 (42.92%) female patients and 1,270 (57.10%) male patients. The mean (SD) age was 60.84 (19.18) years. The baseline characteristics of the two groups (patients who died and survived in SICUs) are described individually in Table 1.

Table 1. Baseline Characteristics.

	Total SICU patients (n = 2225)	Patients died in SICU (n = 331)	Patients survived in SICU (n = 1894)
Age in years (SD)	60.84 (19.18)	71.22 (16.73)	59.03 (19.01)
Height in cm (SD)	171.13 (13.98)	169.40 (11.88)	171.42 (14.02)
Weight in kg (SD)	81.16 (23.02)	80.49 (22.90)	83.25 (23.86)
HR in bpm (SD)	87.72 (19.85)	88.60 (21.85)	89.43 (20.33)
MAP in mmHg (SD)	87.01 (25.90)	86.71 (32.22)	86.14 (23.78)
RR in cpm (SD)	19.26 (6.96)	22.40 (6.88)	19.93 (5.35)
Na in mmol/l (SD)	139.34 (4.11)	139.55 (4.64)	139.31 (4.02)
K in mmol/l (SD)	4.05 (0.65)	4.01 (0.65)	4.06 (0.65)
HCO_3 in mmol/l (SD)	23.25 (4.19)	22.29 (4.59)	23.43 (4.09)
WBC in 103/mm3 (SD)	12.53 (6.09)	12.41 (5.89)	12.41 (5.89)
DiasABP in mmHg (SD)	64.20 (14.92)	62.29 (16.46)	63.84 (14.35)
Glucose in mg/dL(SD)	150.69 (63.42)	163.80 (75.29)	151.22 (59.89)

NIDiasABP in mmHg (SD)	62.30 (16.79)	61.02 (17.84)	62.52 (16.60)
NISysABP in mmHg (SD)	127.97 (26.66)	129.63 (32.05)	127.68 (25.62)
NIMAP in mmHg (SD)	82.78 (17.69)	82.70 (19.69)	82.79 (17.33)
Percentage of SaO_2(SD)	96.93 (3.02)	96.20 (1.64)	96 (4.31)
Temperature in °C (SD)	36.65 (1.07)	36.38 (0.63)	36.74 (0.84)
Cholesterol in mg/dL (SD)	160.54 (49.64)	163.38 (58.66)	159.89 (47.59)
FiO_2 (SD)	0.72 (0.25)	0.76 (0.25)	0.71 (0.25)
Mg in mmol/L (SD)	1.79 (0.39)	1.85 (0.37)	1.79 (0.39)
$PaCO_2$ in mmHg (SD)	40.77 (8.99)	38.53 (8.67)	41.24 (8.99)
PaO_2 in mmHg (SD)	188.46 (19.38)	205 (113.35)	184.89 (108.23)
Platelets in cells/nL (SD)	221.01 (100.50)	206.10 (99.75)	223.61 (100.43)
SysABP in mmHg (SD)	132.34 (29.59)	134.63 (35.37)	131.89 (28.30)
pH (SD)	7.37 (0.89)	7.38 (0.10)	7.37 (0.09)
Bilirubin in mg/dl (Q_1,Q_3)	0.80 (0.50, 1.80)	1 (0.50, 2)	0.80 (0.50, 1.70)
Hospital LOS in days (Q_1,Q_3)	12 (7, 20)	9 (5, 17)	13 (8, 21)
BUN in mg/dL(Q_1,Q_3)	17 (13, 27)	22 (14, 37)	16 (12, 25)
Creatinine in mg/dL(Q_1,Q_3)	0.90 (0.70, 1.30)	1.10 (0.80, 1.70)	0.90 (0.70, 1.20)
Lactate in mmol/L (Q_1,Q_3)	2.20 (1.40, 3.70)	2.80 (1.70, 4.20)	2 (3.60, 1.30)
Gender – male (%)	1270 (57.10)	183 (14.41)	1087 (85.59)

Continuous variables are presented as mean (SD), median (Q_1, Q_3); categorical variables are presented as frequency (%)

The survival probability was visualized as a function of time using the Kaplan-Meier method, as shown in Figure 1. The mean (95% CI) survival time of the patients admitted to SICUs was 95.09 (83.36, 106.83) days.
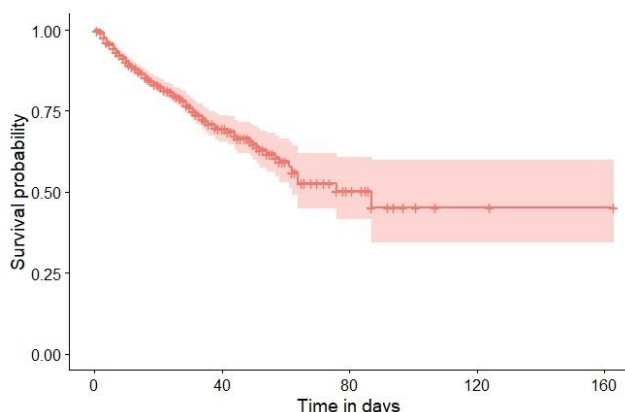
Figure 1. Survival probability of patients admitted to SICU.

The mean (95% CI) of the Ctd-index and IBS from a 5-fold cross-validation procedure for the different models are listed in Table 2.

Table 2. Performance of Deep Learning Models in Terms of C^{td}-index and IBS.

Model	C^{td}-index (95% CI)	IBS (95% CI)
Cox-CC	0.767 (0.737,0.798)	0.192 (0.106,0.279)
Cox-Time	0.659 (0.611,0.707)	0.225 (0.173,0.278)
DeepSurv	0.773 (0.743,0.803)	0.181 (0.139,0.222)
DeepHit	0.765 (0.727,0.804)	0.195 (0.181,0.208)
N-MTLR	0.732 (0.706,0.757)	0.212 (0.174,0.251)
Cox-PH	0.673 (0.631,0.717)	0.220 (0.173,0.277)

Among the five models, DeepSurv achieved the most optimal predictive performance based on both performance metrics; its mean C^{td}-index was 0.773 (95% CI: 0.743-0.803), and its mean integrated Brier score was 0.181 (95% CI: 0.139-0.222). Compared to all of the other models, Cox-Time obtained the least performance (Ctd-index 0.659, 95% CI 0.611, 0.707; Brier score 0.225, 95% CI 0.173, 0.278). The performance of both Cox-CC and DeepHit was similar to that of DeepSurv. For all of the models, both performance metrics resulted in similar results.

4.   Discussion

This study utilized the data extracted from the MIMIC-II database to evaluate the performance of various deep learning-based models to predict the survival of patients admitted to SICUs. This involved identifying a suitable algorithm to bring awareness about potential alternatives to the traditional Cox-PH model. Using such promising alternatives, clinicians could make use of the readily-available large-scale and complex real-world datasets to enforce enhanced treatment policies (Sargent, 2001; Wang et al., 2019; Xiang et al., 2000). The improved predictive ability of such models has already been proven in the existing literature (Katzman et al., 2018; Kvamme et al., 2019; Lee et al., 2018; Yu et al., 2011), in the context of large-scale healthcare record databases.

The results suggest that the DeepSurv model predicts the survival of SICU patients better than the other models. As predicting in-hospital mortality rates and quantifying patient health are vital in critical care research, using an appropriate model for a given dataset has a great impact (Austin et al., 2002; Jalali et al., 2020; Yun et al., 2021).

The limitations of his study include the use of secondary data and the large proportion of missing observations. To the best of our knowledge, this is the first study that attempts to evaluate the performance of various deep learning-based survival models to predict the survival of critically-ill patients admitted to SICUs. The large sample size and number of predictors in the SICU dataset from the MIMIC-II database further strengthens the conclusions of our study.

5.   Conclusions

The Standard Cox-PH model underperforms for large datasets, attributable to its restrictive model assumptions. Deep learning-based models that are free from such assumptions are excellent alternatives for the survival analysis of large real-world problems. Deep learning-based models are typically computationally-expensive, but with suitable tuning, their superior predictive performance can be leveraged for the accurate prediction of in-hospital mortality rates and in turn the effective management of ICU patients.

6.   Acknowledgements

7.   References

Antolini, L., Boracchi, P., & Biganzoli, E. (2005). A time-dependent discrimination index for survival data. Statistics in medicine 24: 3927-3944.

Austin, P. C., Rothwell, D. M., & Tu, J. V. (2002). A Comparison of Statistical Modeling Strategies for Analyzing Length of Stay after CABG Surgery. Health Services and Outcomes Research Methodology 3: 107-133.

Goldberger, A., Amaral, L., Glass, L., Hausdorff, J., Ivanov, P. C., Mark, R., ... & Stanley, H. E. (2000). PhysioBank, PhysioToolkit, and PhysioNet: Components of a new research resource for complex physiologic signals. Circulation [Online] 101, pp. e215–e220.

Graf, E., Schmoor, C., Sauerbrei, W., & Schumacher, M. (1999). Assessment and comparison of prognostic classification schemes for survival data. Statistics in medicine 18: 2529-2545.

Hartl, W. H., Wolf, H., Schneider, C. P., Küchenhoff, H., & Jauch, K. W. (2007). Acute and long-term survival in chronically critically ill surgical patients: a retrospective observational study. Critical Care 11: 1-11.

Ioffe, S., & Szegedy, C. (2015). Batch normalization: Accelerating deep network training by reducing internal covariate shift. In: International conference on machine learning, pp. 448-456.

Jalali, A., Lonsdale, H., Do, N., Peck, J., Gupta, M., Kutty, S., ... & Ahumada, L. M. (2020). Deep Learning for Improved Risk Prediction in Surgical Outcomes. Scientific Reports 10: 9289-9302.

Katzman, J. L., Shaham, U., Cloninger, A., Bates, J., Jiang, T., & Kluger, Y. (2018). DeepSurv: personalized treatment recommender system using a Cox proportional hazards deep neural network. BMC medical research methodology 18: 24-36.

Kvamme, H., Borgan, Ø., & Scheel, I. (2019). Time-to-event prediction with neural networks and Cox regression. Journal of Machine Learning Research 20: 1-30.

Lee, C., Zame, W. R., Yoon, J., & van der Schaar, M. (2018). Deephit: A deep learning approach to survival analysis with competing risks. In: Thirty-second AAAI conference on artificial intelligence.

Mosissa, D., Alemu, S., Rad, M. H., & Yesuf, E. A. (2021). Outcomes of Surgical Patients Admitted to the Intensive Care Unit of Jimma University Medical Center. Health Science Journal 15: 1-4.

Nair, V., & Hinton, G. E. (2010). Rectified linear units improve restricted boltzmann machines. In: 27th International Conference on Machine Learning: USA. Omnipress, pp. 807-814.

Prechelt, L. (1998). Early stopping-but when?. In: Neural Networks: Tricks of the trade, pp. 55-69. Springer, Berlin, Heidelberg.

Rafsunjani, S., Safa, R. S., Al Imran, A., Rahim, M. S., & Nandi, D. (2019). An empirical comparison of missing value imputation techniques on APS failure prediction. International Journal of Information Technology and Computer Science 2: 21-29.

Sargent, D. J. (2001). Comparison of artificial neural networks with other statistical approaches: results from medical data sets. Cancer: Interdisciplinary International Journal of the American Cancer Society 91: 1636-1642.

Srivastava, N., Hinton, G., Krizhevsky, A., Sutskever, I., & Salakhutdinov, R. (2014). Dropout: a simple way to prevent neural networks from overfitting. The journal of machine learning research 15: 1929-1958.

Wang, P., Li, Y., & Reddy, C. K. (2019). Machine learning for survival analysis: A survey. ACM Computing Surveys 51: 1-36.

Xiang, A., Lapuerta, P., Ryutov, A., Buckley, J., & Azen, S. (2000). Comparison of the performance of neural network methods and Cox regression for censored survival data. Computational statistics & data analysis 34: 243-257.

Yu, C. N., Greiner, R., Lin, H. C., & Baracos, V. (2011). Learning patient-specific cancer survival distributions as a sequence of dependent regressors. Advances in neural information processing systems 24: 1845–1853.

Yun, K., Oh, J., Hong, T. H., & Kim, E. Y. (2021). Prediction of Mortality in Surgical Intensive Care Unit Patients Using Machine Learning Algorithms. Frontiers in Medicine 8: 406-415

RELIABILITY ANALYSIS OF ACTIVE REDUNDANT SYSTEM USING GEOMETRIC DISTRIBUTION

Pankaj[1a], Jasdev Bhatti[2a*], Mohit Kumar Kakkar[3a]

Abstract: The present paper is an initiative taken towards study and analysis of industries concerning different maintenance strategies towards their products on behalf of their working and maintenance level. The objective of presenting the concept of the dual nature of repair for units having extra or major failures in addition to regular ones is well explained. The stochastic analysis of reliability characteristics using regenerative techniques for the system consisting of two parallel units following the active-standby redundancy and having different repair time distributions was also studied using geometric distribution. The numerical equations and results are being evaluated for reliability parameters like mean time to system failure, availability of the system in operative form, down period of the system following repair mechanism using regenerative techniques, and geometric distribution. The graphical analysis has also been presented for-profit function with respect to repair and failure rate.

Keywords: Reliability of systems, stochastic modeling, steady-state probability distribution, redundancy techniques, geometric distribution.

1. Introduction

Reliability is the probability that a particular system, service or product will seamlessly carry out its operation for a specific period with the maximum success rate. Moreover, with the astounding industrial development and a wide range of machines available globally, one significant factor that holds paramount importance is reliability. Manufacturing involves repair; therefore, critical evaluation of machines and system availability is essential to ensure the working capacity of the machines in all environmental conditions. Over the years, a significant effort has been put into evaluating the performance of industrial models. Researchers have suggested various reliability enhancement techniques such as redundancy, preventative maintenance, and priority to ameliorate system performance.

H. F. Martz et al. [18] have evaluated the reliability of a convoluted system comprising of several binomial series, or parallel subsystems. The components were estimated using a Bayesian approach. Also, E. Acar et al. [1] evaluated the influence of reliability allocation in different failure modes using system reliability-based design optimization (SRBDO) of an automobile for crashworthiness. In different situations of accidents, the relative importance of automotive structural elements was calculated. Y. S. Dai et al. [9] put forth a model for analyzing a grid's performance (service

time) and reliability in the context of common cause failures due to communication link sharing. Z. Tian et al. [25] and M. Du. et al. [10] described an optimization approach for multi-state series-parallel systems that improve redundancy at every step. M. Ram et al. [23] analyzed the reliability of a system consisting of one main unit and another standby unit. The standby system would be kept in working mode when the primary unit malfunctions. Considering mechanical systems G. Kumar et al. [14], M. Perman et al. [21] applied the Semi-Markov technique. With M operational functions, W warm standby units, and a single repair server with the restoration plan, W. L. Chen [8] evaluated the reliability of retrial machine system. D. Hua et al. [12,13] presented a significant research problem in terms of analyzing systems with linked unit degradation modes. Considering multi-state systems, different reliability measures were analyzed by Y. Liu et al. [17] and M. Nourelfath et al. [20]. S. H. Lee et al. [15] analyzed the behaviour of vehicle working systems. G. Levitin et al. [16] developed an algorithm for analyzing non-repairable series-parallel multi-state systems. A multi-domain simulation is presented by P. Adler et al. [2] to assess the aluminium electrolytic capacitors reliability. M. Y. Haggag [11] looked at the Mean Time to System Failure, steady-state availability, and cost of a two-dissimilar-unit cold standby system with regular inspection. With the assumption that each unit could operate in one of three states: normal, partial, or complete failure, the proposed system was investigated. To detect and reduce possible failure modes, a detailed design for the reliability model of vehicle systems

Authors information:

[a]Chitkara University Institute of Engineering and Technology, Punjab, 140401, INDIA.
Email: pankaj.khanna@chitkara.edu.in[1];
jasdev.bhatti@chitkara.edu.in[2];
mohit.kakkar@chitkara.edu.in3
*Corresponding Author: jasdev.bhatti@chitkara.edu.in

and subsystems was presented by P Popovic et al. [22] along with the failure mode and effects analysis approach.

A. Mihalache et al. [19] analyzed the reliability of a mechatronic system by using the Petri Nets model. P.V. Srihari et al. [24] designed an artificial neural network based on a fault detection system to improve reliability. J. Bhatti et al. [3,4,5,6,7] studied the industrial systems that use a single or multiple repair server to handle a variety of failures and services.

This paper consists of two parallel units arranged in active-standby redundancy mode. The proposed model possesses two categories, 'A' and 'B', which are initially in operative mode. The new technique of repairman having dual nature of inspecting the minor cause of failure and having the capability of repairing it is well explained for automobiles falling under the 'A' category. If there is any major fault or accident, the failed unit would be transferred from the first stage of repair/inspection to the second stage of repair, with additional cost and time. Additionally, the concept of inspection of the repairs of a major failure is also reflected in the maintenance policy, which helps increase customer satisfaction and product reliability after repair. However, machines reported for regular or standard services fall under the category 'B' and have only simple and fixed price repair time/cost. Thus, the concept introduced in the paper clearly shows the current repairing mechanism followed in the automobile industry. The whole process has been designed and explained with the help of the transition model, as shown in Figure 1.

Operative States:

$$S_0 = (A_0, B_0), S_1 = (A_{r1}, B_0), S_2 = (A_0, B_{r1}), S_4 = (A_{r2}, B_0)$$

Failed States:

$$S_3 = (A_{r1w}, B_{r1}), S_5 = (A_{r2}, B_{r1})$$
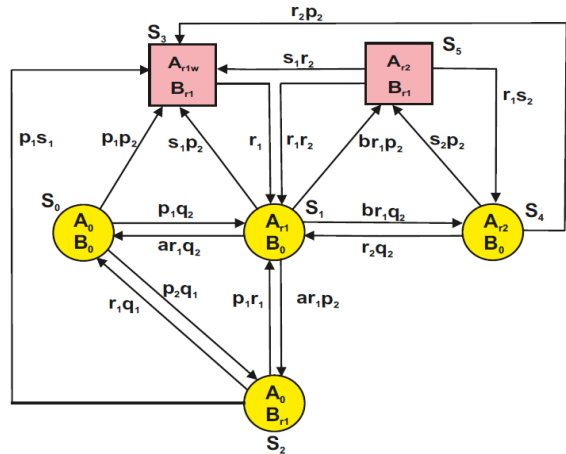
Figure 1. Transition Model

Table 1. Nomenclature

Symbol	Description
A_0, B_o	Units under categories A and B are in operational mode.
Ar_1	Inspection and minor repair of Unit A when it fails.
A_{r2}	Repair Unit A when it needs to be repaired in 1st inspection.
Br_1	Inspection and minor repair of Unit A when it fails.
A_{r1w}	Unit A waiting for its turn to get into the r_1 stage of inspection / repair.
P_1, P_2	Probability of unit A and B getting into a failed state
r_1	Inspecting and repairing probability of minor failure.
s_1	Failed to repair the failed Units due to major failure.
r_2	Repair rate of a major failure.
s_2	Failed or taking extra time to repair a major failure.
a	Probability of inspecting and repairing the minor failure.
b	Probability to inspect the nature of the major failure

2. Transition Probabilities and Sojourn Times

2.1 Transition Probabilities

The probabilities of steady-state transition from S_i to S_j is solved by:

$$P_{ij} = \lim_{t \to \infty} Q_{ij} \tag{1}$$

where Q_{ij} is the 'cumulative density function' from regenerative state $'i'$ to $'j'$. The calculated values of transition probability are listed:

$$P_{01}(t) = \frac{p_1 q_2}{1 - q_1 q_2} \quad P_{02}(t) = \frac{p_2 q_1}{1 - q_1 q_2} \quad P_{03}(t) = \frac{p_1 p_2}{1 - q_1 q_2} \quad P_{10}(t) = \frac{a r_1 q_2}{1 - s_1 q_2}$$

$$P_{12}(t) = \frac{a r_1 p_2}{1 - s_1 q_2} \quad P_{13}(t) = \frac{s_1 p_2}{1 - s_1 q_2} \quad P_{14}(t) = \frac{b r_1 q_2}{1 - s_1 q_2} \quad P_{15}(t) = \frac{b r_1 p_2}{1 - s_1 q_2}$$

$$P_{20}(t) = \frac{q_1 r_1}{1 - s_1 q_1} \quad P_{21}(t) = \frac{p_1 r_1}{1 - s_1 q_1} \quad P_{23}(t) = \frac{s_1 p_1}{1 - s_1 q_1} \quad P_{31}(t) = \frac{r_1}{1 - s_1}$$

$$P_{41}(t) = \frac{r_2 q_2}{1 - s_2 q_2} \quad P_{43}(t) = \frac{r_2 p_2}{1 - s_2 q_2} \quad P_{45}(t) = \frac{s_2 p_2}{1 - s_2 q_2} \quad P_{51}(t) = \frac{r_1 r_2}{1 - s_1 s_2}$$

$$P_{53}(t) = \frac{s_1 r_2}{1 - s_1 s_2} \qquad\qquad P_{54}(t) = \frac{r_1 s_2}{1 - s_1 s_2}$$

2.2 Mean Sojourn Times

The value of mean sojourn time for state Si is calculated by referring to sojourn time in state Si (i = 0 to 5) with the symbol μ :

$$\mu_0 = \frac{1}{1 - q_1 q_2} \qquad \mu_1 = \frac{1}{1 - s_1 q_2} \qquad \mu_2 = \frac{1}{1 - s_1 q_1} \qquad \mu_3 = \frac{1}{1 - s_1} \qquad \mu_4 = \frac{1}{1 - s_2 q_2} \qquad \mu_5 = \frac{1}{1 - s_1 s_2}$$

3. Mean Time to System Failure (MTSF)

Mean time to system failure (MTSF) is known to be a maintenance metric that measures the average amount of time a non-repairable unit or system operates before it fails.

The absorbing states depicted in Figure 1 are used to compute the proposed system's MTSF. The reliability analysis R_i at time $'t'$ is obtained is obtained by solving the equation 2-5.

$$Y_0 = Z_0 + q_{01} \copyright Y_1 + q_{02} \copyright Y_2$$
$$Y_1 = Z_1 + q_{10} \copyright Y_0 + q_{12} \copyright Y_2 + q_{14} \copyright Y_4$$
$$Y_2 = Z_2 + q_{20} \copyright Y_0 + q_{21} \copyright Y_1$$
$$Y_4 = Z_4 + q_{41} \copyright Y_1$$

$$(2\text{-}5)$$

Solving the above equations, we obtain

$$\text{MTSF} = \frac{N_1}{D_1}, \tag{6}$$

where,

$$N_1 = \mu_0 (1 - P_{12} P_{21} - P_{14} P_{41}) + \mu_1 (P_{01} + P_{02} P_{21}) + \mu_2 (P_{01} P_{12} + P_{02} - P_{02} P_{14} P_{41}) + \mu_4 (P_{01} P_{14} + P_{02} P_{14} P_{21}) \tag{7}$$

$$D_1 = (1 - P_{12} P_{21} - P_{14} P_{41}) - P_{10} (P_{01} + P_{02} P_{21}) - (P_{02} + P_{01} P_{12} - P_{02} P_{14} P_{41}) \tag{8}$$

4. System Availability/Operative Period Analysis

The availability of the considered system is the chance that a repairable system or system part is operational at a given moment and under a specific set of environmental circumstances.

If Γ_i denotes availability period of system at time $'t'$, then taking probabilistic argument, the derived relations will be as:

$$\Gamma_0 = Z_0 + q_{01}© \Gamma_1 + q_{02}© \Gamma_2 + q_{03}© \Gamma_3$$
$$\Gamma_1 = Z_1 + q_{10}© \Gamma_0 + q_{12}© \Gamma_2 + q_{13}© \Gamma_3 + q_{14}© \Gamma_4 + q_{15}© \Gamma_5$$
$$\Gamma_2 = Z_2 + q_{20}© \Gamma_0 + q_{21}© \Gamma_1 + q_{23}© \Gamma_3$$
$$\Gamma_3 = q_{31}© \Gamma_1$$
$$\Gamma_4 = Z_4 + q_{41}© \Gamma_1 + q_{43}© \Gamma_3 + q_{45}© \Gamma_5$$
$$\Gamma_5 = q_{51}© \Gamma_1 + q_{53}© \Gamma_3 + q_{54}© \Gamma_4$$

$$(9\text{-}14)$$

The resulted value of availability U_0 is calculated from the above equations as:

$$U_0 = -\frac{N_2}{D_2}, \tag{15}$$

where,

$$D_2 = [(1 - P_{12}P_{23}P_{31} - P_{12}P_{21})(1 - P_{45}P_{54}) + P_{31}\{-P_{13}(1 - P_{45}P_{54}) - P_{14}(P_{43} + P_{45}P_{53}) - P_{15}(P_{43}P_{54} + P_{53})\} - P_{14}(P_{41} + P_{45}P_{51}) - P_{15}(P_{41}P_{54} + P_{51})] + P_{10}[(P_{02}P_{21} + P_{02}P_{23}P_{31} + P_{01} + P_{03}P_{31})(1 - P_{45}P_{54})] - P_{20}[P_{02}P_{31}\{-P_{13}(1 - P_{45}P_{54}) - P_{14}(P_{43} + P_{45}P_{53}) - P_{15}(P_{43}P_{54} + P_{53})\} + (P_{01}P_{12} + P_{03}P_{12}P_{31})(1 - P_{45}P_{54}) + P_{02}\{(1 - P_{45}P_{54}) - P_{14}(P_{41} + P_{45}P_{51}) - P_{15}(P_{41}P_{54} + P_{51})\}] + P_{30}[(1 - P_{45}P_{54})(P_{03}P_{12}P_{21} - P_{01}P_{12}P_{23}) - (P_{01} + P_{02}P_{21})(P_{13}(1 - P_{45}P_{54}) + P_{14}(P_{43} + P_{45}P_{53}) + P_{15}(P_{43}P_{54} + P_{53})) - (P_{03} + P_{02}P_{23})(1 - P_{45}P_{54}) - P_{14}(P_{41} + P_{45}P_{51}) - P_{15}(P_{41}P_{54} + P_{51})] - P_{40}[(P_{14} + P_{15}P_{54})(P_{02}P_{23}P_{31} + P_{03}P_{31} + P_{01} + P_{02}P_{21})] + \mu_5[(P_{14}P_{45} + P_{15})(P_{02}P_{23}P_{31} + P_{03}P_{31} + P_{01} + P_{02}P_{21})] \tag{16}$$

$$N_2 = \mu_0[(1 - P_{12}P_{23}P_{31} - P_{12}P_{21})(1 - P_{45}P_{54}) + P_{31}\{-P_{13}(1 - P_{45}P_{54}) - P_{14}(P_{43} + P_{45}P_{53}) - P_{15}(P_{43}P_{54} + P_{53})\} - P_{14}(P_{41} + P_{45}P_{51}) - P_{15}(P_{41}P_{54} + P_{51})] + \mu_1[(P_{02}P_{21} + P_{02}P_{23}P_{31} + P_{01} + P_{03}P_{31})(1 - P_{45}P_{54})] + \mu_2[P_{02}P_{31}\{-P_{13}(1 - P_{45}P_{54}) - P_{14}(P_{43} + P_{45}P_{53}) - P_{15}(P_{43}P_{54} + P_{53})\} + (P_{03}P_{12}P_{31} + P_{01}P_{12})(1 - P_{45}P_{54}) + P_{02}\{(1 - P_{45}P_{54}) - P_{14}(P_{41} + P_{45}P_{51}) - P_{15}(P_{41}P_{54} + P_{51})\}] + \mu_4[(P_{14} + P_{15}P_{54})(P_{02}P_{23}P_{31} + P_{03}P_{31} + P_{01} + P_{02}P_{21})] \tag{17}$$

5.   Repairman (r_1) and Inspection Period in The System

As per the system reliability concern, it is always essential to have the best repair mechanism for its products for customer satisfaction and to increase profit. However, as we know, any mechanical and working system has many reasons for failure. So, it becomes more critical to get the failed unit to be inspected to know the nature of the failure and proceed using the correct repair mechanism to avoid wasting time and giving exact information to the customer about the time and cost of repair. Hence the repair mechanism has been distributed into two stages: a) inspection of failure or repairing of minor failure or regular service by the repairman (r_1) and b) repair of major failure denoted by repairman (r_2).

If Ψ_i denotes the repairman (r_1)period of the system at time 't,' then the resulting relations will be designed as:

$$\Psi_0 = q_{01}© \Psi_1 + q_{02}© \Psi_2 + q_{03}© \Psi_3$$
$$\Psi_1 = Z_1 + q_{10}© \Psi_0 + q_{12}© \Psi_2 + q_{13}© \Psi_3 + q_{14}© \Psi_4 + q_{15}© \Psi_5$$
$$\Psi_2 = Z_2 + q_{20}© \Psi_0 + q_{21}© \Psi_1 + q_{23}© \Psi_3$$
$$\Psi_3 = Z_3 + q_{31}© \Psi_1$$
$$\Psi_4 = q_{41}© \Psi_1 + q_{43}© \Psi_3 + q_{45}© \Psi_5$$
$$\Psi_5 = Z_5 + q_{51}© \Psi_1 + q_{53}© \Psi_3 + q_{54}© \Psi_4$$

$$(18\text{-}23)$$

The resulted value of availability V_0 is calculated from the above equations as:

$$V_0 = -\frac{N_3}{D_2} \tag{24}$$

$$N_3 = \mu_1[(P_{02}P_{21} + P_{02}P_{23}P_{31} + P_{01} + P_{03}P_{31})(1 - P_{45}P_{54})] + \mu_2[P_{02}P_{31}\{-P_{13}(1 - P_{45}P_{54}) - P_{14}(P_{43} + P_{45}P_{53}) - P_{15}(P_{43}P_{54} + P_{53})\} + (P_{01}P_{12} + P_{03}P_{12}P_{31})(1 - P_{45}P_{54}) + P_{02}\{(1 - P_{45}P_{54}) - P_{14}(P_{41} + P_{45}P_{51}) - P_{15}(P_{41}P_{54} + P_{51})\}] - \mu_3[(1 - P_{45}P_{54})(P_{03}P_{12}P_{21} - P_{01}P_{12}P_{23}) - (P_{01} + P_{02}P_{21})(P_{13}(1 - P_{45}P_{54}) + P_{14}(P_{43} + P_{45}P_{53}) + P_{15}(P_{43}P_{54} + P_{53})) - (P_{03} + P_{02}P_{23})(1 - P_{45}P_{54}) - P_{14}(P_{41} + P_{45}P_{51}) - P_{15}(P_{41}P_{54} + P_{51})] + \mu_5[(P_{14}P_{45} + P_{15})(P_{02}P_{23}P_{31} + P_{03}P_{31} + P_{01} + P_{02}P_{21})] \tag{25}$$

6.   Repairman (r_2) Period of the System

If Φ_i denotes the repairman (r_2)period of the system at time 't,' then the resulting relations will be designed as:

$$\Phi_0 \ = \ q_{01}© \ \Phi_1 + q_{02}© \ \Phi_2 + q_{03}© \ \Phi_3$$
$$\Phi_1 \ = \ q_{10}© \ \Phi_0 + q_{12}© \ \Phi_2 + q_{13}© \ \Phi_3 + q_{14}© \ \Phi_4 + q_{15}© \ \Phi_5$$
$$\Phi_2 = q_{20}© \ \Phi_0 + q_{21}© \ \Phi_1 + q_{23}© \ \Phi_3$$
$$\Phi_3 \ = \ q_{31}© \ \Phi_1$$
$$\Phi_4 \ = \ Z_4 + \ q_{41}© \ \Phi_1 + q_{43}© \ \Phi_3 + q_{45}© \ \Phi_5$$
$$\Phi_5 \ = \ Z_5 + \ q_{51}© \ \Phi_1 + q_{53}© \ \Phi_3 + q_{54}© \ \Phi_4$$

(26-31)

The resulted value of availability W_0 is calculated from the above equations as:

$$W_0 = -\frac{N_4}{D_2}$$

(32)

$$N_4 = \mu_4[(P_{14} + P_{15}P_{54})(P_{02}P_{23}P_{31} + P_{03}P_{31} + P_{01} + P_{02}P_{21})] + \mu_5[(P_{14}P_{45} + P_{15})(P_{02}P_{23}P_{31} + P_{03}P_{31} + P_{01} + P_{02}P_{21})]$$

(33)

7.   Conclusion

The required steady-state profit is calculated as:

$$P = \ E_1U_0 - \ E_2V_0 - \ E_3W_0$$

(34)

where,

E_1: System per unit up time revenue.
E_2 and E_3: System per unit down time expenditure.

As per analysis, the profit function (P) behaviour has been studied by the fixing specific parameters $E_1, E_2, E_3 p_2.$, and 'a' as:

$$E_1 = 10000, E_2 = 500, E_3 = 2000, p_2 = 0.6 \text{ and } a = 0.7$$

Table 2, 3 and Figure 2, 3 depict the behaviour of reliability parameters, including profit function that decrease and increase as the failure rate p_1 and repair rate r_1 increase from 0.1 to 0.8. Hence, with the help of numerical and graphical analysis, it has been proved that the profit function decreases/increases with increasing/decreasing failure rate. In other words, the research paper's objective to benefit the industries by developing new techniques using prescribed repairing techniques for different failures is verified.

Table 2. Reliability parameter values corresponding to Repair Rate r_1.

Repair Rate	MTSF	U_0	V_0	W_0	PROFIT (P)
	10.4878	0.211063	0.98271	0.00615	1606.977
	5.459438	0.176317	0.988435	0.006454	1256.044
$r_1 = 0.1$	3.813798	0.164058	0.990541	0.006566	1132.178
	3.011392	0.157832	0.991669	0.006627	1069.232
	2.544592	0.154086	0.99239	0.006665	1031.338
	2.244375	0.151598	0.992902	0.006693	1006.148
	2.038438	0.149834	0.99329	0.006714	988.2712
	1.89073	0.148524	0.993598	0.00673	974.9816
	11.02186	0.414257	0.930175	0.017014	3643.452
	5.775144	0.339174	0.954097	0.019551	2875.585
	4.043345	0.308992	0.963807	0.02058	2566.853
$r_1 = 0.3$	3.189426	0.292734	0.969106	0.021139	2400.507
	2.68604	0.282589	0.972464	0.021493	2296.668
	2.357445	0.275666	0.974796	0.021738	2225.784
	2.128361	0.270649	0.97652	0.021919	2174.389
	1.961171	0.266851	0.977852	0.022058	2135.47
	11.67403	0.55911	0.86331	0.026572	5106.3
	6.138472	0.468568	0.906238	0.03337	4165.824
	4.30075	0.427053	0.925924	0.036474	3734.615
$r_1 = 0.5$	3.387312	0.403199	0.937236	0.038248	3486.878
	2.843453	0.387696	0.94459	0.039393	3325.88
	2.484277	0.376799	0.94976	0.040192	3212.728
	2.230545	0.368712	0.953598	0.040779	3128.764
	2.042643	0.362466	0.956563	0.041228	3063.917
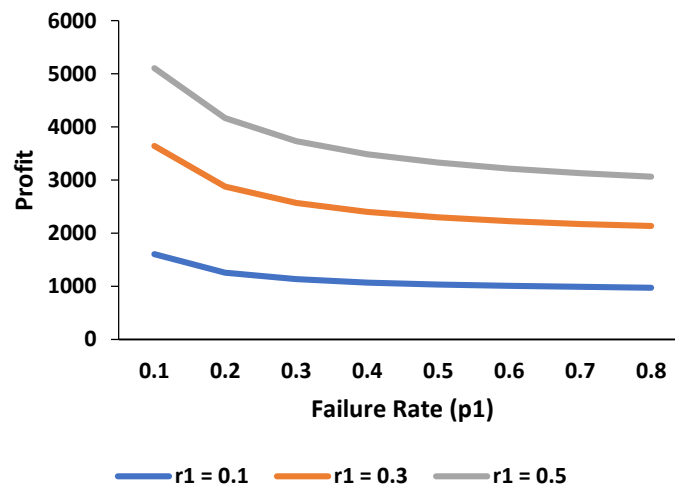
Figure 2. Profit vs Failure Rate p_1

Table 3. Reliability parameters values corresponding to Failure Rate p_1.

Failure Rate	MTSF	U_0	V_0	W_0	PROFIT (P)
	5.459438	0.176317	0.988435	0.006454	1256.044
	5.775144	0.339174	0.954097	0.019551	2875.585
	6.138472	0.468568	0.906238	0.03337	4165.824
$p_1 = 0.2$	6.54955	0.565673	0.85402	0.045619	5138.48
	7.011458	0.637528	0.802755	0.05581	5862.277
	7.529574	0.691005	0.754844	0.064114	6404.404
	8.111476	0.731387	0.711086	0.070861	6816.603
	8.767186	0.762429	0.671518	0.076375	7135.777
	3.011392	0.157832	0.991669	0.006627	1069.232
	3.189426	0.292734	0.969106	0.021139	2400.507
	3.387312	0.403199	0.937236	0.038248	3486.878
	3.608108	0.491995	0.900495	0.05528	4359.146
$p_1 = 0.4$	3.855721	0.563027	0.862002	0.071062	5057.143
	4.135117	0.620001	0.823702	0.085191	5617.777
	4.45265	0.66601	0.786704	0.097635	6071.477
	4.816551	0.703492	0.751581	0.108517	6442.096
	2.244375	0.151598	0.992902	0.006693	1006.148
	2.357445	0.275666	0.974796	0.021738	2225.784
	2.484277	0.376799	0.94976	0.040192	3212.728
$p_1 = 0.6$	2.627628	0.45945	0.920785	0.059412	4015.281
	2.791014	0.527395	0.889918	0.078058	4672.876
	2.979003	0.583671	0.858504	0.09551	5216.442
	3.197645	0.63066	0.827398	0.111527	5669.848
	3.45514	0.670215	0.797124	0.126073	6051.439
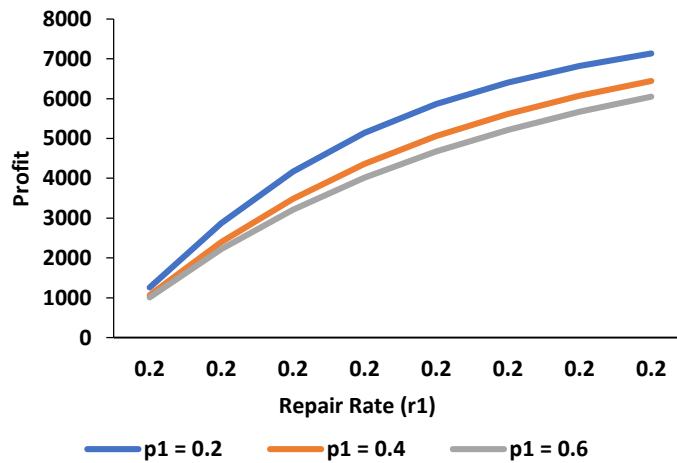
Figure 3. Profit vs Failure Rate r_1

6.   References

Acar E., Solanki K. (2009). System reliability based vehicle design for crashworthiness and effects of various uncertainty reduction measures, Structural and Multidisciplinary Optimization, 39: 311-325.

Adler P., Mallwitz R., (2021). Time-based reliability analysis of electrolytic capacitors for automotive applications using multi-domain simulation, 22nd International Conference on Thermal, Mechanical and Multi-Physics Simulation and Experiments in Microelectronics and Microsystems (EuroSimE), St. Julian, Malta, 1-6.

Bhatti J., Kakkar M. K. (2021). Reliability analysis of cold standby parallel system possessing failure and repair rate under geometric distribution, Recent Advances in Computer Sciences and Communications, 14: 962-968.

Bhatti J., Kakkar M. K., Kaur M., Deepika, Khanna P. (2021). Stochastic analysis to mechanical system to its reliability with varying repairing services, Chebyshevskii Sbornik, 22: 92-104.

Bhatti J., Kakkar M. K., Bhardwaj N., Kaur M., Deepika, (2020). Reliability analysis to industrial active standby redundant system, Malaysian Journal of Science, 39: 74-84.

Bhatti J., Bhardwaj N., Kumar S. (2021). Mathematical modelling to industrial repair and maintenance policy system for its reliability, Mathematical Modeling and Computing, 8: 465-473.

Bhatti J., Kakkar M. K., KaurM. (2021). Stochastic analysis to a power supply system through reliability modelling, Transactions of National Academy of Sciences of Azerbaijan. Series of Physical-Technical and Mathematical Sciences, Issue Mathematics, 41: 35-43.

Chen W. L. (2018). System reliability analysis of retrial machine repair systems with warm standbys and a single server of working breakdown and recovery policy, Systems Engineering, 21: 59-69.

Dai. Y. S., Levitin G. (2006). Reliability and performance of tree-structured grid services, IEEE Transactions on Reliability, 55: 337-349.

Du M., Li Y. F. (2020). An investigation of new local search strategies in memetic algorithm for redundancy allocation in multi-state series-parallel systems, Reliability Engineering & System Safety, 195: 106703.

Haggag M. Y. (2009). Cost analysis of two-dissimilar-unit cold standby system with three states and preventive maintenance using linear first order differential equations, Journal of Mathematics and Statistics, 5: 395-400.

Hua D., Elsayed E. A. (2015). Degradation analysis of k-out-of-n pairs: G balanced systems with spatially distributed units, IEEE Transactions on Reliability, 65: 941-956.

Hua D., Elsayed E. A. (2015). Reliability estimation of k-out-of-n pairs: G balanced systems with spatially distributed units, IEEE Transactions on Reliability, 65: 886-900.

Kumar G., Jain V., Soni U. (2019). Modelling and simulation of repairable mechanical systems reliability and availability, International Journal of System Assurance Engineering and Management, 10: 1221-1233.

Lee S. H., Park T. W., Chung K. H., Choi K. H., Kim K. K., Moon K. H. (2011). Requirement-based testing of an automotive ECU considering the behaviour of the vehicle, International Journal of Automotive Technology, 12: 75-82.

Levitin G., Xing L., Haim H. B., Dai Y. (2013). Reliability of series-parallel systems with random failure propagation time, IEEE Transactions on Reliability, 62: 637-647.

Liu Y., Huang H. Z., (2010). Optimal selective maintenance strategy for multi-state systems under imperfect maintenance, IEEE Transactions on Reliability, 59: 356-367.

Martz H.F., Waller R. A. (1990). Bayesian reliability analysis of complex series/parallel systems of binomial subsystems and components, Technometrics, 32: 407-416.

Mihalache A., Guerin F., Barreau M., Todoskoff A. (2006). Reliability analysis of mechatronic systems using censored data and Petri nets: application on an antilock brake system (ABS), RAMS' 06 Annual Reliability and Maintainability Symposium, IEEE, USA, 140-145.

Nourelfath M., Fitouhi M. C., Machani M. (2010). An integrated model for production and preventive maintenance planning in multi-state systems, IEEE Transactions on Reliability, 59: 496-506.

Perman M., Senegacnik A., Tuma M. (1997). Semi-Markov models with an application to power-plant reliability analysis, IEEE Transactions on Reliability, 46: 526-532.

Popovic P., Ivanovic G., Mitrovic R., Subic A. (2012). Design for reliability of a vehicle transmission system, Proceedings of the Institution of Mechanical Engineers, Part D: Journal of Automobile Engineering, 226: 194-209.

Ram M., Singh S. B., Singh V. V. (2013). Stochastic analysis of a standby system with waiting repair strategy, IEEE Transactions on Systems, Man, and Cybernetics: Systems, 43: 698-707.

SrihariP. V., GovindarajuluK.,Ramachandra K. (2010). A method to improve reliability of gearbox fault detection with artificial neural networks, International Journal of Automotive and Mechanical Engineering, 2: 221-230.

Tian Z., Zuo M. J., Huang H. (2008). Reliability-redundancy allocation for multi-state series-parallel systems, IEEE Transactions on Reliability, 57: 303-310.

ARDUINO BASED SMART SOLAR PHOTOVOLTAIC REMOTE MONITORING SYSTEM

Vinoth Kumar V[1a]*, Sasikala G[2a]

Abstract: The continuous monitoring system of the photo voltaic solar based energy model is currently highly crucial to monitor the overall performance and other related characteristics of energy solar energy systems from remote locations. For this, data loggers also play a vital role. These technologies are highly important to identify any malfunctions inherent in PV based solar energy systems. The proposed IoT based system is useful to obtain real time data from PV based solar energy systems from remote areas. An Arduino ATMEGA16 microcontroller was used to acquire real time data from the system, which is incorporated with the blynk app to transmit real time data to the destination through a webpage. The proposed system consists of a PV based solar system, Arduino controller board Wi-Fi module and the blynk app, in order obtain and transmit data from any remote location. We have developed a cost effective IoT based Smart monitoring system for PV based solar energy applications to monitor the various characteristics and performance of the system, as well as to carry out preventive maintenance and fault detection.

Keywords: Photo-Voltaic (PV), Internet of Things (IoT), solar energy system, monitoring system.

1. Introduction

Renewable energy plays a vital role for fulfilling the energy requirements across the world. Nowadays, researchers are working on smart meter applications, whereby detecting performance and characteristics of PV solar energy systems can be done from a remote location to optimize the overall performance of solar power based applications. The use of renewable energy is required to reduce the environmental pollution generated from the various types of power plants, as well as to reduce greenhouse effects. In this current scenario, Internet of Things (IoT) plays a vital role in order to monitor various parameters from a remote location, and this technology is growing day by day to give application parts to users, due to its communication protocol with an internet connection. Thus, the various parameters of the PV solar energy system are electric potential, temperature, current and intensity of the sun light. These parameters decide the performance of the entire system. Currently, there are many research works that concentrate on the remote monitoring of the important characteristics of PV solar energy systems. A simple prototype model was developed to collect information related to the system without using any automation based tools. In addition, the author used the learning mechanism in order to provide better performance by the system (Hugo T.C et al., 2018). The various performance characteristics were obtained using real time data acquisition with LabVIEW. This

method gives efficient performance characteristics by the system (Amit Kumar Rohit et al., 2017; N.A. Othman et al., 2010). The Microcontroller module was used to evaluate the various parameters of the PV based energy system, which was used to acquire various data from the system and display those data to the user (Kangkana Hazarikaa et al., 2017). An IoT based remote monitoring system was used to continuously acquire different types of characteristics of the PV solar system for the effective tracking of fault detection and maintenance (Soham Adhya et al., 2016). The author proposed an IoT based smart monitoring system for a photovoltaic based solar energy plant in terms prototype using Raspberry pi (Renata I. S. Pereira et al., 2017) . The various performance characteristics, including the light intensity and temperature to the solar panel, were analysed using LabVIEW (Aissa Chouder et al., 2013). The author was proposed a solar energy system using LabVIEW with tracking the sunlight intensity mechanism (Bipin Krishna et al., 2013). The smart metering with a control system strategy was proposed by the author, which includes various control units associated with the PV solar system in order obtain efficient preventive fault detection (R. Nagalakshmi et al., 2014). The PV based solar energy system parameters were monitored using both wired as well as wireless techniques, which were incorporated effectively in the IoT platform (P. Papageorgas et al., 2013). The Arduino based controller and the LabVIEW tool were used in order to monitor the real time data with the use of the inbuilt feature of LabVIEW tool from which the effective data was obtained from the PV system in a graphical manner (Haider-e-Karar et al., 2015). The cost effective IoT based smart monitoring of the PV system was

Authors information:

[a]Department of Electronics and Communication Engineering, Vel Tech Rangarajan Dr. Sagunthala R&D Institute of Science and Technology, 600062, INDIA.
E-mail: vinothkumarv@veltech.edu.in[1], gsasikala@veltech.edu.in[2]
*Corresponding Author: vinothkumarv@veltech.edu.in

proposed by the author in order to analyse the various important characteristics of the PV solar energy system (Bruno Ando et al., 2015). The author effectively used Arduino as well as the Blynk app to measure the various parameters from an agricultural land (Vinoth kumar V et al., 2017).

2. Proposed System

The three-layer architecture of IoT was used for our proposed system in order to transmit the various parameters associated with PV solar energy system. Figure 1 shows the simple three-layer architecture of the IoT device. The first layer of the IoT architecture was used for measuring real time data using various sensors and actuators. In this proposed system, the lower level consists of the sensing unit such as temperature sensor to measure the temperature, an ammeter to measure the current, volt meter to measure the electric potential, and a light intensity sensor in order to measure the intensity of sun light. The various parameters were effectively measured from the PV solar energy system and the measured data was given to the next layer of the IoT architecture, which is the middle layer. The middle layer of the IoT architecture is known as the network and transport layer, and the measured real time data is transmitted through the IoT protocol. The second layer of the IoT architecture is the responsible layer to transmit the measured data to the cloud. Finally, the data pockets are received by the upper layer of the IoT architecture, where the collected data will be displayed to the user using the internet. The Blynk app was effectively used in the application layer of the IoT architecture.
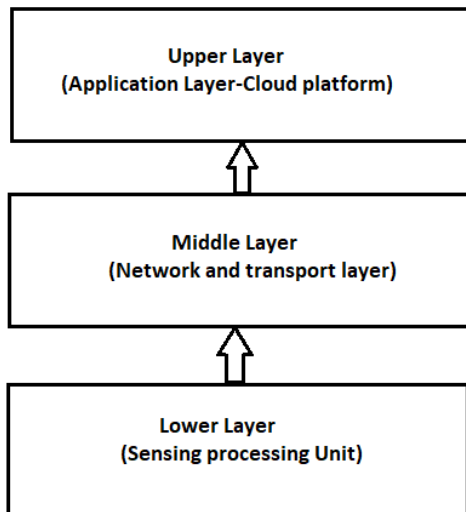
Figure 1. Three layer architecture of IoT

The proposed system block diagram is shown in Figure 2. The parameters such as voltage, current, temperature and light intensity of the PV solar energy system are measured using a voltmeter, ammeter, LM235 temperature sensor and LDR, and those data are given to the arduino controller board. The

these measured data are given as a input the LCD display, which shows the real time data to the user on the field. Simultaneously, the same information is transferred to the cloud platform with the help of the IoT protocol, which is the representation of the Wi-Fi module. Finally, the measured data are transmitted to the user.
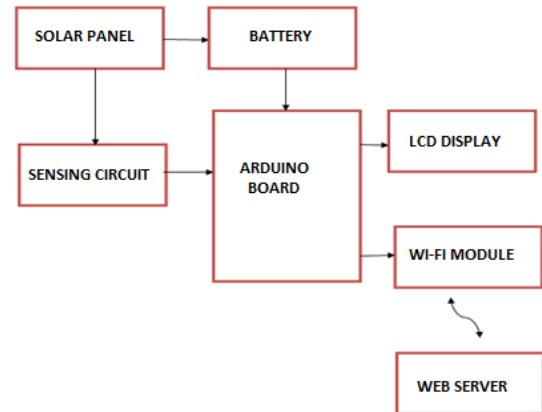
Figure 2. Block diagram of proposed system

An Arduino compiler was used for effective programming, The Arduino IDE was used to upload the embedded C program into the ATMEGA 16 microcontroller chip. The Blynk IoT platform is user friendly, since the data can be easily understandable to the user on the other end. The ESP8266 chip was used to obtain remote information related to the system.

Figure 3. Overall Circuit connection of proposed system

Figure 3 shows the overall prototype setup of the proposed system, which consists of various sensing unit Solar panels as well as the Cloud based devices with the ATMEGA 16 microcontroller unit. The Wi-Fi module ESP8266 was used for reducing the overall system cost, and to get an efficient wireless data transmission. The DC to AC converter was used in the proposed system in order to store the alternating

current in the battery. There is an increase in 10mV of electric potential for every 1°C.

3. Results and Discussions

The acquired parameters are shown in Figure 4, for different times in a day. Figure 4(a) shows the real time data at 12:31 pm, during which the acquired parameters were 15.23 V of electric potential, 6.47 A of electric current, and 63.86 W/m2 of light intensity, at 31.58 °C. Figure 4(b) shows the measurements taken at 1:10 pm. During this time, the various PV parameters were 16.23 V of electric potential, 7.09 A of electric current, and 65.10 W/m2 of light intensity, at 32.23 °C. Figure 4(c) shows the measurements taken at 2:10 pm. During this time, the various PV parameters were 15.98 V of electric potential, 6.91 A of electric current, and 64.86 W/m2 of light intensity, at 31.93 °C. Figure 4(c) shows the final measurements which were taken at 3:06 pm. During this time, the various PV parameters were 14.23 V of electric potential, 5.19 A of electric current, and 58.12 W/m2 of light intensity, at 28.87 °C. The PV parameter variation was observed with respect to the different temperature levels of the day. In the measurement of the first two timings, the electric potential, electric current as well as the intensity were increased. In the last two measurements, it is observed that the electric potential, electric current and light intensity decreases due to the decrease in the temperature level. Those PV solar energy system parameters were observed through the IoT platform using the Blynk app.

Figure 4.(b) Acquired PV parameters at 1:10 PM
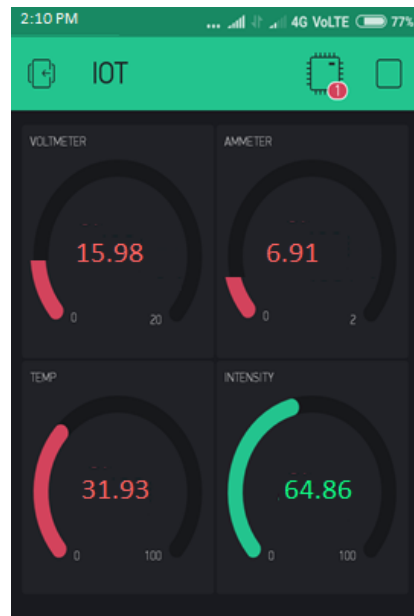
igure 4.(c) Acquired PV parameters at 2:10 PM

Figure 4.(a) Acquired PV parameters at 12:31 PM

Figure 4.(d) Acquired PV parameters at 3:06 PM

The low cost of the proposed system gives effective measurements for the PV solar energy system. Figure 5 shows the plot between temperature and other PV parameters. Figure 5(a) shows the plot between temperature and the electric potential from the PV solar system, from which it is observed that the electric potential increased for first two set of values, and then tends to decrease due to the decrease in the temperature level. Figure 5(b) shows the plot between temperature and the electric current from the PV solar system, from which it is observed that the electric current increased for first two sets of values. It then tends to decrease due to the decrease in the temperature level. Similarly, Figure 5(c) shows the plot between temperature and the light intensity from the PV solar system. It is observed that the light intensity increased for first two sets of values, and then decreases due to the decrease in the temperature level.
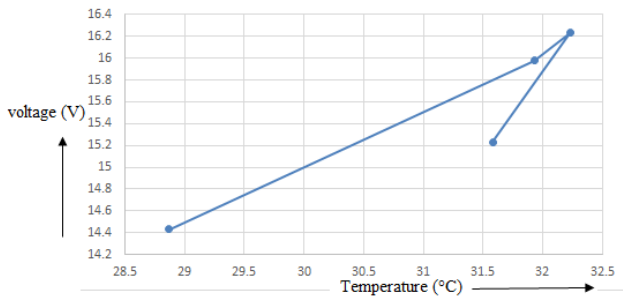
Figure 5(a). Voltage plot for different temperature.
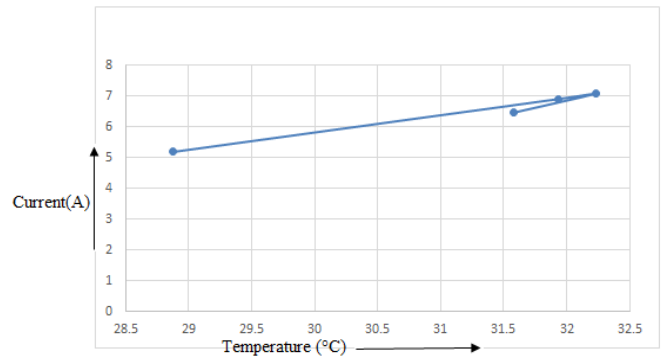
Figure 5(b). Current plot for different temperature.
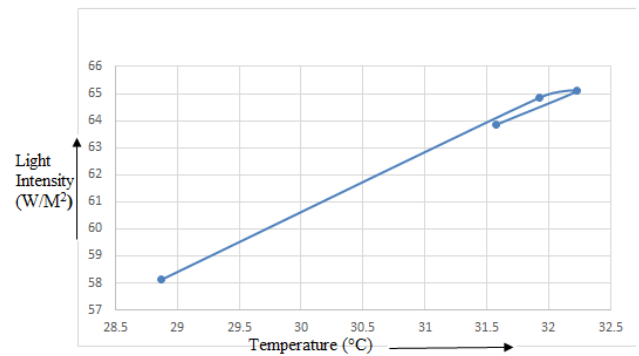
Figure 5(c). Light intensity plot for different temperature.

4.   Conclusion

A cost effective IoT based PV solar energy parameter measuring system was developed in order to avoid faults in the PV solar system, as well as for easy maintenance of the system. Thus, the measured PV parameters such as electric potential, electric current, and light intensity were observed by the user with his smart phone at a remote location, without any interference. The optimized results were observed through the IoT platform using the Blynk app. The proposed system gives effective PV parameter measurements to the user. The parameters can be monitored by the user accurately, quantitatively as well as graphically, and the measurements can be observed effectively by the user.

5.   References

Aissa Chouder, Santiago Silvestre, Bilal Taghezouit, Engin Karatepe (2013), "Monitoring, modelling and simulation of PV systems using Lab VIEW", International Journal of Solar energy, Vol.1, pp.337- 349.

Amit Kumar Rohit, Amit Tomar, Anurag Kumar, Saroj Rangnekar (2017), "Virtual lab-based real-time data acquisition, measurement and monitoring platform for solar photovoltaic module", International Journal of Resource-Efficient Technologies, pp.1-6.

Bipin Krishna, Kaustav Sinha (2013), "Tracking of Sun for Solar Panels and Real-Time Monitoring Using Lab VIEW", Journal of Automation and Control Engineering, Vol. 1, pp.1-4.

Bruno Ando, Salvatore Baglio, Antonio Pistorio (2015), "Sentinella: Smart monitoring of photovoltaic system at panel level", IEEE Transaction on Instrumentation and measurement, Vol.64, pp.2188-2199.

Haider-e-Karar, Aziz Altaf Khuwaja, Abdul Sattar (2015), "Solar Power Remote Monitoring and Controlling Using Arduino, Lab VIEW and Web browser", IEEE International Conference on Power Generation System and Renewable Energy Technologies, pp.1-4.

Hugo T.C. Pedro, Edwin Lim, Carlos F.M. Coimbra (2018), "A database infrastructure to

Implement real-time solar and wind power generation intra-hour forecasts", International Journal of Renewable energy, Vol.123, pp.513-525.

Kangkana Hazarikaa, Pradyumna Kumar Choudhurya (2017), "Automatic monitoring of solar photovoltaic (SPV) module", Science direct proceedings, Vol. 4, pp.12606–12609.

N.A. Othman, N.S. Damanhuri, I.R. Ibrahim, R. Radzali, M.N. Mohd (2010), "Automated Monitoring System for Small Scale Dual-Tariff Solar PV plant in UiTM Pulau Pinang", Proceedings of the World Congress on Engineering(WCE) U.K, Vol.2, pp.1-3.

P. Papageorgas, D. Piromalis, K. Antonakoglou, G. Vokas, D. Tseles and K. G. Arvanitis (2013), "Smart Solar Panels: In-situ monitoring of photovoltaic panels based on wired and wireless sensor networks", International Conference on Advancements in Renewable Energy and Clean Environment, Vol.36,pp.535- 545.

R. Nagalakshmi, B. Kishore Babu, D. Prashanth (2014), "Design and Development of a Remote Monitoring and Maintenance of Solar Plant Supervisory System", International Journal of Engineering and Computer Science, Vol.3, pp.9382-9385.

Renata I. S. Pereira, Ivonne M. Dupont, Paulo C. M. Carvalho, Sandro C. S. Juca (2017), " IoT Embedded Linux System based on Raspberry Pi applied to Real-Time Cloud Monitoring of a decentralized Photovoltaic plant", International Journal of measurement ,Vol.2,pp.1-18.

Soham Adhya, Dipak Sara, Abhijit Das, Joydip Jana, Hiranmay Saha (2016), "An IoT Based Smart Solar Photovoltaic Remote Monitoring and Control unit", IEEE International Conference on Control, Instrumentation, Energy & Communication (CIEC), pp.432-436.

Vinoth kumar V., Ramasamy R. Janarthanan S, and VasimBabu M (2017), "Implementation of IoT in smart irrigation system using Arduino processor", International journal of Civil Engineering and Technology, pp. 1304-1314.

THE MOLECULAR BEHAVIORS OF CALIXARENES AT THE AIR-WATER INTERFACE: DENSITY FUNCTIONAL THEORY, SURFACE PRESSURE, POTENTIAL, AND EFFECTIVE DIPOLE MOMENT

Faridah Lisa Supian[1a]*, Wong Yeong Yi[2a], Nur Farah Nadia Abd Karim[3a], Afiq Radzwan[4a], Darvina Lim Choo Kheng[5a], Abdullah Faisal Al Naim[6b]

Abstract: This study examined the behaviors of Langmuir-Blodgett ultrathin calixarene films at the air-water interface. The Langmuir trough was used to estimate the surface pressure, surface potential, and effective dipole moment of two calixarenes, namely, calix[4]arene (THC4) and calix[8]arene (THC8). The band gap was determined using the density functional theory (DFT). The DFT simulation gave a band gap of 2.28 eV for THC4, confirming that THC4 was an insulator. The surface pressure isotherms of THC4 and THC8 yielded the expected molecular behavior from the gaseous to the solid phases. THC4 and THC8 showed a perpendicular and a parallel orientation in the air-water subphase, respectively. The ΔVmax values of TCH4 and THC 8 were 205 mV and 141mV, respectively, and their µ₊max values were 0.147 D and 0.088 D, respectively.

Keywords: Calixarene, density functional theory, effective dipole moment, Langmuir-Blodgett, surface potential

1. Introduction

Nanomaterials are important inventions for many applications, such as nanosensors and drug delivery systems (Azahari et al., 2012; Lim et al., 2020). In particular, the contribution of host-guest nano-molecules, known as calixarenes, encompasses various sectors, including biosensors, healthcare, biomedical, and transport agents in biological systems Edwards et al., 2021; Kumar et al., 2019; Sanabria Español & Maldonado, 2019). Structurally, calixarenes consist of repeating phenol units linked via alkylidene groups with unique upper rims and basket-like lower rims (Shinkai, 1993). Calixarenes are electrical insulators, and reduced graphene oxide (rGO) enhances the electric conductivity of the non-conductive material (Lim et al., 2020; Al-Rubaye et al., 2017; Echabaane et al., 2013).

The structure and properties of calix[4]arene derivatives and other related guest molecules were studied using the density-functional theory (DFT). These properties included the total interaction energy, electrochemical, and photophysical properties (Ortolan et al., 2018; Sharma et al., 2020). However, studies on the density of state (DOS) and

band gap of calix[4]arene are scarce, if not nonexistent. The band gap is the primary factor determining a material's properties and electrical conductivity (Loa et al., 2018; Wu et al., 2020). Elementary experimental studies of calixarene also are crucial to mimic their potential applications. Also, the surface pressure, surface potential, and effective dipole moment were studied using the Langmuir-Blodgett trough in this work (Azahari et al., 2012).

In this study, the behavior of calix[4]arenes at the air-water interface was investigated using a combination of the theoretical and experimental approaches.

2. Methodology

2.1 The DFT Study of Calixarene

This study investigated two calixarenes, i.e., 25, 26, 27, 28-tetrahydrocalix[4]arene, and 49, 50, 51, 52, 53, 54, 55, 56-octahydroxycalix[8]arene. They were abbreviated as THC4 and THC8, respectively. For the theoretical study, quantum ESPRESSO (QE) was used to estimate the DOS and band gap of calixarenes based on their optimized structures (Liao et al., 2021; Woods-Robinson et al., 2020).

DOS was calculated according to the method of first-principle pseudopotential implemented in the QE simulation with the plane-wave as a basis set (Giannozzi et al., 2009). Geometry optimization was performed using the generalized gradient approximation (GGA) in the form of Perdew–Berke–

Authors information:

[a]Department of Physics, Faculty of Science and Mathematics, Sultan Idris Education University (UPSI), MALAYSIA. E-mail: faridah.lisa@fsmt.upsi.edu.my[1], wongyeongyi97@gmail.com[2], farahnadia2512@gmail.com[3], afiq@fsmt.upsi.edu.my[6], darvinalim@gmail.com[5]

[b]Department of Physics, College of Science, King Faisal University, SAUDI ARABIA. E-mail: anaim2@kfu.edu.sa

*Corresponding Author: faridah.lisa@fsmt.upsi.edu.my

Erzndof (PBE) as an exchange-correlation function to treat the electron-electron interaction (Lawal et al., 2017; Yazyev et al., 2010). All electron-ion core interactions for C, H, and O atoms were treated using full relativistic norm-conserving pseudopotentials of the standard solid-state pseudopotential library (Dal Corso, 2014) Plane-wave basis sets with kinetic energy cutoffs of 25 Ry and 225 Ry were used for expanding the electron wave functions and charge density, respectively. K-points were generated by the irreducible Brillouin zone sampled with a set of (1, 1, 1) Monkhorst-Pack grid using the Gaussian smearing technique for calculating DOS. The geometry optimization was calculated using the Born-Oppenheimer approximation by determining the cell dimension and atomic positions. Within the adopted numerical approximations, the energy function was minimized using the intrinsic Broyden-Fletcher-Goldfarb-Shanno (BFGS) algorithm until their maximum atomic forces were lower than the threshold of $1.0\times〚10〛^{-3}$ Ry/Bohr (Giannozzi et al., 2009). Figure 1 shows the interactive chemical structure for the model of calix[4]arene derived from the crystallographic information file (CIF) in QE.
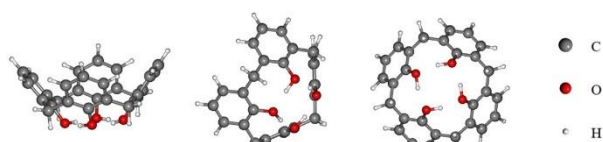
Figure 1. The interactive chemical structure for the model of calix[4]arene in three dimensions.

The contribution of each atom in a structure was quantified based on the valence and conduction band peaks of a DOS curve (Hu & Shang, 2019). Also, the band structure was used to determine the contribution of atoms in the conduction and valence band (Shen et al., 2016). Besides, the structure properties, i.e., whether the structure was a conductor, semiconductor, or insulator, were determined (Kumar et al., 2016).

2.2 Surface Pressure-Area (Π-A), Surface Potential-Area (ΔV - A), and Effective Dipole Moment-Area (μ⊥-A) Isotherms

Experiments of this study were conducted in a 1K cleanroom at room temperature. Calixarenes of 0.2 mg/ml were formed and spread on an air-water subphase. A KSV NIMA 2002 System 2 Langmuir-Blodgett deposition trough attached with a KSV SPOT was used for the experiments. The ΔV-A of the calix[n]arene monolayer was determined using the vibrating plate capacitor method with the KSV SPOT probe at a sensitivity of 1 mV. Deionized water with a resistivity of 18.2 MΩ.cm was gently put into the trough with the surface pressure monitored and stabilized at 25 °C. The monolayer was then compressed symmetrically with two hydrophilic barriers at 12 mm/min. At the onset of the compression, both Π-A and ΔV-A isotherms were performed

simultaneously using the KSV. Extrapolating Π-A isotherm graph yielded the mean molecular area for THC4 and THC8. Therefore, their experimental radius was calculated using the formula for computing the area of a circle.

The surface potential-area (ΔV-A) value of the calixarene monolayer was obtained simultaneously during the Π-A isotherm experiment. Further assessment of ΔV-A values was induced to the average effective dipole moment (μ⊥) by the Helmholtz equation (Azahari et al., 2012).

3.　Results and Discussions

3.1 The DFT study

The total DOS (TDOS) and partial DOS (PDOS) were calculated to elucidate the band characteristics of THC4 (Radzwan et al., 2020). Figure 2 below shows each atom's TDOS and PDOS. The Fermi energy was -3.346 eV and located in the band gap, confirming that THC4 was an insulator (Jin et al., 2021; Khazaei et al., 2016). The C atom gave the highest contribution in both valences (p) and conduction bands (x) compared to O (valence q; conduction bands y) and H (valence r; conduction bands z). The O atoms gave nearly the same contribution as the H atoms in the valence band while showing the lowest contribution in the conduction band. Overall, C atoms contributed to the band gap. This finding agreed with Gillespie and Martsinovich (2019) and Wu et al. (2021). The dominance of C atoms in DOS was due to its unique electron configuration (Wu et al., 2020).
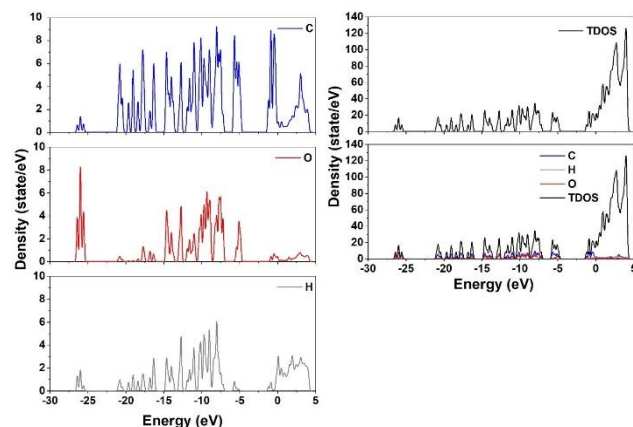
Figure 2. DOS versus the energy of carbon, oxygen, hydrogen, TDOS, and PDOS.

The band gap is 2.28 eV (As in Table 1). However, the band structure based on the PBE exchange-correlation potential underestimated the band gap of insulating materials (Morales-García et al., 2017). With PBE treatment, the actual THC4 band gap should be higher than this computed value. Table 1 shows the bandgap values of calixarenes from other studies. These derivatives were widely used in different applications, such as the fabrication of organic light-emitting diodes, organic optoelectronic

devices, solar cells, photocatalysts, and thermistors (Leontie et al., 2018; Sharma et al., 2020; Wang et al., 2020). Meanwhile, the conductivity, the threshold of 3.0 eV was used to estimate the conductivity of THC4 (Wu et al., 2020).

Table 1. Band gap values of several calix[4]arenes derivatives.

Nanomaterials	Band gap (eV)	References
25, 26, 27, 28-tetrahydrocalix[4]arene (THC4)	2.280	This study
p-tert-butyl-calix[4]arene	3.581 3.582 3.583 3.594	(Sharma et al., 2020)
tertbutylcalix[4]arene with propargyl bromide	1.850 2.640 2.770 3.650 3.830	(Leontie et al., 2018)
Thiacalix[4]arene-Protected Titanium-oxo	2.190 2.240	(Wang et al., 2020)

3.2 Studies of Π-A, ΔV-A, and μ⊥-A Isotherm for THC4 and THC8

Figure 3 shows the Π-A isotherms of TCH4 and TCH8. As the volume of the solution increased, THC isotherms shifted gradually to the right-hand side (Figure 3a) while the THC8 curves remained nearly the same. The intermolecular packing structures between these two calixarenes might have caused their different isothermic behaviors (Dhanabalan et al., 1999).

(a)

(b)
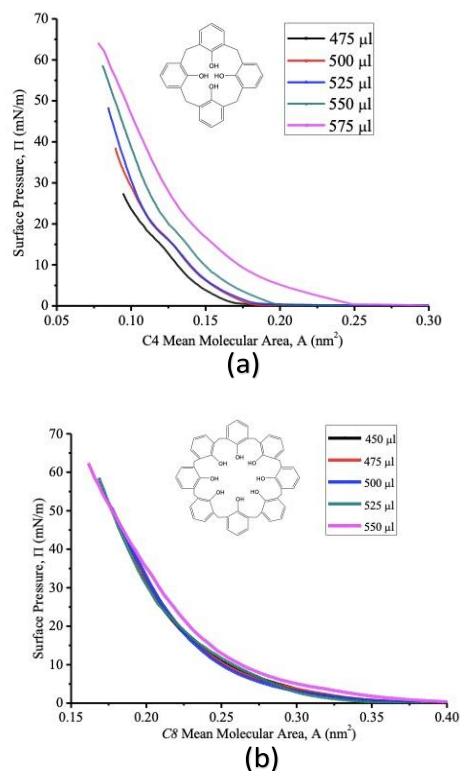
Figure 3. Π-A isotherms: (a) THC4 and b) THC8.

The calixarene molecules moved closer to each other when barriers were shifted to reduce the trough area, changing the surface pressure substantially. Besides, the isotherms of THC4 and THC8 showed the same smooth pattern of phase transition. The molecular transition from the gaseous to liquid, and later, solid phases, showed no flexure before achieving the highest possible surface pressure. Eventually, these phases overlapped into the three-dimensional structure and collapsed.

65

Table 2. The Π-A isotherms of the Langmuir monolayer for calixarenes.

The Langmuir monolayer	Mean molecular area (nm²)	Radius (nm)	Orientation at the air-water subphase
THC4	0.135	0.207	
	0.134	0.207	Parallel
	0.127	0.201	
	0.139	0.210	
	0.157	0.224	
THC8	0.251	0.283	
	0.237	0.275	Perpendicular
	0.242	0.278	
	0.232	0.272	
	0.250	0.282	

Table 2 shows the experimental mean molecular area, radius, and the possible orientations of THC4 and THC8 ring against the water surface plane. The experimental mean molecular area of THC4 was smaller than THC8 by nearly half since THC4 comprised four phenolic units while THC8 was

eight. Therefore, the optimal mean molecular area and radius for THC4 were 0.13 nm² and 0.21 nm, respectively. The optimal mean molecular area and radius for THC8 were 0.24 nm² and 0.27 nm, respectively.
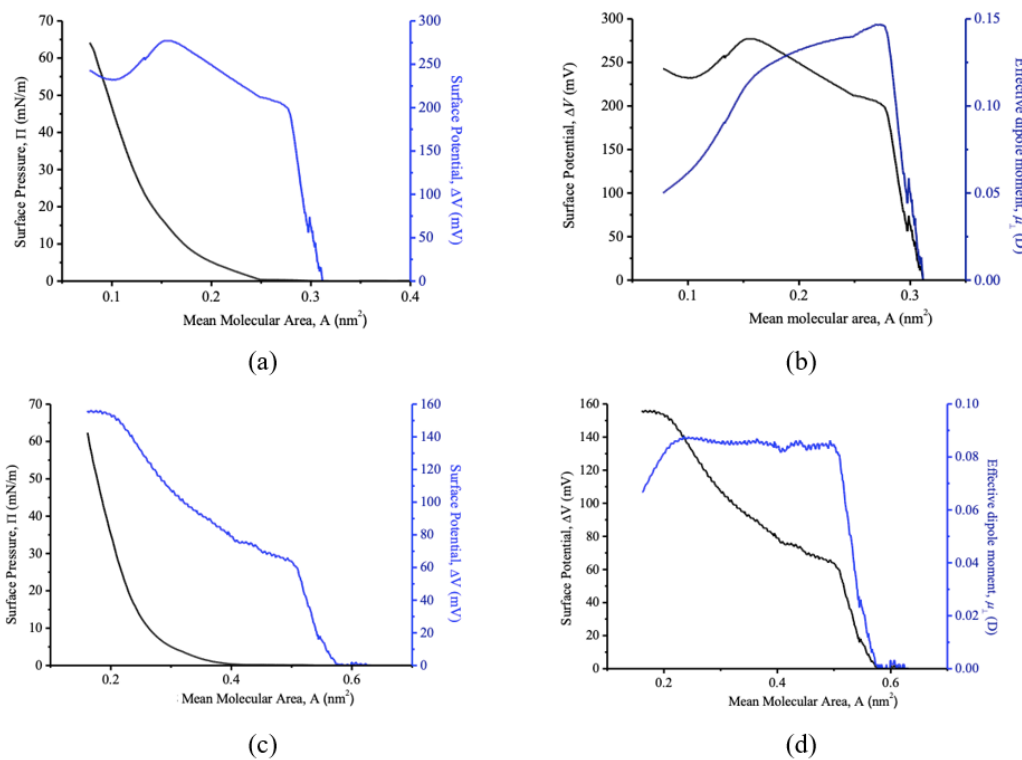
Figure 4. (a) The Π-A isotherm and ΔV-A of THC4, (b) the μ⊥-A isotherm of THC4, (c) the Π-A isotherm and ΔV-A of THC8, and (d) the μ⊥-A isotherm of THC8.

Figure 4 compares the Π-A, ΔV-A, and μ⊥-A isotherms THC4 THC8. ΔV values increased at 0.31 nm² before Π increased at 0.25 nm² (Figure 4a) with the ongoing compression because the molecules began rearranging themselves. Flexures occurred in the ΔV and μ⊥ when THC4 changed from the gaseous to the liquid phase at 15 mN/m, coinciding with the sudden rapid increase in Π at 0.15 nm². Another flexure occurred at 0.27 nm² because the molecules aligned themselves, arranging in a uniform gaseous state. However, the μ⊥ started to decline from 0.27 nm² onward when the molecular area decreased.

Figures 4c and 4d show the Π-A, ΔV-A, and μ⊥-A isotherms of THC8. Similar to THC4, the ΔV values of THC8 also showed the same increasing pattern. Specifically, the ΔV values of THC8 increased first at 0.57 nm² before Π escalated at 0.40 nm². An obvious flexure occurred in the ΔV-A curve at 0.50 nm², indicating that the THC8 molecules changed into the better-arranged gaseous phase. A sudden change also happened in the μ⊥-A isotherm of THC8. When the THC8 molecules transformed into the liquid phase, minor flexure occurred in the ΔV-A curve at 0.40 nm². The μ⊥ of THC8 remained nearly constant, starting from the point at 0.23

66

nm^2 to 0.5 nm^2 when the THC8 molecules went through a substantially greater alignment before 0.5 nm^2. Thus, after the 0.5 nm^2, the molecules improved their alignment slightly with little changes in the μ⊥ throughout the entire compression (Supian, 2010). Thus, 30 mN/m was the selected surface pressure for depositing calixarene on the substrate because the three calixarenes existed in the solid phase.

Table 3 shows the maximum ΔV (ΔVmax) of THC4 and THC8 based on the maximum μ⊥ (μ⊥max) on the isotherms. These data were the results of the arrangement, orientation, and interaction among the calixarene molecules.

Table 3. The maximum ΔV (ΔVmax) of THC4 and THC8 based on ΔV-A and μ⊥-A isotherms.

Calixarenes	Volume (μl)	ΔV$_{max}$ (mV)	μ⊥$_{max}$ (D)
THC4	575	205	0.147
THC8	550	141	0.088

4.   Conclusion

This study investigated the behavior of Langmuir-Blodgett ultrathin films at the air-water interface for two calixarenes, namely calix[4]arene and calix[8]arene. The DFT study estimated the band gap as 2.28 eV based on the DOS calculation. The Fermi energy in the band gap verified that the calixarene was an insulator. Π-A isotherms were formed. THC4 and THC8 showed a perpendicular and a parallel orientation in the air-water subphase, respectively. ΔVmax values of TCH4 and THC8 were 205 mV and 141mV, respectively, and their μ⊥max values were 0.147 D and 0.088 D, respectively.

5.   Acknowledgements

6.   References

Al-Rubaye, S., Rajagopalan, R., Dou, S. X. & Cheng, Z. (2017). Facile synthesis of a reduced graphene oxide wrapped porous NiCo 2 O 4 composite with superior performance as an electrode material for supercapacitors. Journal of Materials Chemistry A, 5(36), 18989-18997.

Azahari, N. A., Supian, F. L. & Malik, S. A. (2012). Interaction Between Langmuir Films Of Calix [4] Arenes With Aqueous Lead Ions.

Dal Corso, A. (2014). Pseudopotentials periodic table: From H to Pu. Computational Materials Science, 95, 337-350.

Dhanabalan, A., Gaffo, L., Barros, A. M., Moreira, W. C. & Oliveira, O. N. (1999). Surface pressure and surface potential isotherms of ytterbium bisphthalocyanine Langmuir monolayers. Langmuir, 15(11), 3944-3949.

Echabaane, M., Rouis, A., Bonnamour, I. & Ouada, H. B. (2013). Optical, electrical and sensing properties of β-ketoimine calix [4] arene thin films. Materials Chemistry and Physics, 141(2-3), 781-789.

Edwards, N. Y., Schnable, D. M., Gearba-Dolocan, I. R. & Strubhar, J. L. (2021). Terpyridine-Functionalized Calixarenes: Synthesis, Characterization and Anion Sensing Applications. Molecules, 26(1), 87.

Giannozzi, P., Baroni, S., Bonini, N., Calandra, M., Car, R., Cavazzoni, C., ... & Wentzcovitch, R. M. (2009). QUANTUM ESPRESSO: a modular and open-source software project for quantum simulations of materials. Journal of physics: Condensed matter, 21(39), 395502.

Gillespie, P. N. & Martsinovich, N. (2019). Origin of charge trapping in TiO2/reduced graphene oxide photocatalytic composites: Insights from theory. ACS applied materials & interfaces, 11(35), 31909-31922.

Hu, R. & Shang, J. (2019). Quantum capacitance of transition metal and nitrogen co-doped graphenes as supercapacitors electrodes: A DFT study. Applied Surface Science, 496, 143659.

Jin, K. H., Yeom, H. W. & Liu, F. (2020). Doping-induced topological phase transition in Bi: The role of quantum electronic stress. Physical Review B, 101(3), 035111.

Karmakar, A., Karthick, K., Sankar, S. S., Kumaravel, S., Madhu, R. & Kundu, S. (2021). A vast exploration of improvising synthetic strategies for enhancing the OER kinetics of LDH structures: a review. Journal of Materials Chemistry A, 9(3), 1314-1352.

Khazaei, M., Ranjbar, A., Arai, M. & Yunoki, S. (2016). Topological insulators in the ordered double transition metals M 2' M ''C 2 MXenes (M'= Mo, W; M ''= Ti, Zr, Hf). Physical Review B, 94(12), 125152.

Kumar, A., Balasubramaniam, K. R., Kangsabanik, J. & Alam, A. (2016). Crystal structure, stability, and optoelectronic properties of the organic-inorganic wide-band-gap

perovskite CH 3 NH 3 BaI 3: candidate for transparent conductor applications. Physical Review B, 94(18), 180105.

Kumar, R., Sharma, A., Singh, H., Suating, P., Kim, H. S., Sunwoo, K., ... & Kim, J. S. (2019). Revisiting fluorescent calixarenes: from molecular sensors to smart materials. Chemical reviews, 119(16), 9657-9721.

Lawal, A., Shaari, A., Ahmed, R. & Jarkoni, N. (2017). First-principles investigations of electron-hole inclusion effects on optoelectronic properties of Bi2Te3, a topological insulator for broadband photodetector. Physica B: Condensed Matter, 520, 69-75.

Leontie, L., Danac, R., Carlescu, A., Doroftei, C., Rusu, G. G., Tiron, V., ... & Susu, O. (2018). Electric and optical properties of some new functional lower-rim-substituted calixarene derivatives in thin films. Applied Physics A, 124(5), 1-12.

Liao, Y., Peng, R., Peng, S., Zeng, W. & Zhou, Q. (2021). The adsorption of H2 and C2H2 on Ge-doped and Cr-doped graphene structures: A DFT study. Nanomaterials, 11(1), 231.

Lim, D. C., Supian, F. L. & Hamzah, Y. (2020). Langmuir, Raman, and electrical properties comparison of calixarene and calixarene-rGO using Langmuir Blodgett (LB) technique. Journal of Materials Science: Materials in Electronics, 31(21), 18487-18494.

Loa, I., Popuri, S. R., Fortes, A. D. & Bos, J. W. G. (2018). Critical mode and band-gap-controlled bipolar thermoelectric properties of SnSe. Physical Review Materials, 2(8), 085405.

Morales-García, Á., Valero, R. & Illas, F. (2017). An empirical, yet practical way to predict the band gap in solids by using density functional band structure calculations. The Journal of Physical Chemistry C, 121(34), 18862-18866.

Ortolan, A. O., Øestrøm, I., Caramori, G. F., Parreira, R. L., Munoz-Castro, A. & Bickelhaupt, F. M. (2018). Anion recognition by organometallic calixarenes: analysis from relativistic DFT calculations. Organometallics, 37(13), 2167-2176.

Radzwan, A., Lawal, A., Shaari, A., Chiromawa, I. M., Ahams, S. T. & Ahmed, R. (2020). First-principles calculations of structural, electronic, and optical properties for Ni-doped Sb2S3. Computational Condensed Matter, 24, e00477.

Sanabria Español, E. & Maldonado, M. (2019). Host–guest recognition of pesticides by calixarenes. Critical reviews in analytical chemistry, 49(5), 383-394.

Shah, A. (2020). A novel electrochemical nanosensor for the simultaneous sensing of two toxic food dyes. ACS omega, 5(11), 6187-6193.

Sharma, V. S., Sharma, A. S., Worthington, S. J., Shah, P. A. & Shrivastav, P. S. (2020). Columnar self-assembly, electrochemical and luminescence properties of basket-shaped liquid crystalline derivatives of Schiff-base-moulded p-tert-butyl-calix [4] arene. New Journal of Chemistry, 44(47), 20610-20619.

Shen, J., Chen, Z., Zheng, L., Li, W. & Pei, Y. (2016). Single parabolic band behavior of thermoelectric p-type CuGaTe 2. Journal of Materials Chemistry C, 4(1), 209-214.

Shinkai, S. (1993). Calixarenes-the third generation of supramolecules. Tetrahedron, 49(40), 8933-8968.

Supian, F.L. (2010). Sensing interactions within nanoscale calixarene and polysiloxane Langmuir-Blodgett films (Doctoral dissertation, The University of Sheffield).

Wang, X., Yu, Y., Wang, Z., Zheng, J., Bi, Y. & Zheng, Z. (2020). Thiacalix [4] arene-Protected Titanium–Oxo Clusters: Influence of Ligand Conformation and Ti–S Coordination on the Visible-Light Photocatalytic Hydrogen Production. Inorganic chemistry, 59(10), 7150-7157.

Woods-Robinson, R., Han, Y., Zhang, H., Ablekim, T., Khan, I., Persson, K. A. & Zakutayev, A. (2020). Wide band gap chalcogenide semiconductors. Chemical reviews, 120(9), 4007-4055.

Wu, B., Zhang, L., Jiang, B., Li, Q., Tian, C., Xie, Y., ... & Fu, H. (2021). Ultrathin porous carbon nitride bundles with an adjustable energy band structure toward simultaneous solar photocatalytic water splitting and selective phenylcarbinol oxidation. Angewandte Chemie International Edition, 60(9), 4815-4822.

Wu, W., Gong, S. & Sun, Q. (2020). Electronic band structure phase diagram of 3D carbon allotropes from machine learning. Diamond and Related Materials, 108, 107990.

Yazyev, O. V., Moore, J. E. & Louie, S. G. (2010). Spin polarization and transport of surface states in the topological insulators Bi 2 Se 3 and Bi 2 Te 3 from first principles. Physical review letters, 105(26), 266806.

SYSTEMATIC LITERATURE REVIEW ON 3D PRINTING PERSONALISED FOOD FOR THE ELDERLY

Muhammad Salahuddin Haris[1a]*, Nur Fatin Adlin Kamarudin[2a], Khairul Auni Adli Mohamed Aini[3a], Harith Juwaidi Abdul Rais[4a], Shaiqah Mohd Rus[5a] and Sakinah Harith[6b]

Abstract: Three-dimensional (3D) printing is currently a new technology being developed in the food industry due to its ability to design, customize, and fabricate a product with good precision and accuracy. Therefore, with regard to the mastication problems frequently faced by elderly people, this technology is utilized to design foods that can be consumed by them. Since there was limited published literature on the subject, the present study aimed to systematically review 3D printing personalized food for the elderly. The study used PRISMA as a guideline for report writing while integrating multiple research designs. This paper employed three databases to select the articles: Science Direct, Scopus, and Google Scholar. The study included five analyzed themes: 1) hardness; 2) moisture; 3) viscosity; 4) elasticity; and 5) printability. The study significantly contributed to several practical purposes and the body of knowledge. The findings provided the factors affecting the 3D printing of food, its mechanisms, and its significance.

Keywords: 3D Printing, personalized food, elderly

1. Introduction

3D food printing is a newly developed method involving food manufacturing through the layering method of producing a 3D-structured model (Derossi et al., 2020a; Hamilton et al., 2018; Huang et al., 2019; Jonkers et al., 2020; Zheng et al., 2019). It requires special computer-aided design (CAD) software to create the shape and design of the product by using a specific digital fabricating machine and to print it mainly through the extrusion method (Huang et al., 2019; Liu et al., 2018; Maniglia et al., 2019; Oyinloye & Yoon, 2020). The printing system is comprised of a syringe that is filled up with viscous food material, which will be printed out through a nozzle that could move in any direction during the process (Chen et al., 2018). This method enables the production of a complex, detailed, and specific shape of a food product (Zheng et al., 2019). Due to its promising contribution to the food industry, research in 3D food printing has gained traction (Maniglia et al., 2019).

This review focuses on aspects including hardness, moisture, viscosity, elasticity, and printability. The customization can be made by adjusting the ingredients of the printed product, also known as the food ink of the machine, based on the product's rheological properties by incorporating structuring agents such as hydrocolloids (Derossi et al., 2020b). The base of the ink is made of edible matter, either nutritional food or snacks (Huang et al., 2019), enabling the development of personalized food for selected populations based on age, health condition, and specific nutritional demand (Dankar et al., 2018; Maniglia et al., 2019).

As for the challenges of 3D food printing, the product printability is affected by the physical appearance, nutritional value, or rheological properties (Maniglia et al., 2019). The printer properties, such as the nozzle size, distance between the nozzle and the printing bed, and speed of printing, can affect the precision of the printing process and end-product (Dankar et al., 2018). Moreover, the transient temperature, surrounding conditions, and ingredients used as the formulation also determine the printing accuracy (Garcia-Segovia et al., 2020; Oyinloye & Yoon, 2020). Some raw materials can be a challenge due to their unstable structure and difficulty integrating with other materials (Zheng et al., 2019). If an ingredient can be used, its homogeneous or heterogeneous form requires specific conditions to form an accurate shape and suitable rheological properties for consumption and to withstand the conditions of cooking and long-period storage (Dick et al., 2020; Hamilton et al., 2018).

This systematic review focuses on the details of the 3D food printing process relating to elderly consumers because they are well-known to experience several physiological

Authors information:

[a]Department of Pharmaceutical Technology, Kulliyyah of Pharmacy, International Islamic University Malaysia, Jalan Sultan Ahmad Shah, 25200 Kuantan, Pahang, MALAYSIA. Email: solah@iium.edu.my[1], fatinelena97@gmail.com[2], auniadli1207@gmail.com[3], harithsktp@gmail.com[4], shaiqahmohdrus@gmail.com[5]

[b]Nutrition and Dietetic Programme, Faculty of Health Sciences, Universiti Sultan Zainal Abidin, Gong Badak Campus, 21300 Kuala Nerus, Terengganu, MALAYSIA. Email: sakinahharith@unisza.edu.my[6b]

*Corresponding Author: solah@iium.edu.my

changes, dysphagia, and require specific nutrition to maintain their well-being (Dankar et al., 2018; Derossi et al., 2020a). By using the right materials and conditions, a specific, nutritious, and easily swallowed printed food with acceptable rheological properties can be manufactured (Jonkers et al., 2020; Maniglia et al., 2020).

1.1 Research Gap – The Existing Research Conducted On 3D Food Printing for The Elderly

It is undeniable that 3D food printing has widely become an area of interest among scholars due to its promising future in the food industry (Dankar et al., 2018; Derossi et al., 2020a; Huang et al., 2019; Liu & Ciftci, 2019; Oyinloye & Yoon, 2020). Although there are many papers discussing this topic, there are limited studies that address a definite food design for specific populations, such as the elderly. Thus, this systematic literature review (SLR) was conducted to collect the data and specify the required characteristics to create 3D printed food for the elderly. The key to SLR was to create a research protocol to ease the process of searching for articles through a variety of databases before selecting and reviewing them (Shaffril et al., 2020a). Throughout the process, there was a classification, inclusion, exclusion, and critical selection using formulated questions to procure the best article for the selected topic.

This SLR was guided by the research question: How can 3D printing be applied to producing personalized food for the elderly? It was conducted to discuss the application of 3D printing to produce personalized food for the elderly based on their needs and acceptability. The technology of 3D food printing can precisely personalize their nutritional needs to improve their quality of life and address swallowing difficulties. Thus, the public or even researchers can determine the food characteristics that can be prepared by using this printing technology.

2. Method

2.1 The Review Protocol – PRISMA

The review was conducted following the PRISMA (Preferred Reporting Items for Systematic Reviews and Meta-Analyses) 2009 checklist that contains items related to the systematic review content and serves as a tool to evaluate the comprehensiveness of the systematic review reporting (Liberati et al., 2009; Moher et al., 2009). The checklist consists of seven major sections: Title, Abstract, Methods, Results, Discussion, and Findings. Each must be accompanied by a rational elaboration, a pedagogical guide, and related examples (Page & Moher, 2017).

2.2 Formulation of Research Questions

To formulate the most suitable research questions, PICo (Population or Problem, Interest and Context) was used, which represents the primary concepts in a research review. For this study, the three major concepts in this review were elderly (population), personalized food (interest), and 3D printing (context) and were employed as keywords to develop the research questions. For example, "How can 3D printing be applied to produce personalized food for the elderly?"

2.3 Systematic Searching Strategies

Systematic searching strategies used in this study involved three main processes: identification, screening, and eligibility.

2.3.1 Identification

Identification was done by searching all the synonyms and related terms for the main keywords used in this study, which were elderly, personalized food, and 3D printing. The purpose of this process was to enable more choices of related articles to be included in the review from the selected database. As shown by Shaffril et al. (2020a), the research questions were used as a basis to develop these keywords. Meanwhile, the online thesaurus (Merriam Webster), the keywords suggested in the thesaurus of Microsoft Word, and common keywords used by past studies were the sources used to conduct this identification process. Two main databases were used to search for the related articles: Scopus and ScienceDirect (Table 1). The existing keywords were successfully enriched by the authors by selecting several synonyms related to this study before developing a full search string (using Boolean operators and phrase searching) to be used in the main databases. Additionally, the authors also selected Google Scholar to be the supporting database. Whereas a developed search string was used for the prior two databases, the authors created several appropriate combinations of keywords to be searched in Google Scholar. These combinations of keywords included elderly, geriatric, "3D printing", "personalized food", "customized food", "customized nutrition", "customized diet", "personalized nutrition", and "personalized diet" by using Boolean operators (AND, OR) and phrase searching functions. Haddaway et al. (2015) propose that Google Scholar has several advantages for use as an additional database in a systematic review. A total of 219 articles were obtained from the searching process in the three selected databases: Scopus, ScienceDirect, and Google Scholar.

Table 1. Database Selected and Search String.

Database	Search string
Scopus	TITLE-ABS-KEY (("Elderly" OR "geriatric" OR "old folks") AND ("personalized food" OR "personalized nutrition" OR "customized food" OR "customized nutrition") AND ("3D printing" OR "3D food printing" OR "additive manufacturing"))
Science Direct	TITLE-ABS-KEY (("Elderly" OR "geriatric") AND ("personalized food" OR "personalized nutrition" OR "customized food" OR "customized nutrition" OR "Personalized diet" OR "customized diet") AND ("3D printing" OR "3D food printing" OR "additive manufacturing"))
Google Scholar	Elderly OR geriatric AND "3D printing" AND "personalized food" OR "customized food" OR "customized nutrition" OR "customized diet" OR "personalized nutrition" OR "personalized diet"

2.3.2. Screening

This study has set several inclusion and exclusion criteria to ease the process of article selection. The sorting function in each database sorted out all the 219 articles according to the inclusion and exclusion criteria (Table 2). The authors decided to review articles within a five-year period before the search was conducted, since it was impossible for them to review all the published articles available online, as corroborated by Okoli (2015). Furthermore, only English-based articles from 2016 until 2020 were included in this review to ease understanding. A total of 166 articles that did not meet the inclusion criteria were removed, and the remaining 53 articles were further screened for duplicates. Then, 11 duplicated articles were detected and removed, leaving 42 articles for the eligibility process.

Table 2. The Inclusion and Exclusion Criteria.

Criteria	Inclusion	Exclusion
Timeline	2016–2020	< 2016
Document type	Research article and thesis	Review article, conference, magazine, encyclopedias, books, chapter in books, book series, periodical, and others
Language	English	Non-english
Indexes	3D printing related to food printing	3D printing other than food printing

2.3.3. Eligibility

This process required the authors to retrieve all the published articles to be manually monitored so that the articles that were included in this review met the criteria. The eligibility process was carried out by going through the titles, abstracts, and conclusions of the retrieved articles. From this process, 27 articles were excluded due to the focus on ways to develop food models instead of using 3D printing for personalized food; focus on food presentation via 3D printing for children instead of the elderly; irrelevancy with 3D food printing; focus on 3D printing for nutraceutical delivery; focus on designing a 3D printer instead of designing food via 3D printing; focus on factors influencing 3D food printing instead of specifically on the characteristics of 3D food printing; focus on developing food equipment using 3D printers instead of developing food itself; focus on economic aspects of 3D food printers; focus on developing personalized food via other methods instead of via 3D food printing; focus on the development of systems to alter perception and illusions of 3D-printed food; and publication as thesis papers. As a result, only 15 articles remained to be reviewed.

2.4. Quality Appraisal

The quality appraisal was conducted to filter out low-quality articles from being included in this review. The remaining articles were assessed by reading all the articles thoroughly and executing the quality appraisal with the Critical Appraisal Skills Program (CASP) tool for systematic review. The authors modified several questions from the checklist accordingly to match the assessed research articles. The checklist was modified by omitting three out of ten questions, which were unrelated to the research articles. Only seven questions in the checklist were agreed to assess the quality of the articles' contents. The marks obtained from the checklist were categorized as follows: 1 to 2 marks as low quality, 3 to 5 marks as moderate quality, and 6 to 7 marks as high quality. Only moderate and high-quality articles were included in this review. The articles would be reviewed if there was a mutual agreement between all the three authors that the articles must at least be classified as moderate quality. Any disagreement on the rank of any article was discussed among the authors, and the third author was the decision-maker. From this process, the authors ranked 10 articles as high quality and five articles as moderate quality to be included in this review (Fig. 1).
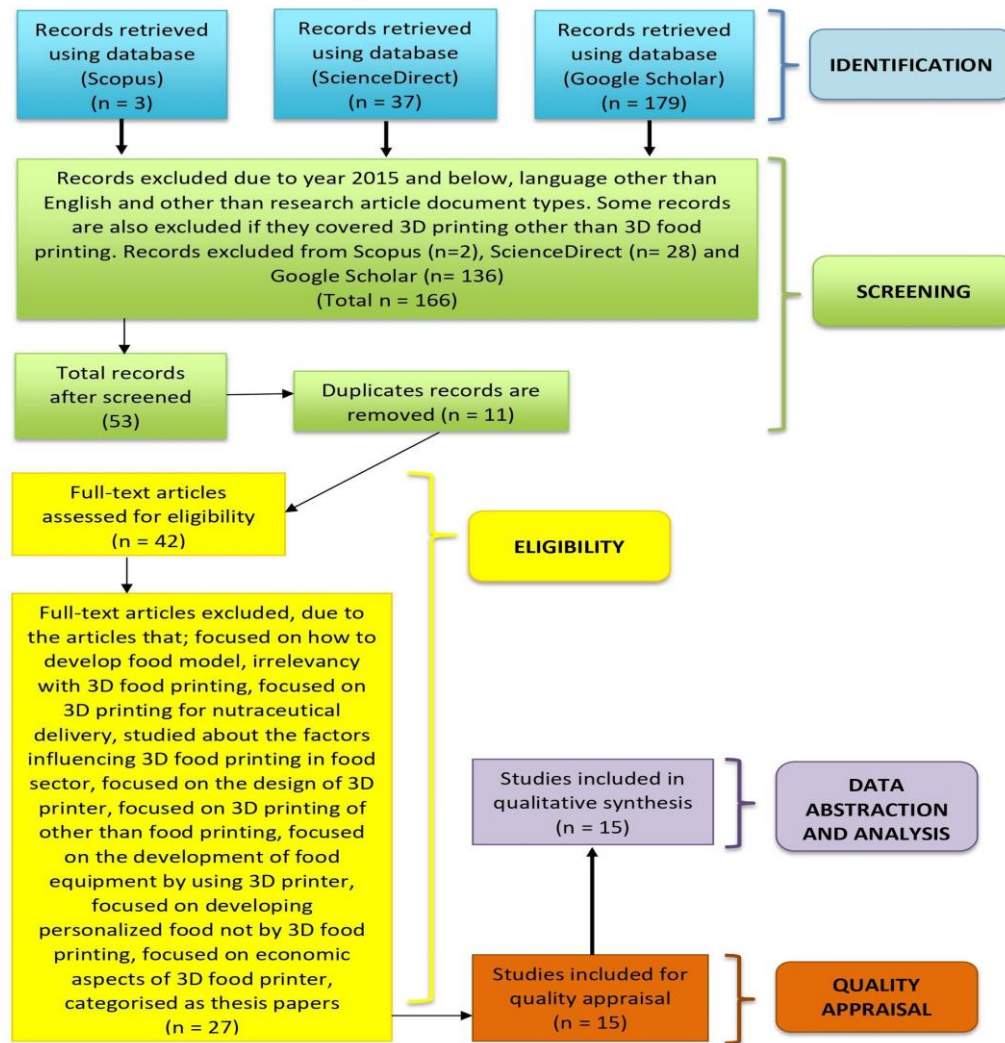
Figure 1. The Flow Diagram of Systematic Searching Strategies.

2.5 Data Abstraction and Analysis

This study used the qualitative synthesis technique. The entire 15 articles, especially the abstract, results, and discussion parts, were read thoroughly by the authors. The authors conducted data abstraction by abstracting any data from the included studies that could answer the research questions and was tabled. Then, the thematic analysis categorized all the data abstracted from all the reviewed articles into themes (Table 3). According to Shaffril et al. (2020b), the synthesis of data can be done either by qualitative synthesis, quantitative synthesis, or both. Thematic analysis is a part of qualitative synthesis that identifies important themes from the selected studies and groups them under the thematic headings (Braun & Clarke,

2006). According to Fleming et al. (2018), it is also the most suitable technique to synthesize a mixed research design, which started with the identification of similar patterns from all the selected studies and were grouped together. From this, seven main themes were discovered by the authors. Next, the accuracy of these themes was reviewed by all authors to ensure their suitability to present the data. The authors had excluded several themes unrelated to the research question, and the finalized themes were comprised of five main themes. The articles were divided among the authors for them to read, identify the patterns, and produce suitable themes. Afterward, the suitability of themes and the different interpretations of data were discussed until a mutual agreement was reached on the finalized themes.

Table 3. Data Abstraction Analysis of Reviewed Articles.

Study	Year	Food studied	Hardness	Viscosity	Moisture	Elasticity	Printability
Dankar *et al.*	2018	Potato Puree	/		/		/
Liu and Ciftci	2019	High-oil-content food pastes	/	/		/	/
Chen *et al.*	2018	Potato, rice and corn starches	/	/		/	/
Oyinloye and Yoon	2020	Mixture of pea protein and alginate	/	/		/	/
Derossi *et al.*	2020a	Cereal	/		/		/
Maniglia *et al.*	2019	Cassava starch		/	/		/
Dick *et al.*	2020	Pork	/	/	/	/	/
Huang *et al.*	2019	Brown rice	/	/		/	/
Zheng *et al.*	2019	Potato starch, corn starch, wheat starch	/	/	/	/	/
Derossi *et al.*	2020b	Cereal	/		/		/
Maniglia *et al.*	2020	Wheat starch	/	/			/
Jonkers *et al.*	2020	3D printed food with 50% native wheat starch, 40% maltodextrin, 10% palm oil powder				/	
Vieira *et al.*	2020	Cookies fortified with *Arthrospira platensis*	/	/	/	/	/
Liu *et al.*	2018	Milk protein incorporated with whey protein isolate (WPI)	/	/	/	/	/
Garcia-Segovia *et al.*	2020	Xanthan/Konjac gum		/		/	/

3. Results

3.1. Background of the Selected Articles

A total of 15 articles were obtained throughout the review process, and five themes were selected to be discussed: hardness, moisture, printability, viscosity, and elasticity. These themes were selected since they were emphasized and discussed deliberately in the studies. Furthermore, the themes affect the food structure to be tailored and consumed by the selected population. Hardness, printability, viscosity, and elasticity are crucial parts during the food extrusion and layering processes since inappropriate measures will result in failure. Meanwhile, moisture can affect all the other suggested parameters and primarily impact the shelf-life of the product. From the patient's acceptability perspective, hardness and elasticity must be within the acceptable range to be successfully printed and readily consumed by the elderly. From all the articles that were published in 2018 (3 journals), 2019 (4 journals) and 2020 (8 journals), the studies discussed the uses of potato puree, potato, rice, corn, wheat, cassava starch, cereals, pea protein, pork, and milk protein. They also included the effects of high oil content in food materials and biscuits incorporated with cyanobacteria.

3.2. Themes

The elderly population usually experience natural physiological changes as they age, such as swallowing difficulties (dysphagia) and reduced sensory perception that can lead to choking and aspiration. Texture-modified diets that consist of pureed, bite-sized, minced food and thickened fluids can help to reduce the risks of choking and aspiration in dysphagia patients (Dick et al., 2020). However, these foods are usually less appetizing to them (Dankar et al., 2018). Therefore, 3D printing allows the creation of food that resembles the original food but with modified textural properties (Dick et al., 2020).

3.2.1 Hardness

Most of the articles studied the hardness of different printed foods and the various parameters that affect it. Dankar et al. (2018) investigated the effects of extrusion parameters and additives on the specific mechanical energy (SME) of potato puree mixtures. They found out that SME was inversely proportional to the extrusion speed and that reducing the diameter of the hole also increased SME. Moreover, Huang et al. (2019) stated that the hardness of their printed sample was lowered significantly when the nozzle size, perimeter, and infill density were reduced. The smaller nozzle size produced a softer texture sample than the larger one. They also emphasized the benefits of controlling the infill levels to produce softer products that may be beneficial for elderly consumption.

Oyinloye and Yoon (2020) correlated the sample hardness with the ability of the materials to retain the shape and their extrusion characteristics after printing. They observed that increasing the concentration of pea-protein in their sample produced a harder printed product. Utilizing the combination of alginate and pea-protein as the basic material for 3D printing can positively improve texture, reduce hardness, and stabilize its shape. This was also supported by Dankar et al. (2018), who have shown that the SME increased with the addition of agar or alginate to potato puree. However, the SME decreased when the same concentration of lecithin or glycerol was added. Although potato puree, or a mixture of puree and glycerol or lecithin, created smoother extrusions, potato puree that was added with agar or alginate showed a more stable shape of extruded layers. Contrarily, the extrusion layers of potato puree alone and puree mixed with glycerol or lecithin easily collapsed and recombined post-extrusion (Dankar et al., 2018).

Besides that, Dick et al. (2020) also studied the effects of varying the concentration of two hydrocolloids – xanthan gum and guar gum – that were mixed with pork towards the formulation's texture profile after a post-processing heating. It was noted that the pork pastes without any added hydrocolloids were the hardest, followed by the formulation with only guar gum added. Addition of either one or both hydrocolloids result in a formulation with lower hardness compared to the sample without any hydrocolloids added (Dick et al., 2020). Vieira et al. (2020) developed functional cookie formulations that incorporated different forms of Arthrospira platensis. The cookie dough with the addition of A. platensis biomass was the hardest among all cookie formulations. In contrast, when the dough was incorporated with its free or encapsulated extract, these formulations showed a significant decrease in hardness compared to the control cookie dough without A. platensis.

The mechanical properties of the food pastes are reflected by their hardness (Liu & Ciftci, 2019; Zheng et al., 2019). Zheng et al. (2019) showed that their printed samples' hardness increased gradually with storage, specifically after 24 hours of storage. According to Liu and Ciftci (2019), the hardness of the high-oil-content food paste that they studied was affected by the ratio of starch more than the ratio of whey protein isolate (WPI). Liu et al. (2018) also reported that introducing WPI can soften the protein paste mixture, benefiting the extrusion and stability of deposited layers. Generally, a hard and rigid paste is formed from pure MPC powder, yielding a dry, rigid, and brittle extruded product compared to when it is mixed with WPI, which produces a

softer and flexible paste (a dose-dependent process) (Liu et al., 2018).

Meanwhile, Liu and Ciftci (2019) also reported that increasing the ratio of starch resulted in increasing gel strength. The same result was reported by Chen et al. (2018), in which higher starch concentration increased the yield stress (τy) and storage modulus (G') of samples, reflecting their mechanical strength. However, the flow stress (τf) also increased with increasing starch concentration, and if it was too high, it could affect the smooth extrusion of the starch samples (Chen et al., 2018). Zheng et al. (2019) also compared the addition of wheat, corn, and potato starches. They observed that wheat starch was the most suitable for 3D food printing. Most of the selected articles studied the effects of different proportions of materials and printing parameters on the hardness of printed products. Meanwhile, Maniglia et al. (2020) conducted research on the effects of dry heating treatment (DHT) on the improvement of wheat starch properties for 3D printing. They reported that increasing the DHT heating period could significantly increase the hardness of printed samples.

Derossi et al. (2020a) showed that the size and position of pores influenced the hardness of 3D printed snacks. Different hardnesses of 3D printed cereal snacks could be produced by modulating the position and number of pores. Thus, they suggested the potential of producing cereals with the desired mechanical properties to meet the specific requirements of the elderly. Lastly, Derossi et al. (2020b) compared the difference between 3D printed food and hand-made food. They observed that the layer-by-layer deposition of 3D printing had contributed to the increase in the hardness of printed food compared to hand-made ones. Moreover, 3D printed food had reduced pores that were bigger in size, leading to a denser food formula than hand-made food. This property made the 3D printed food harder than the traditionally hand-made food.

3.2.2 Moisture

Different kinds of materials incorporated into the sample have different abilities to hold or to prevent the binding of water molecules, thus adjusting the content can be made to meet the requirement. For the potato puree, the measured SME was reduced when it was incorporated with 1% lecithin or glycerol at 51.9 ± 2.1 and 52.0 ± 0.6 kJ.kg-1, respectively. In contrast, 1% alginate or agar would increase the hardness, with SME of 162.4 ± 10.1 and 217.0 ± 0.3 kJ.kg-1, respectively (Dankar et al., 2018).

Another type of starch-based ingredient used was cassava starch. The research was conducted by using DHT at 130°C against the starch component for 2 and 4 hours. This method was designed to maintain the moisture level below

10%. As the control sample contained 13.2% moisture content, the results after 2 hours and 4 hours were only 6.2% and 6.7%, respectively. Furthermore, the starch properties changed after the process. Consequently, maintaining the proper moisture content is crucial in producing a printable hydrogel (Maniglia et al., 2019). Similarly, in another study, wheat starch with longer DHT produced larger granules and lower moisture content (Maniglia et al., 2020). Zheng et al. (2019) discovered samples with wheat, potato, and corn starch as the main ingredients became harder with reduced springiness upon storage for 24 hours.

Derossi et al. (2020a) found that the 3D printed wheat-based cereal snacks having increased pores or honeycomb structure led to a greater moisture loss than the concentric structure upon baking. The smallest surface area of the sample showed changes in pore size and sample volume at -14.94 ± 9.1% and -9.56 ± 3.79%, respectively. Meanwhile, the largest surface areas showed changes of -26.92 ± 11.6% and -17.33 ± 0.67%, respectively. Negative volume denotes reduction in measurement. Another similar study using the same base ingredient showed different moisture content in the 3D printed cereals compared to the conventionally prepared ones (Derossi et al., 2020b). The results showed that the method for 3D food printing could produce an insignificant difference between the crumb and crust, which were 30g/100g and 15g/100g of water content, respectively.

Dick et al. (2020) reported that when the initial moisture content of meat was at 74.51 ± 0.05%, all the cooked samples in the paste form, either control or experimental, showed no difference in moisture content. All of them showed moisture content in the range of 76-77% (Dick et al., 2020). For biscuits incorporated with A. platensis, the moisture content was critical in suppressing the growth of bacteria or any other pathogens and to maintaining their crispiness. The successfully printed biscuits contained an average water activity (aw) of 0.3, low enough to maintain their crispiness and to suppress pathogenic activities (Vieira et al., 2020).

3.2.3 Viscosity

Liu and Ciftci (2019) discovered that storing paste at a low temperature (4°C) for a longer period of time improved viscosity. The 24-hour cooled paste had lower viscosity and a more stable shape of the printed product compared to the 2-hour storage. The results showed a similar trend to the ones observed by García-Segovia et al. (2020), in which the xanthan/konjac gum samples had reduced viscosity when the printing temperature was increased. In addition, by using different types of starch, Zheng et al. (2019) found that wheat and corn starch were less viscous and more thermally stable for the pasting process compared to potato starch. The viscous potato paste can possibly block the nozzle; thus, it needs adjustment for printing. Additionally, wheat starch

exhibited the greatest thermal resistance to viscosity breakdown under temperature exposure of 91.28°C. Moreover, DHT-treated cassava starch also displayed a reduction in its peak apparent viscosity with gel firmness, indicating that the treated samples were better than the native starch (Maniglia et al., 2019). In another study by Maniglia et al. (2020), the apparent viscosity dropped substantially as the period of DHT increased.

Chen et al. (2018) observed that at the same shear rate, increasing starch concentration directly increases its viscosity. Within the range of shear rate from 0.1 to 100 s-1, the viscosity of potato starch was the highest at a low concentration of 10%, while rice starch became the most viscous sample when the concentration was increased to 30%. As for synergistic effects between ingredients, Oyinloye and Yoon (2020) found that higher pea-protein content in the alginate samples yielded higher viscosity. However, the sample with 100% pea-protein displayed the lowest viscosity with increasing shear rate. Optimum viscosity was shown in a blending ratio of 80:20 between alginate and pea-protein and it was best suited for 3D printing (Oyinloye & Yoon, 2020).

Comparatively, shear rate is another vital factor that affects the viscosity of 3D printed products. In an opposite trend, the apparent viscosity of protein paste samples remarkably abates with the shear rate. Furthermore, rising WPI composition was shown to cause the same viscosity result (Liu et al., 2018). Huang et al. (2019) stated a similar trend for the viscosity of brown rice paste with escalating shear stress and shear rate. Dick et al. (2020) added that a decreased apparent viscosity was observed in pork samples mixed with xanthan and guar gum as the shear rate was high and closer to the extrusion step. The addition of hydrocolloid to the samples provided no significant effect to the apparent viscosity. Vieira et al. (2020) utilized the encapsulation method and obtained dough with a lower viscosity, while high viscosity was observed in biomass cookie dough.

3.2.4 Elasticity

The corn starch and WPI incorporated with oil, at any ratio of corn starch, water and canola oil in the study, constantly showed higher G' than G". The sample with reduced corn starch or WPI and increased canola oil resulted in a greater reduction of both G' and G". The result was also observed from the printed object, which could not withstand layering during the process. G' and G" could be increased with longer storage time. Reducing either starch or WPI would create a better print, but too low starch content would reduce the hardness of the product (Liu & Ciftci, 2019). For the study on brown rice, the researchers also stated that higher G' than G" contributed to the elasticity of the gel structure which could be beneficial for the extrusion process

(Huang et al., 2019). Rice starch showed the lowest tan δ (below 0.1), and a more consistent value was observed with a starch concentration of 15–30%.

Chen et al. (2018) found that the elasticity of all starches (corn, rice, potato) remained low under low temperatures until they reached a specific point called glass transition temperature (Tg), which ranged from 60–70 °C. At this point, G' and tan δ rapidly increase and decrease, respectively. Besides, potato starch showed the lowest Tg, which started at 60°C. The maximum glass transition state (TG'max) for potato, corn and rice starch was 71.2 ± 0.9°C, 73.2 ± 1.1°C and 84.4 ± 1.0°C, respectively. At TG'max, the concentration of potato, corn, and rice starch was 10%, 30%, and 10%, respectively. However, further heating resulted in a rapid reduction in the G' value for all samples. The G' value of corn and potato starch declined when exceeding 10°C from their Tg, while 20°C in the case of rice starch (Chen et al., 2018).

From a study conducted by Oyinloye and Yoon (2020), heating of all samples (pea-protein 100%, alginate 100%, alginate-to-pea-protein ratio of 90:10, 80:20, 70:30) with both heating rates (2°C/min, 5°C/min) showed increased G' and G" with G' constantly higher than G". Apart from that, the mixture of both ingredients showed higher G' and the highest G' was achieved with the 70:30 ratio using a 2°C/min heating rate. The increasing ratio of pea-protein increased the G', but the pea-protein and alginate alone showed lower G'. The G' value of 70:30 ratio was also the highest after the cooling process. All the samples showed a higher rate of increasing G' at 40–50°C (Oyinloye & Yoon, 2020).

Zheng et al. (2019) found that the samples of wheat and potato starch were more elastic than corn starch after being stored for 6 hours. After 24 hours, potato starch had slightly higher springiness compared to the others. However, corn starch constantly increased in springiness after a longer storage period. A study on a brittle sample of 50% wheat starch incorporated with maltodextrin (40%) and palm oil (10%) was conducted to characterize and measure plasticity and elasticity behavior. Elasticity was measured to differentiate it from plasticity by measuring the tension and compression when the model was compressed, showing the values of 1.0 MPa and -0.73, respectively. Moreover, the plastic deformation also resulted in a shear rate value of 1.0*10-3 s-1 (Jonkers et al., 2020).

In a test of 3D printed cookies incorporated with different preparations of A. platensis, Vieira et al. (2020) stated that all samples (control, biomass, free extract, and encapsulated extract) showed a tan δ value lower than 1 for all the temperatures tested. Besides that, the biomass-containing dough exhibited greater elasticity. This result was in contrast with the encapsulated extract. Elasticity decreases with increasing temperature after 40°C and remains constant

until 105–110°C. Above this temperature, the elasticity profile rose again until it reached 120°C. The encapsulated sample had the lowest Tg (90°C), TG'max (110°C), and G', while the biomass sample had the highest Tg (100°C), TG'max (120°C), and G'. Changes in elasticity parameters were similar for all types of samples (Vieira et al., 2020).

Pure MPC cannot be used for 3D printing because it does not have enough elastic semi-solid properties. Liu et al. (2018) prepared a few samples with different mixtures of MPC and WPI. They discovered that increasing the WPI ratio reduces G' in all samples. Adding one part of WPI to six parts of MPC greatly reduced tan δ. It showed that an MPC to WPI ratio of 4:3 had the highest G' and the lowest tan δ value (Liu et al., 2018). For the study which used the mixture of xanthan and konjac gum as the base, they found that the G' was more affected than the G" in respect to the printing temperature. For a mixture that has a melting temperature at 45°C, the lower printing temperature (25°C) resulted in greater G' (1006–1528 Pa) compared to the higher temperature, 50°C (390–644 Pa). The G' also be increased by reducing and increasing the concentration of syrup and gum, respectively. Moreover, the xanthan and konjac gum ratios played an important role in determining the elasticity, with the sample ratio of 2:1 showing the highest G' compared to the other ratios (Garcia-Segovia et al., 2020).

3.2.5.   Printability

A lot of foods are printable with suitable modifications of certain parameters. According to Dankar et al. (2018), the best printability of potato puree is achievable with a 0.5 cm nozzle height and a 4 mm nozzle diameter with a range of alginate concentration of between 0.5% and 1.5% and an agar concentration of between 0.5% and 1%. Similarly, Huang et al. (2019) also showed that a smaller nozzle size improved their food samples' printability.

Liu and Ciftci (2019) studied the relationship of paste composition and paste conditioning with the printability of food. Higher WPI content negatively affected the printability, while 24 hours of storage of the pastes at 4 °C improved the printability. However, Liu et al. (2018) showed different results. Their results showed that increasing WPI concentration had improved the printing performance of protein pastes. The best formulation for the successful printing of protein paste was the paste with an MPC to WPC ratio of 5:2. Besides, Chen et al. (2018) studied the influence of the rheological properties of corn, potato, and rice starch on their 3D printing performance. They proved that rice starch of 15% to 25% (w/w) concentrations at 80°C, corn starch of 20% to 25% (w/w) concentrations at 75°C and potato starch of 15% to 20% (w/w) concentrations at 70°C had the appropriate τf, τy, and G' values for excellent printability, shape stability and resolution. Zheng et al.

(2019) also approved the suitability of all starch gels in 3D printing, with wheat starch showing the closest dimension to the actual model.

Derossi et al. (2020a) believed that 3D printed cereal-based snacks with different hardness could be created via the modulation of position and number of pores. Derossi et al. (2020b) observed that the 3D printed food exhibited higher hardness, chewiness, and cohesiveness compared to the hand-made samples. Furthermore, Vieira et al. (2020) agreed on the potential of 3D printing technology as a great alternative to create cookies and other novel functional foods that can be incorporated with antioxidants, such as microalgae.

Besides that, Oyinloye and Yoon (2020) studied the different blends of alginate and pea-protein. They showed that the 100% alginate and 100% pea-protein samples might not be suitable for 3D printing. Some studies added hydrocolloid to improve the printability of food materials (Dick et al., 2020; Garcia-Segovia et al., 2020). Dick et al. (2020) examined the effects of adding xanthan gum and guar gum, either as individual components or in combination, on the printability of pork pastes. All the samples showed a shear-thinning effect, implying their suitability for 3D-extrusion printing. This suggests their possibility of becoming one of the transitional foods for people with swallowing problems (Dick et al., 2020). Meanwhile, Garcia-Segovia et al. (2020) observed that mixtures with higher xanthan gum and konjac gum content and a lower concentration of syrup exhibited greater values of G', G", and η*. Increased syrup concentration led to the reduction of Fmean, area, Fmax, and slope gradient.

Maniglia et al. (2019) evaluated the effects of DHT on the printability of hydrogels based on cassava starch. They concluded that DHT-treated starches, especially those that were treated for 4 hours, produced gels with better printability compared to native starch (Maniglia et al., 2019). Similarly, in their other work, Maniglia et al. (2020) observed that the best printability and better reproducibility were shown by the hydrogels treated with DHT for 4 h compared to 2 h at 130°C.

4.   Discussion

Elderly people may require different nutritional requirements than normal people, which is often due to swallowing problems (dysphagia), which require specialized nutritious meals. Thus, 3D food printing could be one of solution to addressing the problems faced by the elderly by printing a suitable personalized food for them. Based on the thematic analysis, there are five parameters that can be modified to represent the research themes: hardness,

moisture, viscosity, elasticity, and printability. This section will further discuss the themes (Table 4).

4.1 Hardness

Hardness is one of the important themes since it is related to the swallowing problems among the elderly. The hardness of printed samples can be controlled via printing parameters, such as nozzle diameter, infill density, and perimeters (Huang et al., 2019). The diameter of extrusion lines is determined by the nozzle size, while perimeters refer to the amount of layer at the outer part of the printed samples, and infill density refers to the solid proportion in the inner part of the printed samples. When using a 3D slicer to slice the designed food, more layers are sliced with the use of a smaller nozzle. Consequently, this helps to improve the texture of the printed materials (Huang et al., 2019). The SME of the sample can also be decreased with a smaller diameter hole. It will create more friction that leads to a higher applied force needed to extrude the samples (Dankar et al., 2018). Thus, reducing the nozzle diameter, infill density, and perimeters can help to reduce the hardness of the printed samples.

A combination of 80% alginate solution and 20% pea-protein solution as the printing material can create a softer texture food. This is due to their ability to increase the gel strength, which is caused by the calcium release from the alginate gel that can induce the coagulation of aggregated proteins (Oyinloye & Yoon, 2020). Dankar et al. (2018) showed that a lower SME was recorded in the potato puree mixed with lecithin or glycerol compared to the addition of alginate or agar. This is because of the moisture retention ability of lecithin or glycerol that can disrupt the starch granules' internal microstructure, thus softening the material. However, potato puree mixed with alginate or agar is preferred because it can retain the stability of shape after printing better than the mixture with glycerol or lecithin. Even though the mixture with glycerol or lecithin was smoother, its extruded layers collapsed after printing (Dankar et al. 2018).

Adding hydrocolloids can also produce a transitional food that is useful in addressing the swallowing problems faced by the elderly (Dick et al., 2020). It was reported that the ideal ratio of hydrocolloids in the pork pastes was the formulation with a xanthan to guar gum ratio of 70:30. This formulation is more flexible, presenting a less compact microstructure than the pork pastes without hydrocolloids. The less elastic formulation contributes to a higher hardness texture due to a more compact microstructure as seen in the pork pastes without hydrocolloids (Dick et al., 2020). Food thickeners, such as starch and xanthan gum, can act as rheology modifiers in food printing to improve the food materials to be printed (Huang et al., 2019).

Table 4. Summary of Article Findings.

Themes	Hardness	Moisture	Viscosity	Elasticity	Printability
Dankar et al. (2018)	- SME is inversely proportional to extrusion speed, in such a way that the SME decreases with increasing extrusion speed. - Reducing the diameter hole also increases SME.	- The use of water-binding agent increases moisture content, thus softens the starch-based puree. - The use of hydrocolloid increases molecular bonding, thus increasing the puree hardness.	Not discussed.	Not discussed.	A mixture of potato purees with a specific concentration range of agar or alginate can produce a more stable printed product that can retain their shape longer without deforming.
Liu and Ciftci (2019)	- The hardness of food pastes increases with or without storage when there is an increase in the total mass. - Reducing WPI ratio leads to a smoother printed pastes' surface and since they do not spread, the printed shape can be retained well. - Increasing the ratio of starch results in increasing gel strength.	Not discussed.	Increasing total mass, shear rate and storage period within 24 hours improves product viscosity.	Elasticity was increased with increasing percentage of corn starch used and longer storage period.	- Reducing starch or WPI concentration improves the printability of the hexa shape while reducing the starch content to print vase-shaped paste results in poor printability. - Starch acts as a thickening agent and plays a vital role in maintaining the height and weight of the vase-shaped paste.
Chen et al. (2018)	Higher starch concentration will increase the yield stress (τy) and storage modulus (G') of samples, which also reflects their mechanical strength.	Not discussed.	Within constant shear rates, the viscosity rises as the concentration increases.	Rice starch has good thermal stability, and it does not lose its elastic properties in wide range of temperature during printing process.	Starches' shear-thinning and strain-responsiveness behaviour make them suitable for and printable as 3D printing food materials.
Oyinloye and Yoon (2020)	- Increasing the concentration of pea-protein produces a harder printed product. - Combination of alginate and pea-protein as the basic material for 3D printing is beneficial to produce a sample with good texture and reduced hardness while stabilizing its shape.	Not discussed.	An optimum result of easy extrusion was found in a blending ratio of 80:20 (alginate to pea protein).	- Elasticity of pea-protein based food can be increased by using higher amount of pea-protein and slower heating rate. - The best model should have gelation temperature nearly similar to extrusion temperature.	A mixture of pea protein and alginate shows stable thermal properties and no endothermic peak is detected at lower temperature, indicating that the nutritional compositions in the mixture are well-preserved at the extrusion temperature, 45°C.

Derossi et al. (2020a)	- Different hardness of 3D printed cereal snacks can be produced by modulating the position and number of pores. - Cereals with desired mechanical properties can be produced to meet the specific requirements of certain populations such as the elderly people.	Increasing surface area will increase evaporation rate, which will make the sample lose moisture faster.	Not discussed.	Not discussed.	- Printed snacks are smaller than the virtual model, which may be caused by dehydration during the baking process. - There are additional pores developed throughout the dough deposition and baking, which resulting in higher porosity fraction in the printed sample.
Maniglia et al. (2019)	Not discussed.	Pre-treatment of sample with DHT greatly reduces the moisture content of the sample.	The product apparent viscosities drop when the treatment period increases. However, it must be altered at a level that is easy for extrusion.	Not discussed.	- DHT for 4 hours has produced the best printability compared to DHT for 2 hours at the temperature of 130°C. - DHT-treated starches are also presented with lower water absorption index (WAI).
Dick et al. (2020)	Addition of hydrocolloids to samples, either on its own or in combination, can create a formulation with lower hardness compared to the sample without any hydrocolloids added.	Hydrocolloid does not affect moisture content.	Overall, there are no changes in the apparent viscosity upon the addition of hydrocolloids.	Not discussed.	Adding samples with hydrocolloids, either in combination or on its own has shown an admirable textural and rheological properties of the end-products.
Huang et al. (2019)	- Hardness of their printed sample is lowered significantly when the nozzle size, perimeters and infill density are reduced. - Control the infill levels to produce softer products that may be beneficial for elderly consumption or people with mastication problems.	Not discussed.	Elevating both shear stress and shear rate leads to reduced viscosity of the brown rice paste.	Higher G' and lower G" indicate good elastic properties of sample	- Printing precision is significantly affected by the nozzle size due to the influence of gravity towards the deposition of extruded lines. - Smaller nozzle size minimizes the deviation in the dimensional properties of their samples.
Zheng et al. (2019)	- Printed samples' hardness increases gradually with storage, specifically after 24 hours of storage. - Wheat starch is the most suitable for 3D food printing.	- Lower moisture content will reduce springiness of the sample. - Wheat starch can hold the highest amount of water molecules.	Each species of the starches exhibits different level of viscosity. Moreover, higher viscosity would make extrusion more difficult during 3D printing.	Elasticity or springiness will reduce with extended storage period of the sample.	Wheat starch gel is the most suitable starch to be used as 3D food printing materials due to lowest viscosity, better extrusion ability and excellent storage properties.

Derossi et al. (2020b)	- Layer-by-layer deposition of 3D printing has contributed to the increase in hardness of printed food compared to the hand-made ones.	With specifically similar method used, the sample with the same amount of moisture is reproducible.	Not discussed.	Not discussed.	The samples' microstructures vary in 3D samples, affecting their mechanical properties and resulting in less favourable textures compared to the hand-made samples.
Maniglia et al. (2020)	Increasing DHT heating period can significantly increase the hardness of printed samples.	Reducing moisture content without changing the physical properties can be done by using low temperature DHT with longer period.	Long period of DHT reduces apparent viscosity significantly.	Not discussed.	Yield stress of DHT-treated starch increases with increasing DHT time, which is an important characteristic of the food material to retain its shape under gravity and stresses from the deposited layers. - Syneresis is also reduced when the wheat starch is modified with DHT.
Jonkers et al. (2020)	Not discussed.	Not discussed.	Not discussed.	For 3D food printing, its elastic properties do not relate to plasticity.	Not discussed.
Vieira et al. (2020)	- Cookie formulations incorporated with addition of A. platensis biomass is the hardest among all cookie formulations. - Dough that is incorporated with A. platensis free extract or A. platensis encapsulated extract showed a significant decrease in hardness compared to the control cookie dough without A. platensis.	The method used by the researchers can produce a cookie with aw level as low as 0.3. This moisture level is low enough to suppress any growth of microbes.	Dough containing antioxidant extract has unstructured network that leads to reduced viscosity, which consequently lowers its resistance to deformation.	- The sample exhibits gel-like material when tan δ < 1. - Sample incorporated with biomass extract shows the highest elastic properties and the most heat stability since it has the highest TG'max.	By using a diameter close to the opening of the nozzle, all the formulation present consistent dimensional properties post-deposition. - Using the antioxidant extract in encapsulated form is preferable to improve the stability of 3D printed cookies towards different environments.

Liu et al. (2018)	- Using pure MPC alone is too hard to be extruded from the nozzle, thus yielding a dry, rigid and brittle extruded product. - The ideal ratio of MPC to WPI is 5:2. This mixture is easily extruded from the nozzle and it successfully maintains its shape post-extrusion.	Not discussed.	The addition of WPI lowers the apparent viscosity and it is prepared at ratio of 5:2 (MPC/WPI), providing mechanical strength for deposition and adhesion.	MPC to WPI ratio of 5:2 shows the best elastic properties which enable the sample to be printed and layered properly without affecting its confirmation.	- Increasing WPI concentration helps to improve printing performance of protein pastes. - However, increasing too much WPI concentration can result in a protein paste possessing weaker mechanical strength, which can lead to collapse.
Garcia-Segovia et al. (2020)	Not discussed.	Not discussed.	Viscosity serves as a parameter to study rheological and viscoelastic behaviour.	- Higher gum percentage results in greater elasticity. - The printing temperature that is higher than its melting point will reduce elasticity and increase flowability.	- Increasing concentration of xanthan gum and konjac gum and lowering the concentration of syrup lead to higher values of G', G", and η*, influencing textural properties.

82

Liu and Ciftci (2019) observed that the gel strength could be increased by increasing the starch concentration. There is a higher number of starch molecules per unit volume when the starch concentration is increased. This increases the possibility of more intermolecular hydrogen bonding, resulting in a more compact structure that can increase the gel strength. Furthermore, it is recommended that the printing paste be stored at a cold temperature (4°C) to incorporate more oils into the paste. Higher mechanical and gel strength are noted with increasing storage time, providing shape stability of the printed paste after extrusion (Liu & Ciftci, 2019). However, Zheng et al. (2019) showed that their printed samples' hardness increased after 24 hours of storage, possibly due to the higher likelihood of getting dehydrated after cold storage.

Besides that, Liu et al. (2018) suggested the addition of WPI to soften protein pastes. The higher proportion of WPI contributes to a significant reduction in the hardness of protein pastes, as reflected by the alternating interactions shown by the macromolecules of the protein and other small molecules. However, a further increase in WPI proportion will create a smoother texture but with lower shape fidelity (Liu et al., 2018). Reducing relative density is also crucial to lowering the hardness of printing samples, which is also related to porosity, as portrayed by Derossi et al. (2020a). Derossi et al. (2020b) reported that 3D printed food exhibited lower and bigger-sized pores compared to hand-made food, which is may be due to the imbalanced printing conditions.

4.2 Moisture

Moisture content is an important characteristic to be addressed because it can affect various properties of the product, including the extrusion or post-extrusion process. Moisture content may affect the hardness of extruded materials (Dankar et al., 2018), printability (Maniglia et al., 2019), springiness (Zheng et al., 2019), crispiness, and bacterial stability (Vieira et al., 2020). Besides that, moisture content can be affected by the surface area of the printed object (Derossi et al., 2020a). Dankar et al. (2018) revealed that the incorporation of lecithin and glycerol could reduce the SME of the puree. Both lecithin and glycerol can bind with water molecules, reducing the microstructural integrity of starches, and thus, making it softer. In contrast, when incorporating alginate and agar of the same percentage, the material becomes harder since its hydrocolloid properties cause the formation of random, multiple, and continuous bonds with starch molecules. Although alginate has a lower SME compared to puree alone, the shape of the extruded product has better integrity and shape. Consequently, adding alginate softens the materials while, at the same time, increasing their integrity.

Proper moisture content is also important for the printability of materials. The use of DHT before the extrusion process significantly affects the moisture properties of materials after being printed (Maniglia et al., 2019). The longer the period of starch under DHT, the lower the moisture content due to vaporization. The starch properties have also been observed to change, with the granules becoming larger upon DHT. However, using a lower temperature while targeting for a similar moisture content resulted in no changes in granule size, indicating that high temperature is responsible for the properties change (Maniglia et al., 2019; Maniglia et al., 2020). Thus, to maintain the starch properties, a lower temperature can be used while increasing the duration of process. Apart from that, the springiness of the object can be related to moisture content, with lower moisture contributing to less springiness (Zheng et al., 2019). Wheat starch had been shown to hold water molecules better upon storage up to six hours, but it greatly declines after 24 hours. Consequently, the loss of springiness can be attributed to the dehydration during storage. Therefore, observations need to be conducted at a shorter interval, especially on the 12th hour, to identify if wheat starch can hold water molecules for an intermediate storage period.

Derossi et al. (2020a) created a 3D printed food model with a similar size but different numbers of pores. Increasing pore numbers will proportionally increase the surface area. In turn, the increased surface area will significantly increase the evaporation rate, thus greatly reducing the moisture content. Therefore, the honeycomb structure has greater pore size and sample volume reduction upon baking compared to the concentric structure (Derossi et al., 2020a). The study conducted by Derossi et al. (2020b) concluded that a 3D food printing method could produce the same water content in the same snacks made with the same basis if they were processed specifically according to the author's research.

Hydrocolloid is used to increase water dispersion throughout the matrix. Hydrocolloids have been indicated to not affect the moisture content of the matrix since the control sample, incorporated by single or both hydrocolloids, has not changed the moisture content upon heating. However, the incorporation of both hydrocolloid guar gum and xanthan gum improved the pork paste texture, enabling it to be consumed by dysphagia patients (Dick et al., 2020). Although hydrocolloids do not significantly affect moisture content, their incorporation can improve the texture. The chewiness of pork pastes alone reached 37.19 ± 2.13 N, while incorporating xanthan gum and guar gum at a ratio of 1:1, 7:3 and 3:7 had significantly reduced the chewiness (Dick et al., 2020). This result can be achieved by using a higher guar

gum percentage than xanthan gum since it is cheaper and it offers nearly similar textural properties.

In the study of microbial growth in the food manufacturing process, aw is a crucial factor to be monitored to prevent growth (Vieira et al., 2020). The aw is a measure of water molecules that participate in enzymatical, chemical, or biological reactions. The study stated that the suppression of bacterial and mold or yeast activities would be suppressed if aw was below 0.8 and 0.6, respectively. The 3D printed biscuit managed to maintain a low aw, which was below 0.3 even after being stored for 30 days. Therefore, 3D food printing can produce a microbiologically stable product as well as maintain its crispiness (Vieira et al., 2020).

4.3 Viscosity

Liu and Ciftci (2019) mentioned that low water content can reduce viscosity and gel strength as it limits the starch swelling ability and amylose leaching. The gel that was made up of corn starch and WPI required a low amount of water to allow smooth flowability through a small diameter nozzle. The viscosity level must be below the extrusion pressure before being printed into a paste. Upon being stored for 24 hours, the viscosity was observed to increase slightly, yielding a better paste shape.

The behavior of viscosity can also be impacted by shear rate as adopted by the non-Newtonian fluid with shear-thinning properties that vary according to the nature of the material. For example, elevations in both shear stress and shear rate lower the viscosity of brown rice paste (Huang et al., 2019). Chen et al. (2018) added that all starch samples fell under a similar category. Utilizing starch from corn, rice, and potatoes, increasing its concentration improves the viscosity, although the same shear rates are applied. Moreover, the peak viscosity is different for each material depending on their concentration. In the shear rate ranged from 0.1 till 100 s−1, potato starch reached the highest viscosity value at concentrations of ≤ 10% (w/w) while the peak viscosity of rice starches required 15 to 30% (w/w) (Chen et al., 2018).

Dick et al. (2020) observed that a similar relationship between viscosity and shear rate existed in cooked pork paste. However, the utilization of hydrocolloids in the pork paste samples did not yield any significant effect on the apparent viscosity except for the control sample. The hydrocolloids affected the stability of the sample matrix, resulting in reduced apparent viscosity. The peak viscosity refers to the maximum ability of a material to retain its structure while swelling during the gelatinization process. To be precise, the resistance is observed as the starch granules swell before disintegration (Gou et al., 2019).

In a study related to protein, Liu et al. (2018) highlighted that viscosity affected the extrusion process. Successful printing requires a certain correct ratio of specific materials used to produce the right viscosity. For instance, MPC and WPI were combined in a 5:2 ratio to provide adequate mechanical strength for layer deposition and adhesion. Besides, the WPI particles react to water molecules, reducing the apparent viscosity and easing the extrusion of protein pastes. The viscosity had remained low during the process to improve flowability and became high after the process to allow adherence of the printed layers between one another. The observation was corroborated by Liu and Ciftci (2019) and Garcia-Segovia et al. (2020). Conversely, products with high viscosity will stick on the wall and block the nozzle that will lead to inaccurate shape of the printed product (Oyinloye and Yoon, 2020; Zheng et al., 2019). Garcia-Segovia et al. (2020) observed that the product's viscosity is enhanced by decreasing the ratio of syrup while increasing the ratio of both materials.

Meanwhile, Zheng et al. (2019) found that wheat starch gel has the lowest viscosity, better extrudability, and better storage properties but low thermal stability compared to corn starch. This is due to the granule size and shape. Besides, Oyinloye and Yoon (2020) found that increasing the percentage of pea-protein in the sample mixed with alginate resulted in greater viscosity due to the hydrophilic nature of pea-protein that absorbs moisture. The result was similar when the pea-protein was exposed to a higher temperature. However, the 100% pea-protein sample recorded the lowest viscosity. After applying a high temperature of 40°C, the sample turned into a gel with a high viscosity, but it was not favorable for 3D printing. Hence, the blending ratio of alginate to pea-protein for 3D printing was set optimally at 4:1.

Besides, some studies have utilized DHT to alter the product viscosity and firmness. The molecular and granular structures of the sample are modified based on the temperature and the treatment storage time. A cassava starch sample appeared to be the strongest gels with the least peak apparent viscosity under all the evaluated conditions after being treated at 130°C for 2 and 4 hours (Maniglia et al., 2019). Maniglia et al. (2020) further explained that DHT lowered the peak apparent viscosity by cleaving the glycosidic linkage between the starch particles, a process known as depolymerization. This process weakens the granules and diminishes their integrity through thermal degradation of the crystalline structures. Longer treatment time is associated with greater reduction of the peak apparent viscosity.

4.4. Elasticity

The matrix should exhibit pseudoplastic and shear-thinning behavior to ease the printing process. It should also ideally be able to withstand its own weight upon completing the process. Plus, thermoelastic value analysis helps to form good layering during the printing process (Oyinloye & Yoon, 2020). This value can be measured by the mechanical strength, where a higher value shows the ability to retain its structure. Higher G' with lower G" indicates the high elastic property of the matrix and it will have a gel or gel-like behavior (Huang et al., 2019; Liu & Ciftci, 2019). Besides that, Chen et al. (2018) stated that tan δ < 0.2 might indicate good elasticity property.

Liu and Cifti (2019) reported that all the samples showed G' is higher than G", indicating a matrix with gel-like properties. On the other hand, a reduction in corn starch percentage in the sample reduces elasticity. Corn starch acts as the water-binding agent, forming a crosslinking of the gel that strengthens the bond. Reducing corn starch can reduce the bond formation, thus reducing elasticity and vice versa. Storage time can also increase G' and G" due to more time being allowed for the agent to form more bonds (Liu & Ciftci, 2019).

The study on the effects of temperature on starch elasticity showed that at a specific level (Tg), the elasticity would rapidly increase as denoted by the rapid incline of G' and the decline of tan δ. The researchers stated that a good elastic starch suspension will have G' > 500 Pa and tan δ < 0.2 upon increasing the temperature. Tan δ is the measurement of its elasticity, with lower values indicating a greater ability to withstand plastic deformation. At Tg, the starch granules start to swell and form interactions with other ingredients. TG'max is the temperature when the sample has the highest elasticity value. Further temperature rises reduce G', indicating that the starch molecules start to degenerate and break their molecular interaction (Chen et al., 2018). Rice starch offers the widest range of Tg compared to other starches used, indicating that it has better thermal stability. The concentration of starches used does not correlate with TG'max, thus further research needs to be conducted to determine the absolute cause.

In the study conducted on alginate and pea-protein, the elastic properties were different due to the interaction between the two materials with respect to heating. Through heating, the mixture shows an increase in G' with an increasing ratio of pea-protein. The calcium ions of alginate react with the protein molecule to enhance the covalent bond, thus describing the change in elastic properties as it behaves as a gel. The rate of heating can also affect the G' value. A slower heating rate (2°C/min) resulted in greater G' compared to a higher heating rate (5°C). A longer period

allows the protein molecules to rearrange and create a more structured network. Increasing the pea protein-to-alginate ratio can yield stronger bonds, thus resulting in a higher G' compared to pea-protein and alginate alone. Apart from that, all the samples' Tg ranged from 40 to 50°C due to the higher increase in the rate of G' in this range. Due to the increased elasticity, a too low gelation temperature will increase the pressure required during extrusion. Therefore, the pea-protein amount needs to be adjusted so that it reaches a gelation temperature nearly similar to the extrusion temperature, which is 45°C (Oyinloye & Yoon, 2020).

Elasticity can also be measured through the springiness of the mixture. Springiness is determined by the water content; more water escape results in a less elastic, hard, and compact structure. The study showed that the samples incorporated with potato and wheat starch were highly elastic in the 6th h but reduced after the 24th h (Zheng et al., 2019), indicated that the water started to leave the samples 6 h later. Thus, this mixture can be produced due to its high elasticity, but it cannot be stored for a long period of time. Apart from that, the base that uses corn starch can be stored for a longer period since its elasticity does not deteriorate after 24 h, but it is naturally harder and less elastic from the beginning.

Through stress-strain tests on several brittle models with different geometries, Jonkers et al. (2020) observed that the plasticity did not correlate to elasticity. This is because plasticity is measured through the macroscopic stress-strain response, showing signs of deformation before a fracture stress is reached. The sample's plasticity, measured as shear rate, was $1.0 \times 10^{-3} s^{-1}$ while the elasticity was so small and insignificant that both did not correspond to each other (Jonkers et al., 2020). Thus, the studied model showed that the elasticity of the brittle model did not correspond to plasticity. With the sample having a tan δ lower than 1, all the cookie dough exhibited a gel-like property (Vieira et al., 2020). The dough that uses biomass had the largest G' because its free composition created more networks with other materials in the dough. Compared to encapsulated extract, their content was trapped, and consequently no additional or strengthening of the bond could be created. All samples decreased in elasticity upon reaching 40°C due to the melting of butter used during the preparation of the dough. The biomass also indicated that it was the most heat stable compared to other preparations due to the highest TG'max. The reduced elasticity profile after such a temperature indicates that the bond starts to break because of molecular deterioration (Vieira et al., 2020).

The pure form of MPC is stiff and cannot behave as a semi-solid. Since it needs a very high extrusion force, it cannot be a candidate to be used in 3D printing. However,

the incorporation of WPI manages to reduce its G' value, allowing it to behave as a viscoelastic material. WPI can hold water particles, incorporating them together with the sample. Increasing the water content will soften the materials, reducing their G' from their original sturdy state. However, excessive WPI will greatly reduce G' due to excess water content, making the mixture too soft, less elastic and exhibiting high flowability. The 4:3 ratio of MPC to WPI has been shown to have the lowest G' and highest tan δ. However, in this condition, the mixtures were too soft, showing failure in the layering process. Thus, the best MPC-to-WPI ratio to produce a suitable elastic material for smooth extrusion and good layer adhesion while withstanding external pressure is 5:2 (Liu et al., 2018). Consequently, very high G' and very low tan δ are bad for elasticity and printing process.

Garcia-Segovia et al. (2020) studied the effects of printing temperature on the elasticity of gel material using xanthan and konjac gum. The xanthan gum used has a melting point of 30–45°C. When the printing temperature is higher than the melting point, the elastic property of a gel is reduced. This observation correlated with the test since 50°C printing temperature resulted in a significantly lower G' compared to 25°C (Garcia-Segovia et al., 2020). Increasing the gum concentration also increases the G' or elasticity, since the gum itself contributes to the elastic properties of the mixture. Consequently, printing at a higher temperature than the melting point of substances can greatly reduce elasticity and increase flowability due to the melted samples (Garcia-Segovia et al., 2020). Besides that, the correct proportion of gel materials is necessary to produce good elastic properties during printing.

4.5. Printability

The 3D food printing technology has some limitations in building the 3D structure of the food and retaining the shape of the printed food post-printing. The composition of the food ink to be printed and the printing parameters of the 3D food printers highly affect the performance of the end products (Çakmak & Gümüş, 2020). Therefore, all the reviewed studies have focused on achieving good printability of food materials by modulating certain parameters that can affect the texture and rheology of the studied food. Before concluding that the ideal nozzle height was 0.5 cm, Dankar et al. (2018) tested the effect of a ≥ 1 cm nozzle height and irregular material flow. Irregular material flow was caused by the delayed deposition, which led to brittle extrusion layers. The surface roughness and precision of the samples were also affected by the nozzle diameter (Dankar et al., 2018).

Huang et al. (2019) reported that smaller nozzle size could improve 3D food printing precision. Printing precision was significantly affected by the nozzle size due to the

influence of gravity on the deposition of extruded lines throughout the printing process. They concluded that smaller nozzle size should be used to greatly minimize the deviation in the dimensional properties of their samples. The type of substrate is also crucial during the printing process. Dankar et al. (2018) concluded that the mixture of potato purees with a specific range of agar or alginate concentration could produce a more stable printed product that could retain its shape longer without deformation. This is possibly due to the higher internal strength and higher SME shown by the formulation incorporated with agar or alginate. Thus, they suggested the possibility of substituting unappealing meals for people with swallowing difficulties by developing foods in a more innovative way.

Liu and Ciftci (2019) observed a negative effect of increasing WPI concentration on their samples' printability. WPI acts as a water and liquid oil emulsifier, which is co-applied with starch, a thickening agent. Successful printing also depends on the optimum weight of the pastes. Consequently, reducing starch or WPI concentration improves the printability of the hexa shape while reducing the starch content to print vase-shaped paste, results in poor printability. This is because the starch acts as a thickening agent and maintains the height and weight of the vase-shaped paste. The gel strength has been observed to increase with reduced starch content, but due to the absence of sufficient thickening agent, the end-product collapsed after printing (Liu & Ciftci, 2019). Besides that, 24 h of storage at 4°C has improved the printability of the pastes by increasing the gel strength. However, the gelation time and swelling are different with different gelling agents (Kim et al., 2018). Gelling agents that reduce the gel strength of the printed pastes during storage are not suitable to be used in 3D food printing since this technology needs consistent rheological properties (Liu & Ciftci, 2019).

Contrarily, Liu et al. (2018) observed that increasing WPI concentration helped to improve the printing performance of protein pastes. They stated that pure MPC paste was fragile, dry, and rigid upon extrusion from the nozzle, and it could not be shaped via extrusion-based printing. When they increased the MPC/WPI ratio to 6:1, the protein paste was easily extruded, but was still highly brittle and prone to collapse after printing. They further increased the WPI content and noted a smooth extrusion of protein paste with a more stable shape. However, excessively increasing WPI concentration can result in a protein paste with weaker mechanical strength, which can lead to collapse due to the inability to support its own weight. Consequently, protein paste with an MPC/WPI ratio of 5:2 was the best mixture since it provided excellent textural properties (Liu et al., 2018). Thus, it is imperative for the printed material to have optimum mechanical strength to support the weight of the deposited layers.

Zheng et al. (2019) and Chen et al. (2018) supported the use of starch-based food materials in 3D food printing technology. Chen et al. (2018) claimed that starches' shear-thinning and strain-responsiveness behavior made them suitable as 3D printed food materials. To ensure excellent starch printability, the desired starch-based printing materials should possess the optimal τy and G' values since these parameters are important in shape retention by being able to support their own weight. Other than having the appropriate τy and G' values, low τf values are also important to ensure smooth extrusion from the nozzle. Both τy and τf values are dependent on the concentration of the starch (Chen et al., 2018). Meanwhile, Zheng et al. (2019) concluded that wheat starch gel was the most suitable starch to be used as the 3D food printing material due to its lowest viscosity, better extrusion ability, and excellent storage properties. Thus, researchers can include wheat starch in future 3D food printing research within the concentration ranges that have appropriate G', τy and τf values to ensure successful printability of starch-based materials.

Derossi et al. (2020a) suggested the possibility of printing cereal-based snacks with different textures by controlling the numbers and sizes of pores. Even though the 3D printed snacks exhibited high shape fidelity without deformation even after the baking process, there was an 8% size reduction in the printed sample. Therefore, the snacks were smaller than the virtual model, which might be caused by dehydration during the baking process (Derossi et al., 2020a). The 3D printed samples studied by Derossi et al. (2020b) have a bigger pore size and a reduced number of pores caused by the screw-extrusion system and essential food compression in the 3D printing system. However, the main cause that creates most of the pores is the imbalanced printing conditions–printing speed and extrusion rate. The samples' microstructures vary greatly in 3D samples, affecting their mechanical properties and resulting in less favorable textures compared to the hand-made samples (Derossi et al., 2020b).

Furthermore, Vieira et al. (2020) studied different forms of A. platensis and their effects on the rheological properties of the 3D printed cookies. Their results have confirmed the suitability of all the formulations for extrusion. By using a diameter close to the opening of the nozzle, a homogenous filament was formed, and all the formulations presented consistent dimensional properties post-deposition. They also explained that using the antioxidant extract in the encapsulated form was much preferable to improve the stability of the 3D printed cookies in different environments.

Besides that, a mixture of pea-protein and alginate showed stable thermal properties, and no endothermic peak was detected at a lower temperature, indicating that the nutritional compositions in the mixture were well-preserved at the extrusion temperature, 45°C (Oyinloye & Yoon, 2020). Even though the mixture does not retain for a long time in the extrusion chamber, thermal stability is still important because it reflects the ability of the mixture to retain its nutrients from heat degradation at the printing temperature. Higher denaturation temperature of the mixture allows it to retain its nutritional components throughout the printing process (Oyinloye & Yoon, 2020).

Adding samples with hydrocolloids has shown an admirable textural property of the end-products (Dick et al., 2020). After heating, these samples displayed lower hardness, cohesiveness, and chewiness compared to the pork paste without any hydrocolloids. Cryo-SEM micrographs showed textural changes in samples with hydrocolloids due to the additional retention of water by the hydrocolloids, resulting in the formation of less dense matrix (Dick et al., 2020). Garcia-Segovia et al. (2020) implied that different compositions of gels could influence the textural properties. Reducing other components in the mixture also led to the reduction of Fmax, Fmean, area, and slope gradient due to the reduced synergistic interactions between xanthan gum and konjac gum (Garcia-Segovia et al., 2020). Thus, adding hydrocolloids helps to improve the texture of food materials, consequently improving their printability.

Lastly, results from Maniglia et al. (2019) and Maniglia et al. (2020) showed that longer DHT treatment had produced the best starch printability at the temperature of 130°C. Maniglia et al. (2019) explained that starch treated with DHT for a longer time had a larger granule size and higher carbonyl content. Water vaporization during the DHT treatment might contribute to the expansion of the granules and, hence, the larger granule size (Maniglia et al., 2020). Moreover, the higher carbonyl content presented in DHT-treated starches was caused by the oxidizing capability of DHT towards the starch molecules, and this was observed with increasing DHT period (Maniglia et al., 2019). The molecular structural changes indicate the effectiveness of DHT in modifying starches.

Furthermore, Maniglia et al. (2020) reported that the τy of DHT-treated starch increased with an increasing DHT period. It is an important characteristic of the food material to retain its shape under gravity and stresses from the deposited layers. Moreover, the tendency of undergoing amylose crystallization causes water to be released from the gels, also defined as syneresis, leading to an unfavorable condition for 3D printing (Maniglia et al., 2020). However, Maniglia et al. (2020) observed that the syneresis was reduced when the wheat starch was modified with DHT, which was a crucial element for a successful 3D printing process. Therefore, DHT treatment helps to improve the

printability of hydrogels based on different starches. In general, both works supported the use of the DHT process to improve the hydrogels' rheological properties, providing a suitable food ink for 3D printing.

5.   Recommendation

This review listed several recommendations that could be focused on for future studies. The primary recommendation for future studies is regarding the nutritional value of the food. Most studies have thoroughly focused on the food's physical properties. However, too little attention is paid to the nutritional content of food after it has been 3D printed. There were 15 journal articles found using strategic and systematic search, but only an article by Vieira et al. (2020) mentioned the beneficial properties. Besides that, the scholars may stress the portion of the printed food that is deemed suitable for the geriatric group according to the weight, size, concentration, calorie or nutritional value of the food. This latter will influence the variation of food design, the development of 3D printer technology, customization of healthy food, food industry dependency and the local economy.

6.   Conclusion

This study systematically reviewed 3D printing of personalized food for the elderly. It provides some insights and practical knowledge that are applicable in nurseries, homes, and healthcare settings. To conclude, the level of food hardness must be maintained in a suitable range that suits the needs of the elderly with mastication problems. Besides that, maintaining moisture content at certain ranges prevents bacterial growth, thus increasing the food storage period. 3D printing food also requires the use of materials with the right which may affect the extrusion process. Furthermore, each food has its own optimum ratio in combination with other materials to form products with the desired viscosity. Throughout the review, the elastic modulus has been measured for both pre-printed and printed samples, including samples tested for storage. G' and tan δ need to be maintained within a suitable range since it may affect the extrusion process. Also, personalized food for special populations can only be produced if the food ingredients used are printable. Therefore, it is vital for researchers to study the factors that influence the printability of materials to develop suitable food inks that can be printed into functional foods.

7.   Acknowledgement

Declaration Of Competing Interest

The team declares that there is no association within their knowledge relating to financial interests or personal relationships or any means that affect the work reported in the study.

8.   References

Braun, V., & Clarke, V. (2006). Using thematic analysis in psychology. Qualitative Research in Psychology, 3(2), 77–101.

Çakmak, H., & Gümüş, C. (2020). 3D Food Printing with Improved Functional Properties: A Review. International Journal Of 3D Printing Technologies and Digital Industry, 4(2), 178–192.

Chen, H., Xie, F., Chen, L., & Zheng, B. (2018). Effect of rheological properties of potato, rice and corn starches on their hot-extrusion 3D printing behaviors. Journal of Food Engineering, 244, 150–158.

Dankar, I., Pujolà, M., El Omar, F., Sepulcre, F., & Haddarah, A. (2018). Impact of Mechanical and Microstructural Properties of Potato Puree-Food Additive Complexes on Extrusion-Based 3D Printing. Food and Bioprocess Technology, 11(11), 2021–2031.

Derossi, A., Caporizzi, R., Oral, M., & Severini, C. (2020b). Analyzing the Effects of 3D Printing Process Per Se on The Microstructure and Mechanical Properties of Cereal Food Products. Innovative Food Science & Emerging Technologies, 66, 102531.

Derossi, A., Caporizzi, R., Paolillo, M., & Severini, C. (2020a). Programmable Texture Properties of Cereal-Based Snack Mediated by 3D Printing Technology. Journal of Food Engineering, 289, 110160.

Dick, A., Bhandari, B., Dong, X., & Prakash, S. (2020). Feasibility Study of Hydrocolloid Incorporated 3D Printed Pork as Dysphagia Food. Food Hydrocolloids. Food Hydrocolloids, 107, 105940.

Flemming, K., Booth, A., Garside, R., Tunçalp, O., & Noyes, J. (2018). Qualitative evidence synthesis for complex interventions and guideline development: clarification of the purpose, designs and relevant methods. BMJ Global Health, 4(1), e000882.

García-Segovia, P., García-Alcaraz, V., Balasch-Parisi, S., & Martínez-Monzó, J. (2020). 3D printing of gels based on

xanthan/konjac gums. Innovative Food Science & Emerging Technologies, 64, 102343.

Gou, M., Wu, H., Saleh, A. S., Jing, L., Liu, Y., Zhao, K., ... & Li, W. (2019). Effects of Repeated and Continuous Dry Heat Treatments on Properties of Sweet Potato Starch. International Journal of Biological Macromolecules, 129, 869–877.

Haddaway, N., Macura, B., Whaley, P., & Pullin, A. (2018). ROSES Reporting standards for Systematic Evidence Syntheses: pro forma, flow-diagram and descriptive summary of the plan and conduct of environmental systematic reviews and systematic maps. Environmental Evidence, 7(1). 1–8.

Hamilton, C. A., Alici, G., & in het Panhuis, M. (2018). 3D printing Vegemite and Marmite: Redefining "breadboards". Journal of Food Engineering, 220, 83–88.

Huang, M. S., Zhang, M., & Bhandari, B. (2019). Assessing the 3D Printing Precision and Texture Properties of Brown Rice Induced by Infill Levels and Printing Variables. Food and Bioprocess Technology, 12(7), 1185–1196.

Jonkers, N., van Dommelen, J. A. W., & Geers, M. G. (2020). Experimental characterization and modeling of the mechanical behavior of brittle 3D printed food. Journal of Food Engineering, 278, 109941.

Kim, H.W., Bae, H., Park, H.J., (2018). Reprint of: Classification of the printability of 310 selected food for 3D printing: Development of an assessment method using hydrocolloids as 311 reference material. Journal of Food Engineering, 220, 28–37.

Liberati, A., Altman, D. G., Tetzlaff, J., Mulrow, C., Gøtzsche, P. C., Ioannidis, J. P., ... & Moher, D. (2009). The PRISMA Statement for Reporting Systematic Reviews and Meta-Analyses of Studies That Evaluate Health Care Interventions: Explanation and Elaboration. Journal of Clinical Epidemiology, 62(10), e1–e34.

Liu, L., & Ciftci, O. N. (2020). Effects of High Oil Compositions and Printing Parameters on Food Paste Properties and Printability in A 3D Printing Food Processing Model. Journal of Food Engineering, 288, 110135.

Liu, Y., Liu, D., Wei, G., Ma, Y., Bhandari, B., & Zhou, P. (2018). 3D printed milk protein food simulant: Improving the printing performance of milk protein concentration by incorporating whey protein isolate. Innovative Food Science & Emerging Technologies, 49, 116–126.

Maniglia, B. C., Lima, D. C., Junior, M. D. M., Le-Bail, P., Le-Bail, A., & Augusto, P. E. (2019). Preparation of Cassava Starch Hydrogels for Application in 3D Printing Using Dry Heating Treatment (DHT): A Prospective Study on The Effects of DHT and Gelatinization Conditions. Food Research International, 128, 108803.

Maniglia, B. C., Lima, D. C., da Matta Júnior, M., Oge, A., Le-Bail, P., Augusto, P. E., & Le-Bail, A. (2020). Dry heating treatment: A potential tool to improve the wheat starch properties for 3D food printing application. Food Research International, 137, 109731.

Moher, D., Liberati, A., Tetzlaff, J., & Altman, D. (2009). Preferred Reporting Items for Systematic Reviews and Meta-Analyses: The PRISMA Statement. Plos Medicine, 6(7), e1000097.

Okoli, C. (2015). A Guide to Conducting a Standalone Systematic Literature Review. Communications of The Association for Information Systems, 37(1), 879–910.

Oyinloye, T., & Yoon, W. (2021). Stability of 3D printing using a mixture of pea protein and alginate: Precision and application of additive layer manufacturing simulation approach for stress distribution. Journal of Food Engineering, 288, 110127.

Page, M. J., & Moher, D. (2017). Evaluations of the Uptake and Impact of The Preferred Reporting Items for Systematic Reviews and Meta-Analyses (PRISMA) Statement and Extensions: A Scoping Review. Systematic Reviews, 6(1), 263.

Shaffril, H., Samsuddin, S., & Abu Samah, A. (2020b). The ABC of systematic literature review: the basic methodological guidance for beginners. Quality & Quantity, 1–28.

Shaffril, H., Ahmad, N., Samsuddin, S., Samah, A., & Hamdan, M. (2020a). Systematic literature review on adaptation towards climate change impacts among indigenous people in the Asia Pacific regions. Journal of Cleaner Production, 258, 120595.

Vieira, M. V., Oliveira, S. M., Amado, I. R., Fasolin, L. H., Vicente, A. A., Pastrana, L. M., & Fuciños, P. (2020). 3D printed functional cookies fortified with Arthrospira platensis: Evaluation of its antioxidant potential and physical-chemical characterization. Food Hydrocolloids, 107, 105893.

Zheng, L., Yu, Y., Tong, Z., Zou, Q., Han, S., & Jiang, H. (2019). The Characteristics of Starch Gels Molded by 3D Printing. Journal of Food Processing and Preservation, 43(7), e13993.